Dust measurements around the Moon and across the Solar System

by

E. A. Bernardoni

B.S., Mathematics and Physics, Case Western Reserve University, OH,

2014

A thesis submitted to the

Faculty of the Graduate School of the

University of Colorado in partial fulfillment

of the requirements for the degree of

Doctor of Philosophy

Department of Physics

2022

Committee Members:

Mihály Horányi, Chair

Xu Wang

Zoltan Sternovsky

Tobin Munsat

Sascha Kempf

Bernardoni, E. A. (Ph.D., Physics)

Dust measurements around the Moon and across the Solar System

Thesis directed by Prof. Mihály Horányi

Dust grains are a key source of impact bombardment which is a critical component of space weathering, a ubiquitous process occurring on all airless bodies in the solar system governing how the surfaces of airless bodies are physically and chemically altered over time. Additionally, these dust grains interact with a broad range of celestial bodies within our solar system resulting in changes to their size distribution and trajectories. Thus characterizing the dynamics and distribution of dust provides key insight into the evolution of our solar system and airless bodies in particular. When impacting solid surfaces, secondary dust ejecta can be produced. These ejecta, following ballistic trajectories, form an exosphere observable to in situ instruments such as the Lunar Dust Experiment (LDEX) aboard the Lunar Dust and Environment Explorer (*LADEE*) spacecraft. The primary dust grains can also be observed directly through in situ instruments such as the Venetia Burney Student Dust Counter (SDC) aboard the *New Horizons* spacecraft which to date has produced measurements up to 50 AU.

In this thesis, we will constrain the meteoroid environment at 1 AU using a forward modeling approach fitted to LDEX data. First, we expand a prior 2D plume simulation to 3D with additional considerations to derive impact ejecta cone angles relevant for the altitudes observed by LDEX. From these results, we construct a global lunar ejecta model fitted to LDEX observations to produce the product of impactor mass flux and mass yields for each of the primary sporadic background sources: helion, anti-helion, and apex. The potential for additional sources such as β-meteoroids is also explored. From this we consider the integrated current signal measurements from LDEX presumably produced from smaller ejecta dust grains. The potential for energetic neutral atoms (ENAs) produced from backscattered solar wind is discussed along with the apparent lack of small ejecta on the lunar night-side. Additionally, we implement a simply trajectory tracing model of the solar wind to determine if there exists significant electrostatic lofting enhancement from twilight craters. From this, we find no evidence for such an enhancement. Finally, updated meteoroid flux and densities are reported for several grain size cutoffs using recent SDC measurements under updated methodology.

Dedication

To my parents and siblings for their empathy, humor, and wit. Never has there been a more entertaining and trustworthy bunch and I am thankful and surprised every day at how fortunate I am to have you all in my life.

Acknowledgements

I could not have completed this thesis and made it to this point in my education without the guidance and support of many people who went above and beyond to push me to succeed and open paths otherwise inaccessible.

To Robert Brown who not only introduced me to my first internship opportunity, but who's support and advocating are the primary reason I am at CU today.

To Marcus Piquette who tutored me in the ways of SDC and the arcane practices that make up its pipeline.

To Jamey Szalay for answering my novice questions and who's enthusiasm sold me on LDEX research.

And, most importantly, to my advisor, Mihály Horányi, who's patience and guidance I really don't deserve. I am extremely fortunate to have spent my graduate career under his advisement as I simply would not be where I am today without his help. Thank you again for all your support and I hope to someday pay that kindness forward.

Contents

List of Tables

Table

List of Figures

Figure

Chapter 1

Introduction

1.1 Meteoroid Environment

Dust from a variety of sources permeates our entire solar system. Their trajectories are influenced by gravity due to the Sun and the planets, trapping in mean-motion resonances [69, 73, 74, 90], radiation pressure, Poynting-Robertson drag, and electromagnetic forces, and their size distribution is altered by sublimation, sputtering, and mutual collisions [120, 90]. As dust grains interact with a broad range of celestial bodies, understanding the dynamics and distribution of dust provides key insight into the evolution of our solar system.

Dust grains sourced by comets, asteroids, or Edgeworth-Kuiper Belt Objects within our solar system are known as interplanetary dust particles (IDP) while those originating from outside our solar system are known as interstellar dust particles (ISD). Comets in particular are the primary source of IDPs in the inner solar system. Comets are bodies formed in the outer solar system and ejected from their place of origin through the formation of planets [68]. These fall into two general source groups of Oort Cloud Comets and the Scattered Disk shown in Figure 1.1 characterized by high eccentricities and a broad range of inclinations for the former and low eccentricities and inclinations for the latter [79, 28, 68]. The Scattered Disk sources Jupiter Family Comets (JFC) produce the majority of IDPs in the inner solar system [77]. IDP production in the outer solar system, in contrast, is dominated by Edgeworth-Kuiper Belt Object (EKBO) via mutual collisions and bombardment by ISDs and IDPs [101, 127]. Grains produced in this manner tend to flow toward the Sun as they become slowed by Poynting-Robertson drag; after which Neptune tends to prolong the lifetime of these IDPs while Jupiter blocks inward flowing IDPs by ejecting most that cross its orbit. Asteroids, also sourced from the formation of planets, produce IDPs via mutual collision and bombardment located primarily between Mars and Jupiter [105].

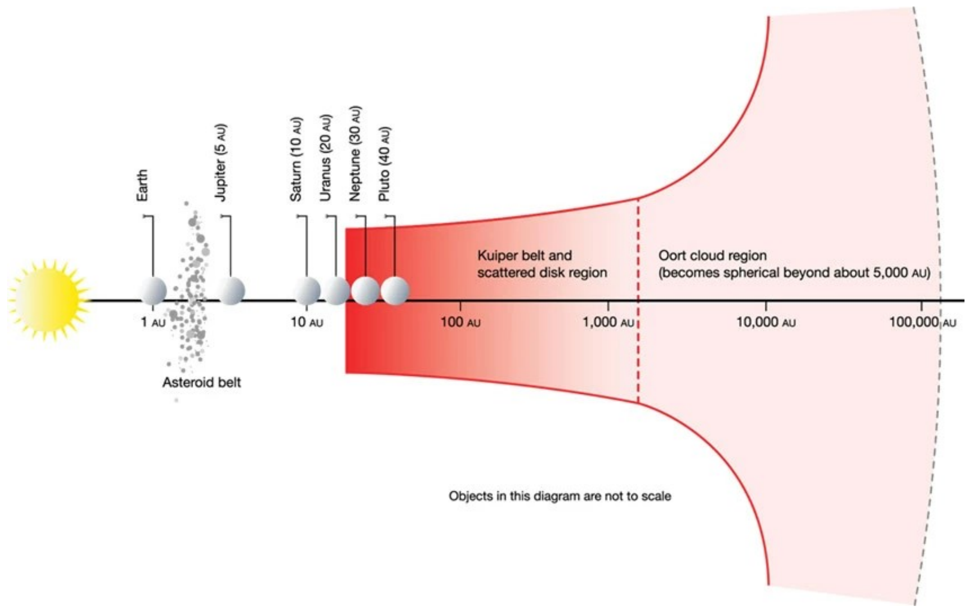

Figure 1.1: Illustration of the relative positions of the Oort Cloud, Kuiper belt, and Scattered Disk taken from [100].

IDPs that interact with the Earth-Moon system are classified either as meteoroid showers or sporadic background. When initially produced, IDPs follow similar trajectories to their parent body before becoming modified and consequently decoupled by radiation pressure, Poynting-Robertson drag, grain-grain collisions, and electromagnetic forces. As each of these forces are size dependent, smaller grains (radii $< 100\ \mu$m) become entirely decoupled from their source while larger grains (radii $> 100\ \mu$m) gradually disperse along a similar orbit to their parent body [45, 46]. The former makes up the sporadic background while the latter produces meteoroid showers. Meteoroid showers are characterized by highly collimated beams of particles originating from a localized region in the sky while the sporadic background is comprised of dust particles with trajectories decoupled from their parent bodies though can still be characterized by "source" classified by concentrations at a fixed radiant with respect to the apex of the Earth's motion [45]. The sporadic background is the largest contributor to the total meteoroid flux at 1 AU.

Sporadic background meteoroids are generally grouped with respect to their source radiant relative to the apex of the Earth's motion, shown in Figure 1.2, as helion (HE), antihelion (AH), apex (AP), antiapex (AA), northern toroidal (NT), and southern toroidal (ST). The two toroidal sources are characterized by steep inclination toward the Earth's equator while the first four sources are near equatorial sources. HE and AH meteoroids follow prograde low inclination orbits where the AH portion encounters 1 AU before their closest approach to the Sun while the HE portion is the same population on its way back after closest approach. In contrast, AP and AA meteoroids orbit in retrograde motion and encounter 1 AU on the outbound portion and inbound portion of their trajectories respectively. HE, AH, NT, and ST meteoroids are thought to be produced from JFCs while AP and AA meteoroids are thought to be produced from Halley-type and long-period comets from the Oort Cloud. The general radiants of each source are skewed toward the Earth's orbital ram direction when observed at the Earth and Moon due to the Earth's orbital velocity [114, 117, 20, 70].

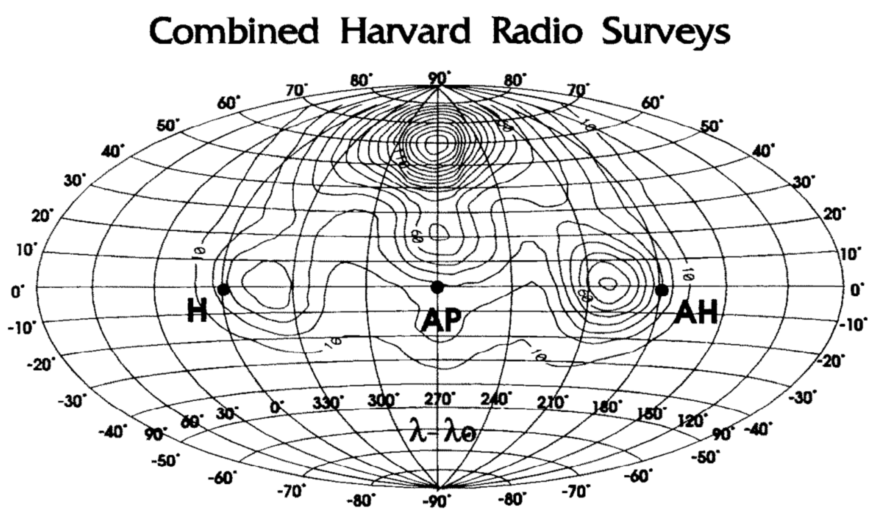

Figure 1.2: Activity contours for the combined Harvard I and Harvard II radio surveys depicting helion, antihelion, and apex sporadic background sources taken from [56, 55].

1.2 Scientific Motivation

Recent efforts analyzing the cosmic dust accretion rate to the Earth's surface and the injection rate of Na and Fe atoms to the Earth's atmosphere have led to an estimate of 43 $\pm$ 13 t d^{-1} for the total meteoroid mass input to the Earth [22]. However, estimates using a variety of observation methods from Earth-based radar to satellite-based dust detectors differ by as much as two orders of magnitude [85]. This uncertainty is due in part to the limited mass range of each of these techniques. None can observe particles over the entire mass range of 10^{-12} g to 1 g which covers the majority of meteoroids at 1 AU [85]. In situ instruments in particular suffer from a low detection rates due to smaller collection areas compared to ground based methods such as radar [40]. These methods, however, must contend with the additional complexity of the Earth's atmosphere. Another means of constraining the total meteoroid flux at 1 AU is by measuring the production rate of the ejecta produced via continuous meteoroid bombardment of the lunar surface effectively treating the Moon as one large detector. Constraining the total meteoroid flux at 1 AU through this additional detection method is key to further understanding of the evolution and dynamics of our solar system.

Additionally, dust grains are a key source of impact bombardment which is a critical component of space weathering, an ubiquitous process occurring on all airless bodies in the solar system governing how the surfaces of airless bodies are physically and chemically altered over time [81]. Characterizing space weathering processes is essential for understanding the origin and evolution of airless bodies in our solar system [18, 26]. High-speed impactors modify the surfaces of airless bodies by uncovering and redistributing surface material in a process called impact gardening [7, 24]. For bodies with diverse surface materials and mineralogy, impact bombardment can serve to redistribute mineralogically distinct material to other regions of the surface, with an efficacy that depends on the impactor distribution and specific properties of the impact plumes they create [110]. Additionally, surface based instruments that rely on utilizing optical surfaces exposed to space, such as lunar laser reflectors [75, 76], may accumulate layers of surface regolith over time, affecting their operation and efficiency. Thus, constraining the properties of both the primary impactors as well as the characteristics of the impact plumes they generate is key to understanding the continual evolution of airless surfaces as well as the solar system as a whole.

1.3 Lunar Dust Experiment

Observations of the lunar ejecta environment by the Lunar Dust Experiment (LDEX) onboard the Lunar Atmosphere and Dust Environment Explorer (*LADEE*) mission discovered a permanently present dust cloud produced by continual meteoroid bombardment [50]. Measuring from October 16, 2013 to April 18, 2014, LDEX observed a total of ~ 140000 dust impacts. This dust cloud is highly sensitive to meteoroid showers and changes in impactor flux rates [118, 117]. Of the sporadic meteoroid sources, impact ejecta were correlated with the HE, AH, and AP sources as primary contributors with a small contribution from the AA source and possible contributions from NT and ST sources, each oscillating with lunar phase [114, 117, 112]. The fluxes of these four sporadic sources can be constrained by LDEX observations through a forward modeling approach.

For grains with radii > 0.3 μm, LDEX records individual dust via impact ionization plasma charge produced from dust grain impact with a grounded hemispherical target to establish an impact rate and size distribution under certain assumptions. These larger grains are produced as ejecta from continual meteoroid bombardment of the lunar surface and follow ballistic trajectories [50]. It is from this data set that we will be constraining the IDP flux at 1 AU per sporadic background sources. For the purpose of characterization of smaller lunar ejecta, LDEX also records an integrated current measurement. These smaller ejecta are of particular interest as mechanisms other than meteoroid bombardment, such as electrostatic lofting, may be the dominant driver for their dynamics, particularly over the lunar terminators [25, 39, 12]. This data set provides the first dedicated dust instrument detections of the lunar environment up to altitudes as high as 250 km [49].

1.4 IDP Distribution in the Outer Solar System

Several in-situ dust detectors on various spacecraft have covered a broad range of the solar system. *HEOS 2* and *HELIOS* observed the IDP environment near 1 AU [27] while both *Galileo* and *Ulysses* measured from Earth to Jupiter, including measurements above/below the ecliptic plane [62]. *Cassini* observed IDP between Jupiter and Saturn [1] while *Pioneer 10* and *11* covered up to 9 and 18 AU, respectively [52]. In addition to dedicated in-situ dust detectors, *Voyager* measurements of dust particles approximately a micron in size were reported up to 100 AU through the detection by radio and plasma wave instruments of the plasma clouds produced via impact with the spacecraft [43].

The Venetia Burney Student Dust Counter (SDC) is an in-situ dust detector aboard the *New Horizons* spacecraft with IDP measurements spanning past 50 AU to date for grains with mass $m > 10^{-12}$ g. Collisions between EKB objects are suggested by numerical models to be a dominant source of IDP [90, 89]. As such, measurements up to and beyond this range are key for resolving the validity of this prediction which directly relates to the large-scale structure of our solar system and debris disks around other stars [125]. It is from this data set that we will estimate the total IDP flux in the outer solar system with considerations taken for potential ISD contributions.

1.5 Thesis Outline

With the goal of constraining the meteoroid flux at 1 AU and beyond as well as the characterizing the lunar dust environment, we focus on connecting the LDEX data set to these quantities as well as report on recent SDC values under updated methodology. To accomplish this, we follow three primary modelling thrusts which constitute the four main sections of this thesis:

Ejecta Plume Characterization Using individual LDEX plume detections produced from meteoroid streams, we fit inner and outer cone ejecta angles using a self-consistent 3D Monte Carlo simulation. This section expands upon prior 2D plume simulation fits which produced surprisingly narrow outer cone angles of $< 10°$ compared to the anticipated $30°$ [17].

Global Lunar Ejecta Model Using the constrained ejecta distributions from the previous section, we construct a global ejecta model to connect LDEX impact rates to meteoroid impactor flux and mass yields per source. Assuming equal rates and yield for HE and AH sources, we then consider the potential for additional sources, namely β-meteoroids [14].

Integrated Current As the global ejecta model indicated a potentially significant contribution from smaller impactors (and consequently smaller ejecta), We explore the integrated current signal of LDEX designed for detecting dust grains with radii < 0.3 μm. As the integrated signal is sensitive to more than just dust impacts, we start by characterizing the dominant enhancements on the lunar day and night-sides. For the day-side, we explore the potential for energetic neutral atoms (ENAs) produced from solar wind ions backscattered and neutralized from the lunar surface. Following this, a simple model for electrostatic lofting enhancement by twilight craters is constructed and compared to integrated current values near 6 local time [15].

IDPs Beyond 1 AU Using SDC measurements recently covering up to 50 AU, we produce IDP flux and density values for several grain size cutoffs. Updated methodology is used to correct the implementation of reference channels used in prior studies. Values follow current prediction models though the potential contribution from ISDs to cause a deviation in future measurements is also considered [16].

Chapter 2

Ejecta Plume Characterization

2.1 Introduction

To connect ejecta detection rates from LDEX to meteoroid fluxes, the structure and dynamics of lunar ejecta plumes must first be characterized. To this end, numerous laboratory experiments have been performed [23, 6, 10, 51]. These experiments focused on the cratering effects on glass and sand targets produced by impactors with sizes on the order of 5 mm and impact speeds ranging from 0.085-1.9 km s^{-1} [23, 6, 10, 51]. Additionally, spacecraft missions such as Deep Impact [95, 94] and the Lunar Crater Observation and Sensing Satellite (LCROSS) [47] along with complimentary laboratory and theoretical work provide direct observations of impact ejecta dynamics on airless bodies, though on a much larger scale than the plumes discussed in this paper. Impact experiments into ice-silicate mixtures [58] were used successfully to describe the impact ejecta measurements near Jupiter's large icy moons [61, 60, e.g.]. However, the ejecta response of a fluffy regolith surface may be characteristically different than that of a hard, icy surface. While these experiments and others provide key insight into a broad range of ejecta parameters, interplanetary dust impactors into regolith surfaces are difficult to reproduce in the lab and may have different characteristics than much larger, slower impactors. Thus, constraining existing models to the lunar dust environment can bolster our understanding of interplanetary dust impactors into regolith surfaces and is also a necessary first step in providing a meteoroid flux estimate via lunar ejecta measurements.

Each impact LDEX detected came from an individual particle within an impact ejecta plume. Typically, separate impacts were assumed to originate from separate plumes. However, throughout

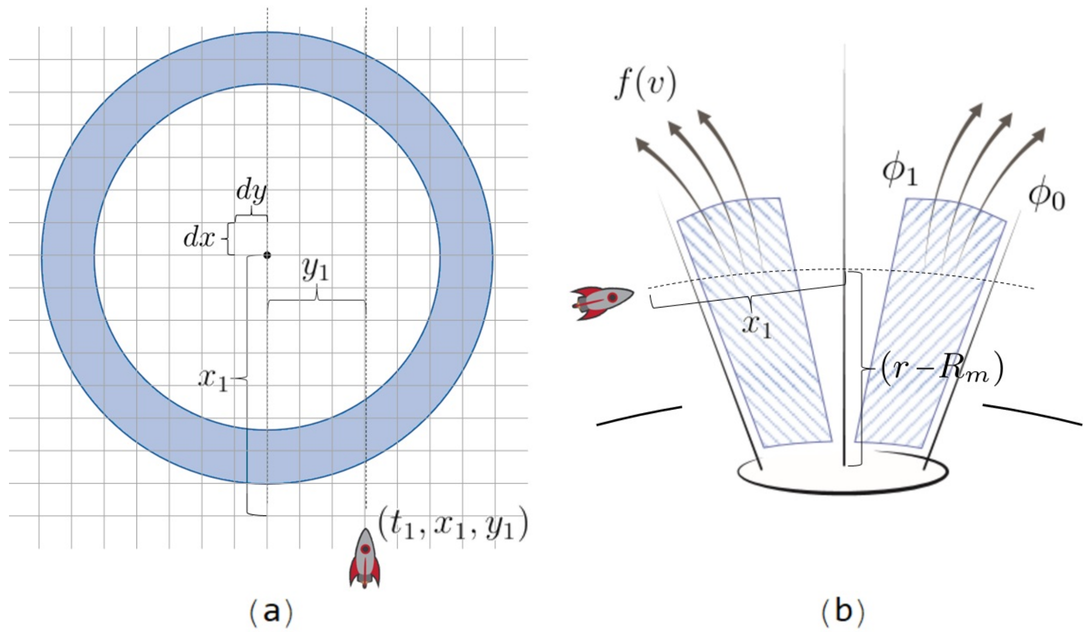

Figure 2.1: Illustration of the simulated plume and flight path. The blue ring represents the generated plume while the dotted line represents the a simulated flight path. **(a)** shows the top view of the plume model labeled with the starting point of the simulated flight path (t_1, x_1, y_1) as well as grid steps dx and dy used for binning the simulated impact rates. **(b)** shows the side view of the plume model labeled with inner and outer cone angles ϕ_1 and ϕ_0 respectively. Note that the grid shown in **(a)** is actually curved at a fixed altitude of $(r - R_m)$. dx and dy are fixed to 1.67 km for all altitudes considered to allow for direct comparison between plume fits.

the mission, LDEX observed 'bursts' of particles, which were interpreted to all originate from the same impact ejecta plume. It is these 'bursts' we focus on in this chapter. As these observations were the first in-situ dust measurements of dense lunar ejecta plumes, analysis of the results provides unique insight into the physics of in-situ hypervelocity dust impacts. Previous work implemented a two-dimensional model matched to LDEX data to derive the initial ejecta speed, mass, and angular distributions [107]. This approach derived ejecta cone angles that were much narrower than those used in previous literature with an interior region void of ejecta as shown in Figure 2.1 [50, 60]. The two-dimensional model, however, assumes that the detector flew through the center of the plume. Additionally, the speed distribution used was later improved to account for the correlation between local time and altitude of the sampling [117]. More specifically, the speed distribution is derived from energy conservation and an exponential fit to the average dust density profile as a function of altitude. Figure 2.2 shows the calculated density as a function of latitude in LT bins excluding meteoroid shower activity and normalized to the 6 LT [117]. The dashed line indicates the best exponential fit to the average in the form of $n(h) = n_0 e^{-h/\lambda}$ corresponding to a altitude distribution of $f(h) = \frac{1}{\lambda} e^{-h/\lambda}$ where h is the altitude in kilometers, n_0 is the density at the lunar surface, and $\lambda = 200$ km is the scale height from the fit. From energy conservation, we have the relation $h(v) = \frac{R_m}{(v_e/v)^2 - 1}$ where $v_e = 2.4$ km s^{-1} is the lunar escape speed and $R_m = 1737$ km is the Moon's radius. Therefore, the one-dimensional initial ejecta velocity distribution is derived as [117],

$$f(v) = f(h(v)) \frac{dh}{dv} = \frac{2 R_m v}{\lambda v_e^2 (1 - (v/v_e)^2)^2} e^{-\frac{R_m/\lambda}{(v_e/v)^2 - 1}}. \tag{2.1}$$

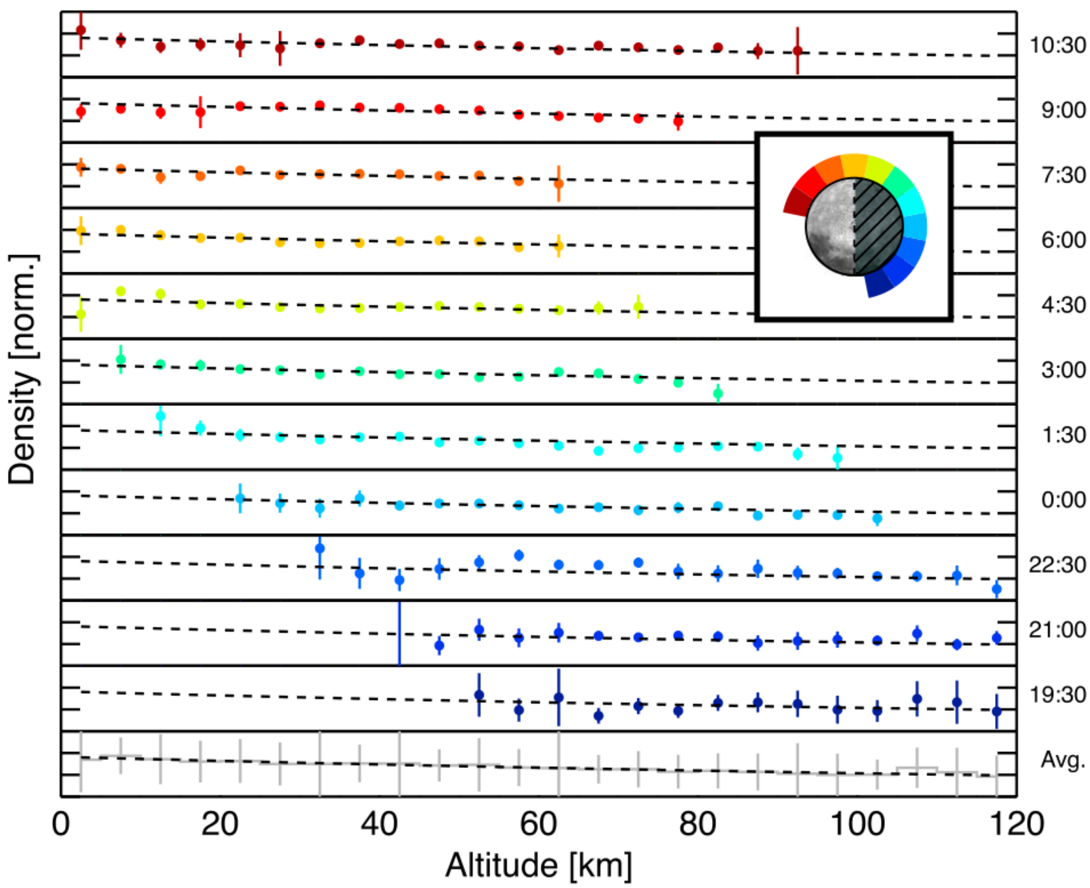

Figure 2.2: Dust density as a function of altitude per local time bin indicated by color normalized to the 6 LT values. The dashed line shows the exponential with a scale height of $\lambda = 200$ km derived as the best fit to the average over all local times indicated in the last panel [117].

A lack of altitude dependence in the detected impact charge distribution of, as shown in Figure 2.3, suggests that the initial ejecta mass and speed distributions can be decoupled [50]. However, we note that to some extent these distributions will be correlated [92]. Additionally, the measured impact charge closely follows a power law of the form $p_q(q) \propto q^{(1(1+\alpha))}$ with power of $\alpha = 0.910 \pm 0.003$ indicated by the inset of Figure 2.3. Therefore the rate of ejecta produced from the lunar surface with masses greater than m has the form of the power law $N^+(m) \propto m^{-\alpha}$ and an ejecta mass distribution of of the form $f(m) \propto m^{-(1+\alpha)}$ [50].

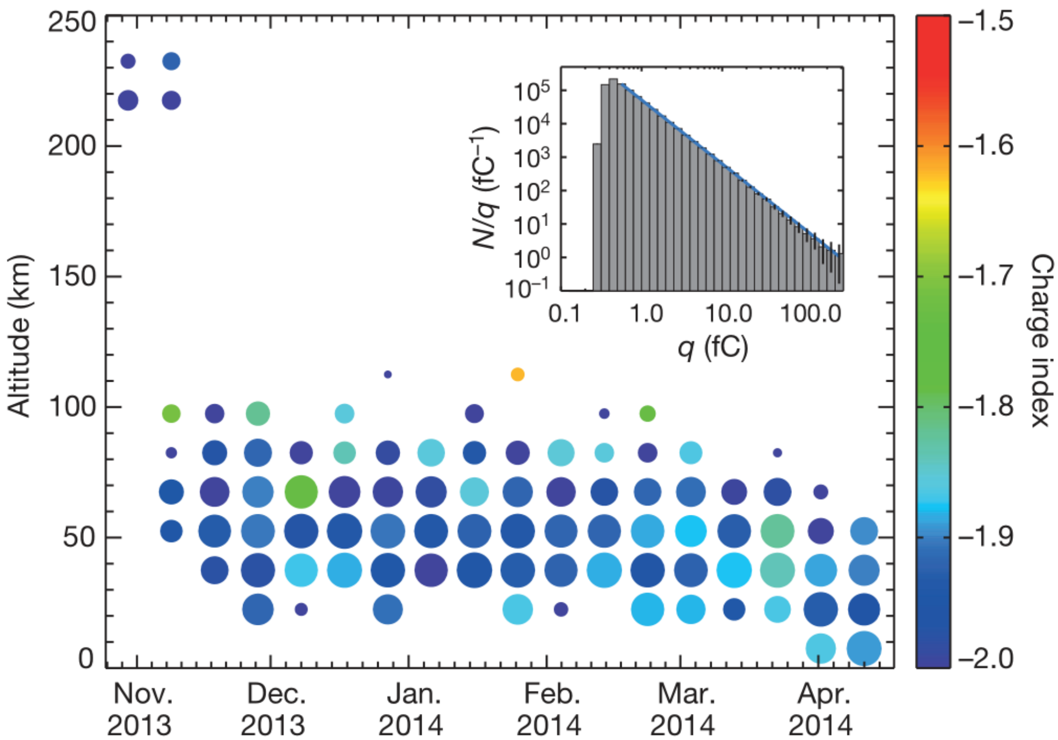

Figure 2.3: Exponent of the form $p_q(q) \propto q^{(1(1+\alpha))}$ fitted to LDEX charge measurements binned by altitude and time in 15 km and 10 day bins respectively. Color indicates the values of $-(1+\alpha)$ while size is inversely proportional to uncertainty from ± 0.1 to ± 0.5. The inset plots the impact charge distribution for the entire mission with a fitted power of $\alpha = 0.91 \pm 0.003$ [50].

For simplicity, and driven by the previously mentioned absence of altitude and impact charge correlation, we assume the initial ejecta distribution is represented as the product of speed, mass, and angular distributions,

$$\begin{aligned} f(v) &= \frac{2R_m v}{\lambda v_e^2(1-(v/v_e)^2)^2} e^{-\frac{R_m/\lambda}{(v_e/v)^2-1}}, \\ f(m) &= \frac{\alpha}{m_{min}^{-\alpha} - m_{max}^{-\alpha}} m^{-(1+\alpha)}, \\ f(\phi) &= \frac{\sin\phi}{\cos\phi_1 - \cos\phi_0}, \end{aligned} \tag{2.2}$$

where $v_e = 2.4$ km s^{-1} is the lunar escape speed, $R_m = 1737$ km is the Moon's radius, and $\lambda = 200$ km is the characteristic scale height derived from the dust density distribution measurements [117]. The mass exponent ($\alpha = 0.91 \pm 0.003$) was measured by LDEX consistent across all local times [50], and the mass bounds ($m_{min} = 10^{-17}$ kg and $m_{max} = 10^{-8}$ kg) were determined by the detection limits of LDEX at the spacecraft's apex velocity. While $f(v)$ and $f(m)$ are empirically derived from from averaged LDEX measurements assuming purely vertical motion, $f(\phi)$ is assumed to be a uniform distribution of the form presented in [50] with an inner cone angle. Note that as a consequence of the vertical motion assumptions in the derivation of $f(v)$, a large ϕ_0 would indicate an inconsistency in the model. An assumed initial ejecta speed distribution, however, is a necessary component of expanding this fit to including an offset from the center of the plume as without the general impact rate profile of a simulated fly through, the fitted solution becomes degenerate with arbitrarily large outer cone angles with increasing offset. By implementing the distributions in Eq. 2.2 into a Monte Carlo 3D simulation with ϕ_0 and ϕ_1 as fit parameters ranging from 0° to 45°, we will constrain these values relevant to the lunar ejecta environment for use in the global ejecta model in Chapter 3.

2.2 Plume Identification

LDEX received impacts above its detection threshold of $a > 0.3$ μm at an average rate of $\mu = 2.3 \times 10^{-2}$ s^{-1} during commissioning and $\mu = 3.1 \times 10^{-2}$ s^{-1} during the nominal science mission (21-Nov-2013/18-Apr-2014) [50]. We must determine if a given set of impacts is statistically anomalous with respect to the average background impact rate LDEX observed. To do this, we note that the impact rate can be described as a Poisson process. The probability of detecting n

impacts within a time Δt is,

$$P(n, \Delta t) = 1 - e^{-\mu\Delta t} \sum_{n'=0}^{n-2} (\mu\Delta t)^{n'}/n'! \tag{2.3}$$

where n is the number of impacts, Δt is the total elapsed time, and μ is the average impact rate [116, 78]. The $n-2$ in the upper limit of the summation follows from the assumption that Δt begins and ends at individual particle detections. For example, the probability of detecting 2 particles separated by time Δt is $P(2, \Delta t) = 1 - e^{-\mu\Delta t}$. Using Eq. 2.3, we can quantify the probability of a set of impacts occurring by employ a sliding window throughout the data of either a fixed time range Δt or a fixed number particles n. Since the temporal structure of the impact rate time series is highly variable, we elected to fix the number of particles. Measurements referred to as 'bursts' are impact rates with probability of detection $P < 10^{-3}$ containing at least $n = 5$ particles as shown in Figure 2.4 (b).

In this analysis, we are concerned with the total number of impacts in a given plume. Therefore, consecutive bursts are grouped together in the following manner. We search for bursts within a sliding window of 30 seconds and group these together as a 'plume' measurement as shown in Figure 2.4 (c). The total number of particles contained in each plume measurement are estimated as $N_{plume} = nN_b$, where N_b is the number of consecutive bursts. Since we group consecutive bursts together, plume identification is not very sensitive to n for sufficiently small values. Additionally, as long as P is small enough to exclude unrelated groupings but not too small to exclude most events, the results are not highly sensitive to P.

For the following analysis, we only consider the very largest plume detections which contain 75 or more individual impacts. Figure 2.4 (a) shows all identified plumes with the threshold of 75 particles indicated by a dotted line. Table 2.1 lists each plume's detection time, duration, number of impacts, altitude, and spacecraft speed. Note that for this analysis we treat all plumes equally regardless of temporal coincidence with meteoroid showers. These 18 plumes, detected at altitudes spanning from 24 km to 89 km, represent the most statistically significant detections of lunar impact ejecta plumes by LDEX. An impact rate time series for three such detections are shown in

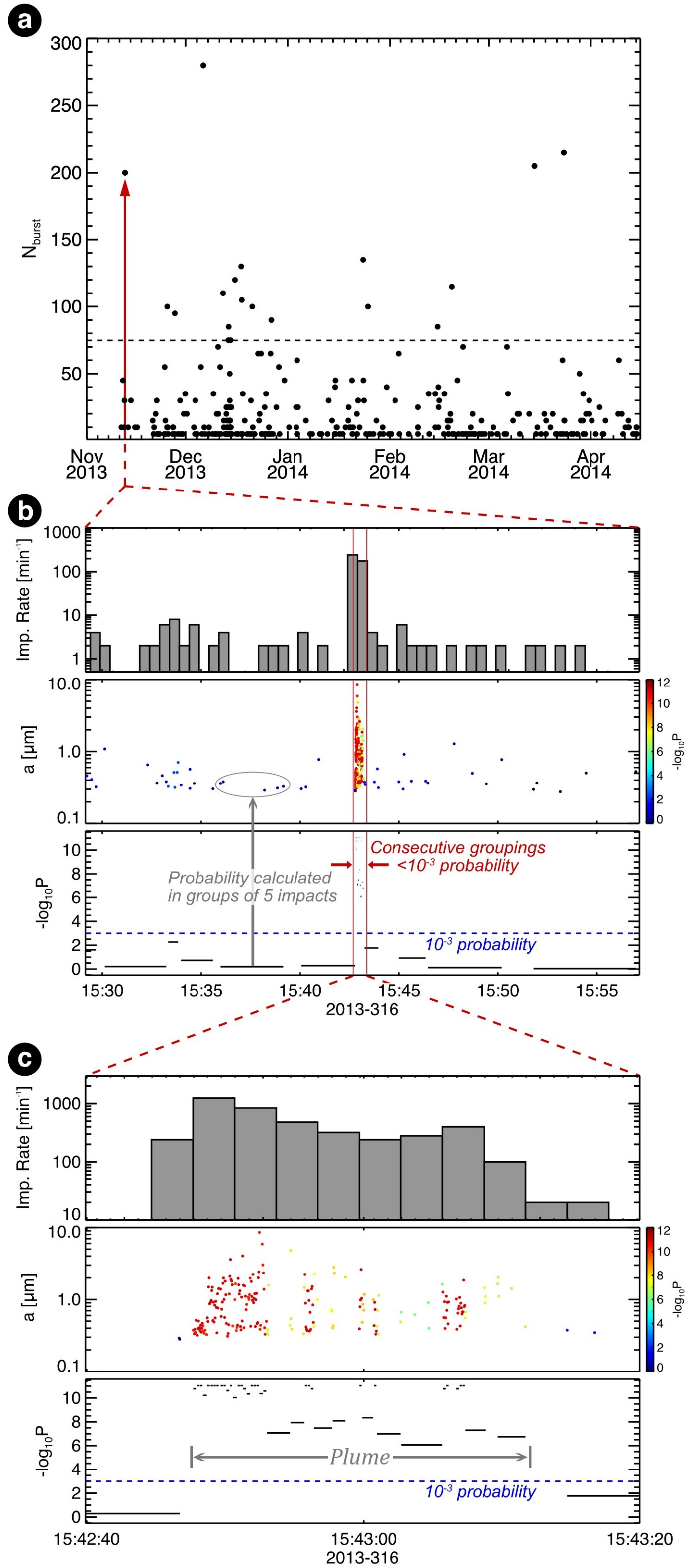

Figure 2.4: **(a)** all plumes detected with consecutive bursts identified by Eq. 2.3. The selection threshold of 75 particles is indicated by a horizontal dotted line. **(b)** time series showing impact rate (top), size (middle) and probability for each 5 impact grouping (bottom) for the burst indicated with the red arrow in (a) on 12-Nov-2013. **(c)** zoomed in version of (b) showing the detailed structure of the plume detection [17].

Figure 2.5 (b). These impact rates were calculated using a sliding window of 3 seconds and have been normalized by their peak values. The structure in any given plume detection is dependent on the time and location of LDEX relative to the lunar impact site. There is no a priori method to extract this temporal and geometric information from the LDEX data, therefore, a model must be used to interpret these impact rates in a meaningful way.

2.3 Method

To produce new fits for ϕ_0 and ϕ_1, a Monte Carlo approach was implemented to simulate impact rates on LDEX from a single plume with the restriction that $\phi_0 - \phi_1 \geq 0.5°$. Roughly a billion simulated ejecta particles were produced through initial sampling of the speed and angular distributions in Eq. 2.2 from which the Kepler equations of motion are calculated for each as described in Section 2.3.1. Section 2.3.2 describes the impact rates calculations for which the velocity dependence of the minimum detectable mass by LDEX plays a key role. A χ^2 minimization was then performed using LDEX data with bursts containing more than 75 particles as discussed in Section 2.3.3.

Aside from ϕ_0 and ϕ_1, the other tunable parameters of this minimization were the time of the first detected impact, t_1, and starting position of the spacecraft relative to plume origin, (x_1, y_1), as shown in Figure 2.1. The inclusion of a second spatial parameter, correction to the ejecta speed distribution in Eq. 2.2, and the removal of the apex velocity assumption in the implementation of the impact rate (described in Section 2.3.2) are the three notable changes from previous two-dimensional fit [107].

2.3.1 Plume Generation

First, a set of initial particle speeds and angles were generated via random sampling of the distributions in Eq. 2.2. Since ejecta-ejecta interactions are assumed to be negligible and initial ejecta speeds are restricted to be less than v_e, trajectories can be modeled as elliptical orbits. The assumption of bound ejecta particles is based on the previous estimates for the speed distribution.

Table 2.1: LDEX plume detections with more than 75 impacts.Columns correspond to Time (UTC), duration (s), number of impacts N_{plume}, Altitude (km) and LADEE ram speed v_{ram} km s^{-1}.

Time (UTC)	Duration (s)	N_{plume}	Altitude (km)	v_{ram} (km s^{-1})
12-Nov-2013 15:42	22	200	91.6	1.67
06-Dec-2013 09:39	24	280	71.2	1.65
18-Dec-2013 01:39	18	105	70.8	1.64
15-Feb-2014 12:03	14	85	67.2	1.65
14-Dec-2013 16:19	12	75	64.5	1.64
12-Dec-2013 09:33	20	110	61.4	1.64
14-Dec-2013 02:51	20	85	55.1	1.65
21-Dec-2013 05:50	14	100	54.1	1.66
16-Dec-2013 00:06	14	120	51.9	1.66
19-Feb-2014 19:19	32	115	51.7	1.67
27-Nov-2013 17:17	5	95	50.8	1.67
14-Dec-2013 00:44	16	75	48.9	1.66
16-Mar-2014 21:40	27	205	44.1	1.67
25-Mar-2014 18:46	14	215	44.1	1.67
25-Jan-2014 07:28	15	100	39.2	1.68
23-Jan-2014 20:23	12	135	33.2	1.68
17-Dec-2013 21:21	13	130	32.9	1.68
27-Dec-2013 00:35	15	90	27.2	1.69
25-Nov-2013 10:58	13	100	23.0	1.69

While there may be a small fraction of unbound ejecta at the Moon, LDEX was unable to quantify this minor constituent. For mathematical simplicity, we proceed under the assumption of bound ejecta. For a given initial ejecta speed, v_i, and angle from surface normal, ϕ_i, the parameters defining an elliptical orbit (eccentricity: e, semimajor axis: a, frequency of revolution: ω^*, total energy: E, and angular momentum: l) are calculated as follows:

$$\begin{gathered}\frac{k}{m} = GM_m, \quad \tfrac{E}{m} = \tfrac{1}{2}v_i^2 - \tfrac{k}{mR_m}, \quad \frac{l}{m} = R_m v_i \sin\phi_i, \\ a = -\frac{k}{2E}, \quad e = \sqrt{1 - \tfrac{l^2}{mka}}, \quad \omega^* = \sqrt{\frac{k}{ma^3}},\end{gathered} \tag{2.4}$$

where $M_m = 7.3476 \times 10^{22}$ kg is the mass of the moon, m is the mass of the ejecta in kg, $G = 6.67408 \times 10^{-11}$ m^3 kg^{-1} s^{-2} is the gravitational constant, and k is the gravitational force coefficient calculated as the product of the two masses and G. Using these parameters, the equations of motion in polar coordinates (radius: r, angle: θ, time: t) can be written using the eccentric anomaly, ψ:

$$\begin{gathered}t = \frac{1}{\omega^*}\left(\psi - e\sin\psi\right), \qquad r = a\left(1 - e\cos\psi\right), \qquad \cos\theta = \frac{a\left(1-e^2\right)}{er} - \frac{1}{e}, \\ v_\theta = v_i \sin\phi_i \frac{R_m}{r}, \quad v_r = v_i\cos\phi_i \tfrac{\sin\theta}{\sin\theta(r=R_m)}.\end{gathered} \tag{2.5}$$

Note that Eq. 2.5 are independent of m. Taking advantage of this for a later consideration, we initially only sample the speed and angular distributions in Eq. 2.2.

Using Eq. 2.5, ejecta trajectories were sampled over a fixed time step of $dt = 1$ s and duplicated at fixed azimuthal angle steps about surface normal $d\Phi = \frac{\pi}{272}$. Positions were then compared to a spatial grid binned by altitude steps of $dr = 1$ km and horizontal steps $dy = dx \equiv r d\theta = v_{sc} dt = 1.67$ km as illustrated in Figure 2.1 (a). $v_{sc} = 1.67$ km s^{-1} is the spacecraft's speed with $\hat{x}$ chosen to correspond to the spacecraft's velocity. We note that the spacecraft ram speed varies about 1.67 km s^{-1} by up to 2%, from 1.64 to 1.69 km s^{-1} for the 18 plume detections as shown in Table 2.1. We employ a fixed value of 1.67 km s^{-1} to reduce model complexity by keeping the grid size identical throughout all runs. Contributions are recorded in each relevant spatial-temporal bin as an impact rate as described in the next section.

It is important to note that dx and dy are fixed to 1.67 km for all altitudes and correspond to arc-lengths at each altitude bin. This allows for a more direct comparison between fits at varying altitudes without having to account for changing bin sizes associated with fixed angular bins in a spherical coordinate system. Additionally, when implementing the duplication of trajectories, we are assuming azimuthal symmetry of the plume. This is equivalent to assuming that the obliqueness of an impact, along with impactor speed and mass, only affects the ejecta yield of the subsequent plume (an assumption we also use for the global ejecta model in Chapter 3). As we will be comparing normalized impact rates between measured and simulated results, contributions associated only with ejecta yield have no effect on the fitted results. We assume azimuthal plume symmetry primarily to avoid introducing additional tunable parameters as well as the degeneracy associated with allowing the simulation to fit to only half of the plume. However, there exists compelling laboratory evidence for significant asymmetry in ejecta flow resulting from oblique impacts [6]. Extrapolating these results to relevant impactor parameters and introducing assumptions on the impact angle would allow for the implementation of asymmetry in the plume model. As this approach would require additional assumptions on the mass and speed of the impactors, we will proceed under the simplified model of azimuthal symmetry with the justification at plume asymmetry decreases with time and thus altitude [6].

2.3.2 Impact Rate

LDEX measures impact rates, not densities. Therefore, to compare modeled plumes to LDEX measurements, local impact rates must be calculated. In the previous two-dimensional fit [107, 116], ejecta were assumed to be at their orbital apex when calculating impact rate. With the addition of a third dimension, this assumption was dropped as the impact angle must now be calculated regardless. Consequently, the velocity dependence of the lower mass threshold m_{min} also needs to be evaluated as [107, 116],

$$m_{min} = C_m v_{rel}^{-4.76}, \quad \vec{v}_{rel} = (v_\theta \cos\Phi - v_{sc})\hat{x} + v_\theta \sin\Phi \hat{y} + v_r \hat{r}, \tag{2.6}$$

where $\vec{v}_{rel}$ is the ejecta's velocity relative to the spacecraft at the point of detection and $C_m = 0.91$ is a constant. Using Eq. 2.6 and the initial mass distribution of Eq. 2.2, the impact rate, R, for a given ejecta is,

$$R(v_{rel}) \propto A(\omega) \left(m_{min}^{-\alpha} - m_{max}^{-\alpha}\right) v_{rel}, \quad \cos\omega = -\frac{\vec{v}_{rel}\cdot\hat{x}}{v_{rel}}, \tag{2.7}$$

where ω is the angle between the detector's bore-sight and the ejecta's relative velocity vector. A is the detectors effective area which is maximal at $\omega = 0$ and zero for $\omega \geq 68°$ [50]. The mass portion of Eq. 2.7 comes from integrating Eq. 2.2 from the minimum to maximum detectable mass. This treatment utilizes the separability of the distributions in Equation 2.2 to treat each simulated ejecta as macro particles representing all masses following the given trajectory. The mass distribution can then be implemented as the fraction of ejecta masses that can be detected by LDEX for the corresponding relative velocity incorporating the velocity dependence of the detectable mass minimum. As we will be comparing the normalized impact rate to the measured impact rate and all other contributions to the impact rate are proportionally constants between ejecta, Eq. 2.6 and Eq. 2.7 are sufficient for calculating the impact rate contributions to the spatial-temporal bins per ejecta.

2.3.3 Comparison to LDEX Data

After the plume data cube is generated, consecutive temporal bins are averaged to match the binning of 3 s used by the impact rate calculation from LDEX data. The error, σ_{R_i}, for each measured impact rate, R_i, was calculated as,

$$\sigma_{R_i} = \frac{1}{\tau\sqrt{R_i\tau}}, \tag{2.8}$$

where $\tau = 3$ s is the sample rate. For each point on the data cube (t_1, x_1, y_1) and point in the discretized (ϕ_0, ϕ_1) parameter space, the value of χ^2 was calculated as,

$$\chi^2(t_1, x_1, y_1, \phi_0, \phi_1) = \sum_i \frac{(R_i - I_i)^2}{\sigma_{R_i}^2}, \tag{2.9}$$

where I_i is the simulated impact rate at position (t_{1+i}, x_{1+i}, y_1). The minimum value of χ^2 corresponds to the most probable value of ϕ_0 and ϕ_1 found by sampling over the entire $(t_1, x_1, y_1, \phi_0, \phi_1)$ grid. In addition, marginalized probability distributions were produced by summing $e^{-\chi^2/2}$ over the other four parameters.

t_1, x_1, and y_1 were limited to all possible flight paths that would intersect at least one nonzero element of the simulated plume. t_1 and x_1 were further restricted in the following way. An outline of the plume was created by sampling to the largest and smallest nonzero x_1 values for each t_1. The start and end points of each simulated flight path were then required to lie outside of this region. This restriction prevents the simulation from fitting the flight path to only half of the plume. y_1 was also truncated to a maximum of 16.7 km as the minimal χ^2 value increases by several orders of magnitude well before this limit for all plumes. Finally, ϕ_0 and ϕ_1 were initially restricted over a range of $0°$ to $45°$ with a coarser grid containing fewer simulated ejecta than the presented results. As the χ^2 values became several orders of magnitude greater beyond $20°$, the maximum simulated cone angle was then restricted to $25°$ for the higher resolution runs presented in the following section.

Note when considering the marginalized probability distributions that the measurement errors given by Eq. 2.8 are actually non-Gaussian despite the probability χ dependence assumed above. Multiple impact rates of zero were also added to the beginning and end of each burst measurement window to minimize the effect of fits to gaps in the simulated impact rate. While these zero measurements are physical, such additions may cause the system to become over-constrained. In addition, restrictions were implemented in the parameter sweep to suppress simulated flight paths where the spacecraft arrives directly above the impact site just before the first ejecta particle reaches that altitude. Such a case would result in a burst measurement of only half the plume. While possible, including these cases results in high degeneracy for the fit. We proceed under this restriction with the justification that majority of the plume detections are unlikely to fit this specific circumstance.

2.4 Results

Considering only LDEX burst measurements containing more than 75 particles, 18 data sets were compared to the simulated plume collected at altitudes spanning from 24 km to 89 km. Figure 2.5 (a) and (b) shows simulated flight paths of minimal χ^2 for three such data sets. Note that one of the burst measurements consists of a single spike in impact rate instead of the usual two. It is for these plumes, primarily, that the restrictions mentioned in the previous section are implemented. Such measurements are expected to coincide with large values of y_1.

To provide an initial guess at the global optimal value for ϕ_0, we first consider the histogram, shown in Figure 2.6 (a), of ϕ_0 values corresponding to minimal χ^2 for each plume. The bin size was chosen as twice the angle parameter step size, $d\phi_0 = d\phi_1$, used in the χ^2 minimization. Note that a similar histogram for ϕ_1 would mean very little as it becomes degenerate with increasing y_1. While this would appear to indicate a ϕ_0 value of 7° or 11°, comparing only the minimal χ^2 values between plumes is susceptible to bias produced from unphysical spikes in the simulated impact rate. Additionally, deviations in fitted ϕ_0 values between plumes have no correlation with altitude, local time, or impact site topography. A clearer picture can instead be derived via the marginalized probability distributions.

Figure 2.5 (c) and (d) shows the marginalized probability distributions of ϕ_0 and ϕ_1 respectively of the three example plumes discussed previously. To produce a global estimate of ϕ_0 and ϕ_1, we summed the marginalized probability distributions over all plumes with equal weight. The result is shown in Figure 2.6 (b) and (c) where the most probable values are $\phi_0 \approx 8°$ and $\phi_1 \approx 0°$. To compare how these values of ϕ_0 and ϕ_1 coincide, consider Figure 2.6 (d) which shows the contour plot of the marginalization of t_1, x_1, and y_1 summed over all plumes.

2.5 Discussion

We presented a particle-based model of impact ejecta plumes generated on the surfaces of airless bodies. Detections of these plumes with in-situ dust detectors yield rich data sets. Unraveling

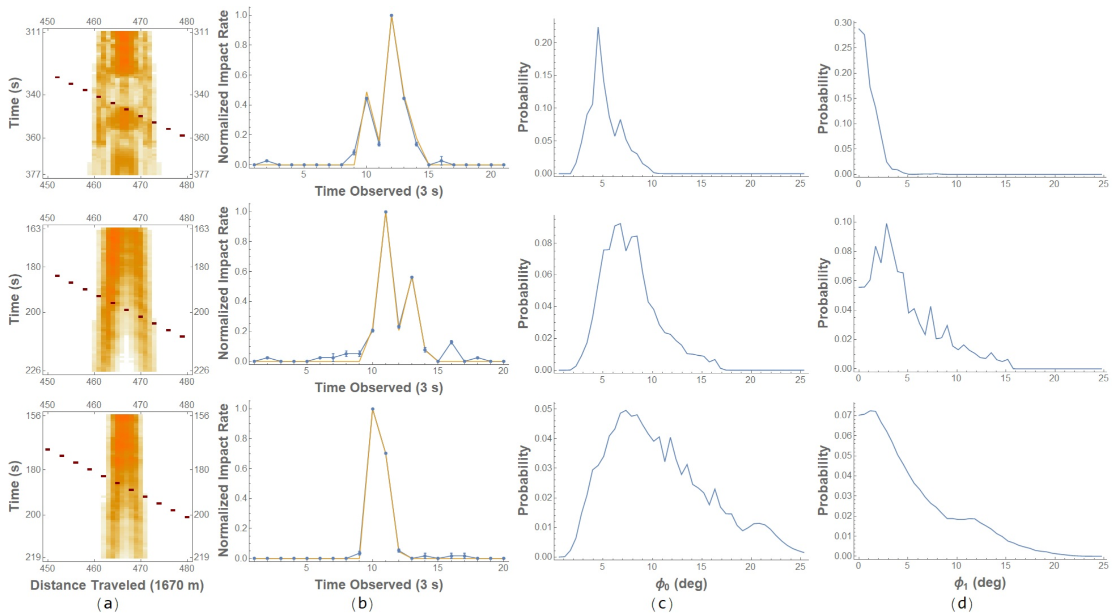

Figure 2.5: Optimal path fits produced from the χ^2 minimization for three burst measurements. **(a)** shows the simulated flight path, represented by a dotted red line, plotted over the simulated impact rates, represented by orange contours, through the plume at optimal y_1 (5.01 km, 11.69 km, and 8.35 km from top to bottom respectively). **(b)** shows the normalized impact rate profile of the simulated path (orange) compared to the corresponding LDEX measurement (blue) with error bars calculated using Eq. 2.8. **(c)** and **(d)** show the marginalized probability distribution functions of the fits for ϕ_0 and ϕ_1. Note that while the ϕ_0 values of least χ^2 for these plumes are 6°, 12°, and 10° from top to bottom, the most probable ϕ_0 values, shown in **(c)**, are more closely aligned at around 7° [17].

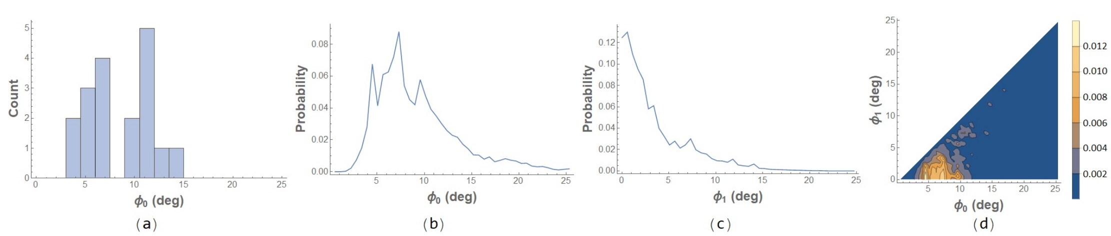

Figure 2.6: **(a)** histogram of the fitted ϕ_0 values for LDEX burst measurements containing more than 75 particles. The bin size was chosen as twice the step size $d\phi_0$ used in the minimization. **(d)** shows the sum over all burst measurement marginalizations with only t_1, x_1, and y_1 marginalized. **(b)** and **(c)** represent the additional marginalization of ϕ_1 and ϕ_0 respectively [17].

the structure of detected plumes requires comparison with model results.

The model presented in this work will allow for future lines of study using the rich LADEE/LDEX dataset. For example, comparing the absolute magnitude of each plume detection gives an estimate of the relative densities of each plume, however, estimating the actual density of a detected plume is a complex matter and is suggested as a future topic of study. In addition, incorporating impact ejecta plumes which generated less impacts than the 18 large plumes discussed in this work would further our understanding of lunar ejecta plumes. Furthermore, the bursts in the LDEX data may not all represent the nominal plumes generated by sporadic meteoroids and may instead be generated by unusually energetic primary impactors. Comparing plumes which may be generated by impactors from a known meteoroid stream such as the Geminids, whose plumes were determined to be from primary impactor particles in the 2 mm to 2 cm size range [113], to plumes which are more likely from the sporadic background and from smaller particles in the 100's of μm size range would better constrain the properties of the primary impactors. We have, however, proceeded with the current fitted initial ejecta distrubtions when constructing the global ejecta model in Chapter 3.

By expanding the Monte Carlo approach used in previous work to three spatial dimensions, updating the ejecta speed distribution, and removing the apex velocity assumption, we have further examined the narrow inner and outer ejecta cone angles, ϕ_0 and ϕ_1, found in [107]. Contrary to the canonically used value of 30° [50, 60] for the impact ejecta curtain angle, we find lunar ejecta plumes to be significantly narrower, with an exterior angle derived from Figure 2.6 (b) of approximately 8 $\pm$ 3°.

The assumption of 30°, however, is not unwarranted as laboratory experiments [23, 6, 10] support similar values. These experiments consisted of different impactors and targets than those generating the lunar impact ejecta plumes and the discrepancy between those experiments and the results of this work could be due to these differences. There is also the concern that as the speed distribution from Equation 2.2 was derived from assuming purely vertical trajectories and perhaps the fitted cone angles are artificially narrow. As a simple check to this, we consider the peak to peak and edge to edge distance of each plume and derive the initial ejecta angle required to defuse that far from the plume's center assuming the particle is at the apex of its trajectory. The reasoning being that ejecta at their apex should make up the densest part of the measured plume due to their increased flight time at that altitude for the peak to peak comparison while the edge to edge comparison gives an upper limit on the outer ejecta cone angle. From the 18 plumes, we derive average initial ejecta angles of $5 \pm 2°$ for the peak to peak case and $12 \pm 4°$ for the edge to edge case. Therefore, the fitted $8 \pm 3°$ is within expectation while an outer cone angle of 30° is not representative of the plumes observed by LDEX.

Another possible explanation for the narrow ejecta outer cone angles is that the plumes observed by LDEX are 'reverse' plumes. Reverse plumes are narrow high velocity plumes produced shortly after the initial plume cone is generated due to swift collapse of the crater or impactor breakdown. Such reverse plumes have been observed during both the Deep Impact [94] and LCROSS [47] missions as well as their complimentary laboratory experiments. While those observed during the Deep Impact and LCROSS missions are due to impactor breakdown, reverse plumes are also produced from highly porous, low density targets with high speed impactors, criteria which the lunar meteoroid environment fulfills [95, 94, 47].

Further work is necessary to determine if this is indeed the case. However, preliminary results suggest that, in the case of a reverse plume, we do not observe a 30° additional outer cone of the same speed distribution. If such a broad plume component exists, it must be ejected at speeds less than ~ 300 m s^{-1} else LDEX would have detected it at the lowest altitude plume considered here of 24 km. Thus, the reverse plume component would dominate the lunar dust environment at the altitudes observed by LDEX. Regardless of whether the observed LDEX bursts are the result of reverse plumes or a single $8 \pm 3°$ cone, this finding allows us to better understand the structure of the lunar impact ejecta cloud, the extent to which lunar material is redistributed due to meteoroid impacts, and has refined our understanding of the physics of high-speed impactors into regolith targets. While this chapter focused on the impact ejecta processes occuring at the Moon, its results may be applicable to the broad class of regolith dominated bodies throughout the solar system such as asteroids, Jupiter trojans, and Edgeworth-Kuiper Belt Objects.

Chapter 3

Global Lunar Ejecta Model

3.1 Introduction

Constraints on mass yields, the ratio of the total mass of the produced dust ejecta over the mass of the initial impacting particle, are necessary for deriving impactor fluxes from modeled ejecta clouds. While the relationship between impactor mass, speed, and mass yield has been measured in a variety of experiments [58, 57, e.g.], these do not cover the relevant impactor compositions, sizes, speeds, nor characteristics of the surface regolith for the lunar environment. As such, this chapter focuses on constraining the product of impactor flux and mass yield per source via a forward modeling approach expanding the single plume model from Chapter 2 to a global one. β-meteoroids, dust grains on hyperbolic orbits moving away from the Sun, have been suggested to be an additional source of impact ejecta at the Moon due to the persistent dust ejecta density enhancement on the Moon's sunward side [109]. Because of this, we also explore the possibility of β-meteoroids producing observable impact ejecta [109].

3.2 Particle Discretization

Ejecta for each impact plume were modeled discretely similar to Chapter 2, describing the initial ejecta velocity (v), mass (m), and angle from surface normal (ϕ) distributions as Equation 2.2 with the outer and inner ejecta cone angles, ϕ_0 and ϕ_1 (see Figure 3.1), fixed to 8° and 0° respectively [118, 117, 50, 17]. While [92] suggests coupled speed and size ejecta distributions, the ejecta distributions used here are treated as separable as there is a lack of altitude dependence in the detected impact charge distribution of LDEX [17, 50]. For simulating the contribution of a single plume's ejecta to LDEX's measured ejecta impact rate, we sampled 200,000 simulated ejecta particle trajectories based on $f(\phi)$ and $f(v)$. Positions and velocities for each simulated particle trajectory were calculated at fixed time steps of $dt = 1$ s using elliptical orbit equations from Equation 2.4 and 2.5. As LDEX's lowest detectable mass threshold is velocity dependent, $f(m)$ was again implemented as a weight for the simulated impact rate. Now, however, we are not comparing normalized impact rates and the goal is to derive physical quantities from this model. As a more explicit version of Equation 2.7, the impact rate from ejecta into LDEX, I_i, for impact i becomes [118],

$$\begin{aligned} I_i &= \frac{R_i}{dV} = \frac{A(\omega_i)}{dV}\cos(\omega_i)\frac{(C_m v_{rel}^{-4.76})^{-\alpha} - m_{max}^{-\alpha}}{m_{min}^{-\alpha} - m_{max}^{-\alpha}} v_{rel}, \\ \cos\omega_i &= -\frac{\vec{v}_{rel}\cdot\hat{x}}{v_{rel}}, \\ \vec{v}_{rel} &= (v_\theta\cos\phi_i - v_{sc})\hat{x} + v_\theta\sin\phi_i\hat{y} + v_r\hat{r}, \end{aligned} \tag{3.1}$$

where v_{sc} is the spacecraft speed with $\hat{x}$ chosen in the direction of the spacecraft velocity vector, ω is the angle between the detector's boresight and the ejecta's relative velocity vector, v_{rel}, dV is the simulated volume element, and A is the detectors effective area which is maximal at $\omega = 0$ and zero for $\omega \geq 68°$ [50]. Each plume in this model is assumed to have the same initial ejecta distributions. Effects of impactor mass, speed, and obliquity of the impact are contained entirely within the mass yield (total mass of ejecta per plume divided by the mass of the impactor) and the impactor flux (number of plumes per spatial-temporal bin). This is done for simplicity as such effects are not sufficiently constrained over the relevant impact parameters. Formulating these additional effects, particularly asymmetric plumes produced from oblique impacts, could lead to a possible improvement of this model.

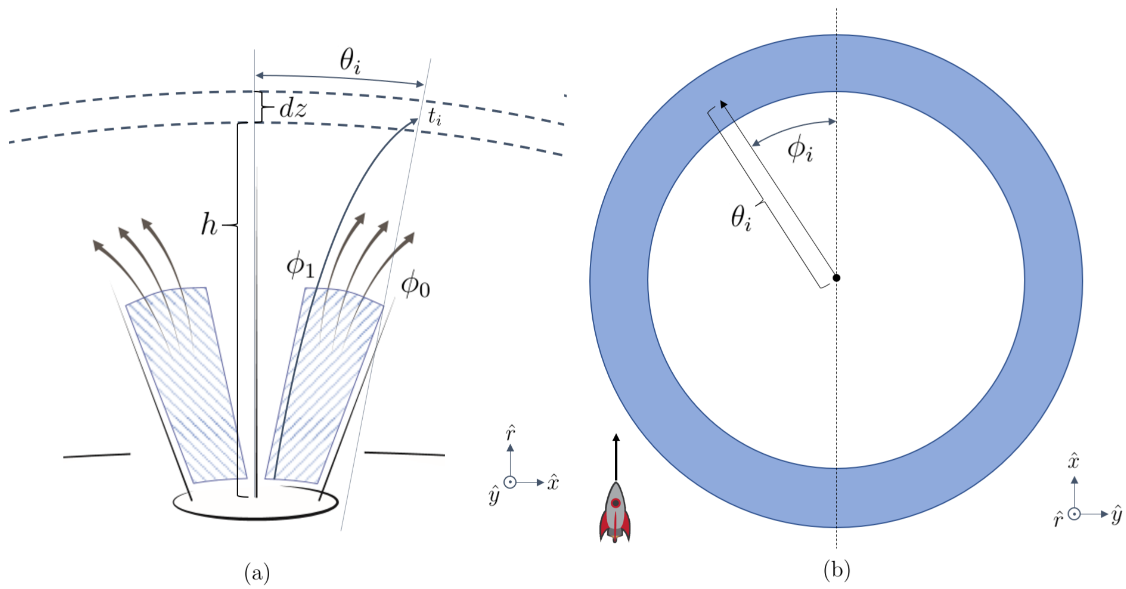

Figure 3.1: Illustration of a simulated dust plume **(a)** side-view and **(b)** top-view for the parameters relevant to the global ejecta model. Discretized impacts are characterized by (t_i, θ_i, ϕ_i) with velocity components v_r and v_θ determined from initial ejecta speeds and angles. Note that $\hat{r}$ is the direction normal to the lunar surface while $\hat{x}$ is the direction of the spacecraft velocity vector also demonstrated by the rocket (to indicate LADEE) in **(b)** [14].

3.3 Multiple Plume Model

3.3.1 One Bin

For simulating the contribution of multiple plumes to the detected impact rate, we first consider the simplified case of a single volume element, dV, with constant impactor flux, Φ_{imp}. For a single simulated particle at time t_i and azimuthal angle ϕ_i with respect to the plume's origin and spacecrafts velocity (Figure 3.1), the contribution to the simulated impact rate, I_i, is given by Equation 3.1. Thus the measured average impact rate of LDEX, I_{LDEX}, is

$$I_{LDEX} = N_p \frac{M_p}{M_s} \sum_i I_i, \tag{3.2}$$

where N_p is the total number of plumes produced per simulated time step within the lunar surface element (dA), M_p is the average total mass of one plume, and M_s is the simulated mass of one plume. The simulated mass of one plume consists of the sum of all particles in the simulation multiplied by the average mass, based on the distribution from Equation 2.2, while we treat the total mass of an actual plume as an unknown quantity. Note that there are some additional complications to the total simulated mass, as the azimuthal component is treated as continuous while the initial ejecta distributions are sampled discretely. Since the impactor mass flux for characteristic impactor mass m_{imp} can be written as $\Phi_{imp} = m_{imp}N_p/dA$, we rewrite Equation 3.2 as

$$\begin{aligned} I_{LDEX} &= \frac{N_p}{dV}\frac{M_p}{M_s}\sum_i R_i \\ &= \frac{N_p}{dA}\frac{R_m^2}{\int_{R_m+h}^{R_m+h+dz} r^2 dr}\frac{M_p}{M_s}\sum_i R_i \\ &= Y\Phi_{imp}\frac{3R_m^2}{(R_m+h+dz)^3-(R_m+h)^3}\frac{1}{M_s}\sum_i R_i, \end{aligned} \tag{3.3}$$

where h is the altitude of the spacecraft, $Y = M_p/m_{imp}$ is the mass yield of a plume, and dz is the altitude bin size (Figure 3.1). Matching the simulation to LDEX data is then a matter of scaling $Y\Phi_{imp}$.

3.3.2 Multiple Bins

The previous case holds true for a constant impactor flux within the lunar surface patch considered. As the lunar impactor flux varies with local time, we expand this approach by considering local time bins assuming that each bin encompasses a constant impactor flux. To standardize the notation of the following sections, i denotes a simulated impact sampled from ejecta particle trajectories as described in Section 3.2. A subscript of k denotes the observing surface-altitude bin (i.e., the bin which contains the measured impact rate) while j denotes the surface bin being observed (i.e., surface patch possibly containing the plume origin, corresponding to simulated impact i). Thus the subscript of dA_{ijk} is read as 'for simulated ejecta measurement i originating from surface bin j as measured within surface-altitude bin k.'

One subtlety that was glossed over in the one bin case was the location of dA relative to dV, as dA is only located directly beneath dV in the case where the angular distance of the simulated impact from the center of the plume, $\theta_i = 0$. For a single simulated impact at time t_i and position (θ_i, ϕ_i) relative to the center of the plume, dA is shifted from surface patch corresponding to dV.

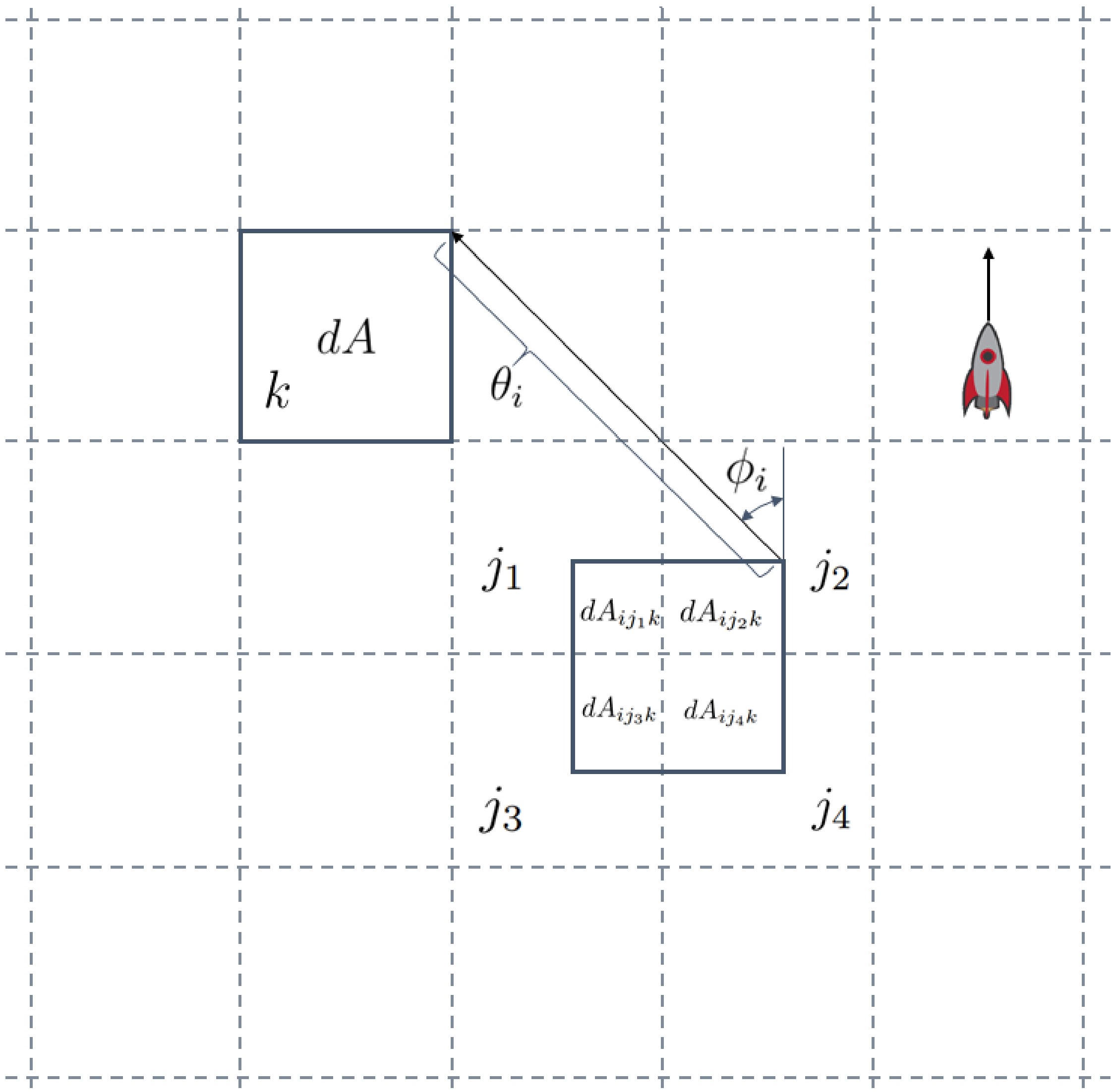

Figure 3.2: Illustration of the possible plume impact location for a given simulated ejecta measurement i relative to the surface patch dA directly below the simulated volume element dV. This possible plume location is characterized by the projection of surface element dA given that the simulated measurement traveled a great circle distance of θ_i at an angle ϕ_i with respect to the spacecrafts velocity. Dashed lines represent local time-latitude bins each with a constant flux. For the illustrated case, simulated impact i has contributes from bins j_1 and j_2 weighted by the area ratio in Equation 3.4. Note that k is also binned by altitude with the corresponding bin determined by the height of simulated ejecta impact i [14].

Thus, for a particular (θ_i, ϕ_i), the corresponding dA can overlap multiple local time bins (up to four in the case of an equal area square grid as shown in Figure 3.2).

For the illustrated case in Figure 3.2, dA projected from bin k overlaps fixed surface bins j_1, j_2, j_3, and j_4 with surface areas dA_{ij_1k}, dA_{ij_2k}, dA_{ij_3k}, and dA_{ij_4k}, respectively. This simulated impact contribution to the measured impact rate is

$$\begin{aligned} I_{ik} &= \frac{M_p}{M_s} R_i \left(\frac{N_{ij_1k}}{dV} + \frac{N_{ij_2k}}{dV} + \frac{N_{ij_3k}}{dV} + \frac{N_{ij_4k}}{dV} \right) \\ &= \frac{M_p}{M_s} R_i \frac{3R_m^2}{(R_m+h+dz)^3 - (R_m+h)^3} \left(\frac{N_{ij_1k}}{dA} + \frac{N_{ij_2k}}{dA} + \frac{N_{ij_3k}}{dA} + \frac{N_{ij_4k}}{dA} \right) \\ &= \frac{1}{M_s} R_i \frac{3R_m^2}{(R_m+h+dz)^3 - (R_m+h)^3} Y \left(\Phi_{j_1} \frac{dA_{ij_1k}}{dA} + \Phi_{j_2} \frac{dA_{ij_2k}}{dA} + \Phi_{j_3} \frac{dA_{ij_3k}}{dA} + \Phi_{j_4} \frac{dA_{ij_4k}}{dA} \right), \end{aligned} \tag{3.4}$$

where Φ_{j_1}, Φ_{j_2}, Φ_{j_3}, and Φ_{j_4} are the impactor fluxes for surface bins j_1, j_2, j_3, and j_4, respectively. Note, it is with the assumed constant flux that $\Phi_j = m_{imp} N_{ijk}/dA_{ijk}$ for each i and k. Expanding this to all j bins and summing over all simulated impacts i gives the generalized form of Equation 3.3,

$$\begin{aligned} I_{LDEX,k} &= \frac{3R_m^2}{(R_m+h+dz)^3 - (R_m+h)^3} \frac{1}{M_s} \sum_{ij} Y \Phi_j R_i \frac{dA_{ijk}}{dA} \\ &\equiv \sum_j Y \Phi_j S_{jk}. \end{aligned} \tag{3.5}$$

Matching all surface and altitude bins of data becomes a minimization with $Y\Phi_j$ as parameters. In this formulation, the values of S_{jk} contain all of the geometric information from the numerical simulation separated from the desired parameters to be estimated. Specifically, R_i contains the geometry of the instrument while the rest of S_{jk} contains the geometry of the system.

3.3.3 Latitude Variation

3.3.3.1 Grid Motivation

While the latitude coverage of the LDEX data set is limited (Figure 3.3), expanding this model to a full three dimensional sphere may prove useful for future data sets, as well as to minimize errors introduced by assuming a purely equatorial orbit. In the case of a grid covering the entire surface of

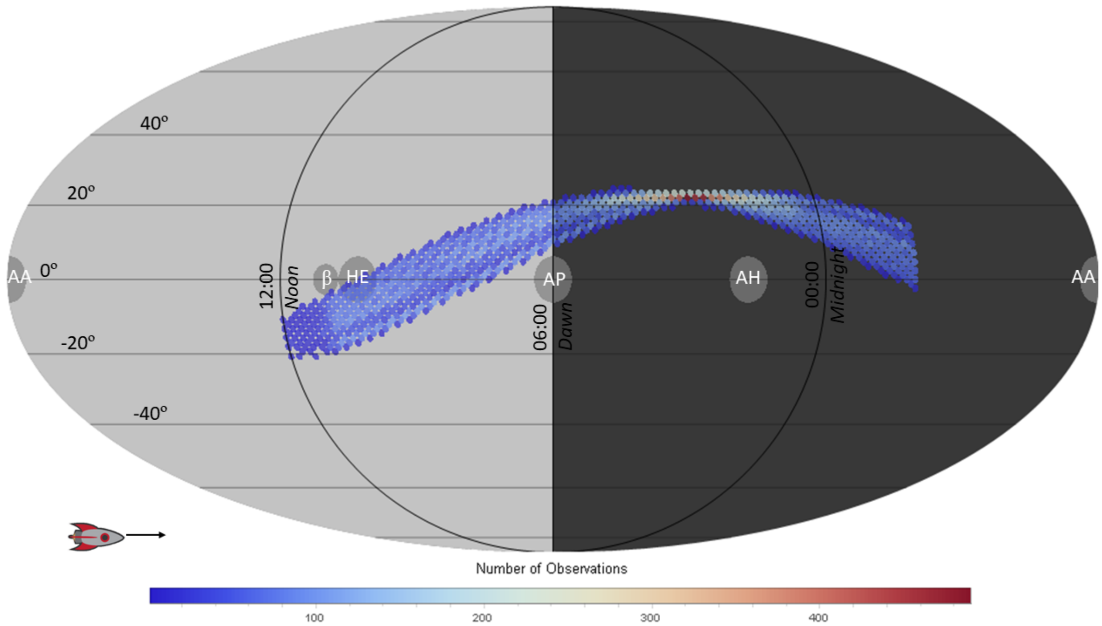

Figure 3.3: Histogram of LDEX data used in the fit binned by the surface grid described in Section 3.3.3.1. Note that this grid is in local time with the transition from white to dark regions corresponding to sunset and sunrise. Impact rate measurements were selected for periods when LDEX's boresight was along the spacecraft's velocity vector and the Sun was not within the instrument's field of view [49]. Additionally, measurements within 5 days of the identified Geminids and Quadrantids meteor shower times [116] were removed. As indicated, LADEE was moving across this map from left to right on its retrograde orbit about the Moon. The radiants of the sporadic meteoroid sources bombarding the Moon are also indicated [112, 14].

a sphere, Equation 3.5 still holds true with different values for dA_{ijk}. However, complications arise with the increasing number of parameters and computation time. For example, surface grid cells defined by equal latitude and longitude steps are no longer of equal area, as was the case in Figure 3.2, and whose overlap with arbitrary θ_i and ϕ_i proves computationally expensive to perform for each simulated impact.

Polygonal grids, even when approximately equal in area and shape, also introduce an additional parameter in relative orientation of the projected cell to the considered cell. For example, In the case of Figure 3.2, dA_{ij_1k} would have a different value from the one illustrated if the projected square was tilted by an arbitrary angle.

Here we use overlapping spherical caps as surface grid cells with grid points defined as the center of these spherical caps (Figure 3.4). As this will introduce error in the form of surface

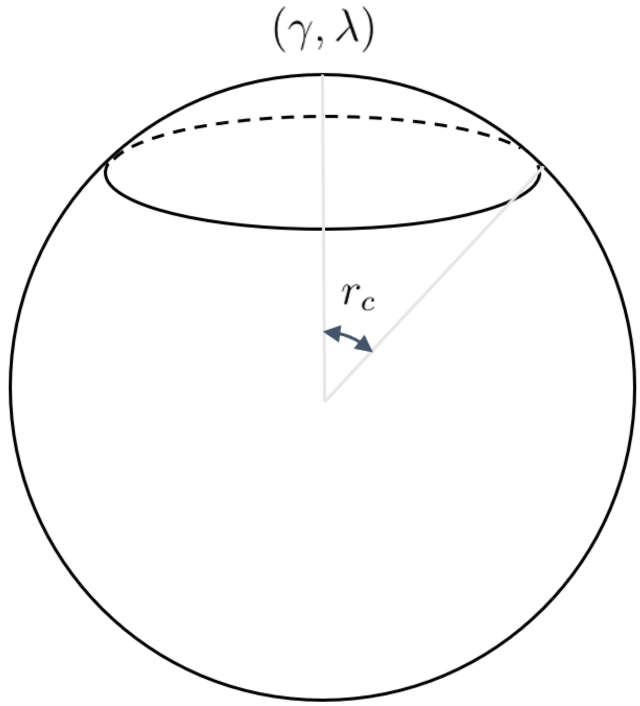

Figure 3.4: Illustration of an exaggerated spherical cap used to discretize the surface area of a sphere. Each surface grid cell is defined by it's center point latitude and longitude (γ, λ) as well as angular radius r_c [14].

patches not covered or double counted, we construct the grid cell size such that the sum of all surface grid cell areas equals the surface area of the sphere. This represents our best estimate, as the double counted regions should come close to accounting for the regions not covered by the cells. Additionally, surface grid cells are positioned to meet the following criteria:

- Maximize the smallest distance between any two grid points.
- Minimize the number of unique grid point to grid point distances within an effective range.

The first criteria is imposed to achieve a close to uniform covering of the sphere while the second criteria is imposed to reduce the computation time of the simulation. As the distance between grid points will become a parameter in determining S_{jk} (Equation 3.7-3.8), reducing the number of unique grid point to grid point distances significantly increases the performance of the simulation. The 'effective range' mentioned in the criteria (and Appendix Figure 3.6) refers to surface grid cells within the maximum θ_i of all simulated impacts plus two times the radius of the surface grid cells as any cell beyond this range does not contribute to the simulated impact rate. We used the HEALPix framework [38] to generate the locations of these grid cells as it has reasonable agreement with our criteria with the flexibility to scale the resolution as needed. To balance accuracy with computation time, we chose a resolutions of $N_{side} = 2^5$ resulting in 12288 surface grid cells.

3.3.3.2 Grid Derivation

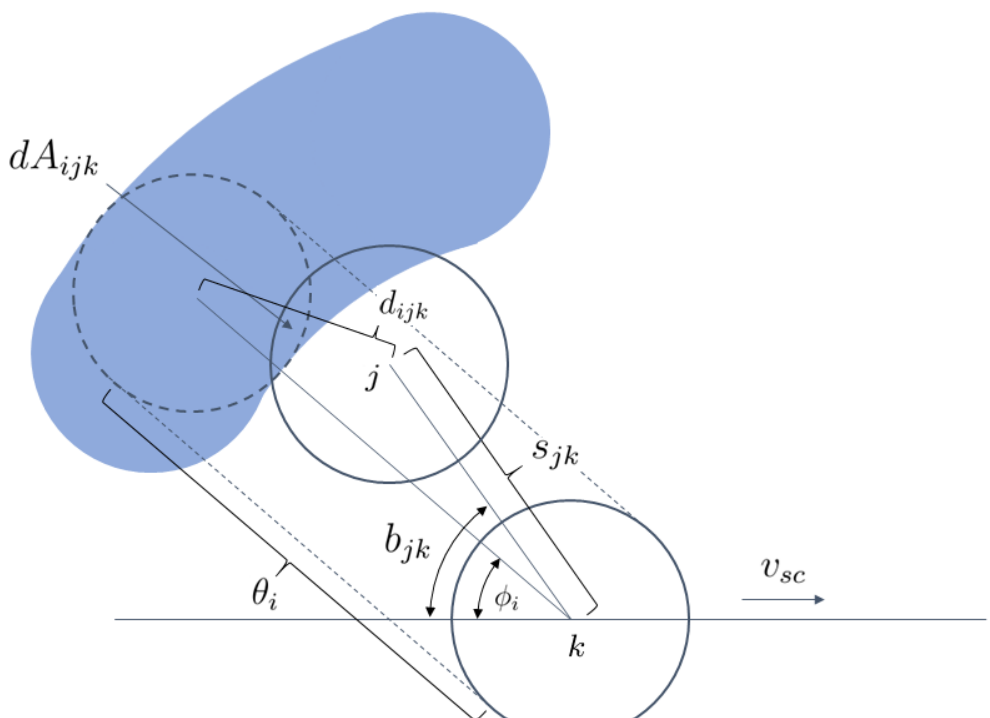

Figure 3.5: Illustration of the area overlap dA_{ijk} of impact i projected from cell k with cell j. Spherical cap k represents the surface bin below the surface-altitude bin where simulated ejecta measurement i is collected. The dotted circle indicates where on the surface ejecta i could have come from given that it traveled a great circle distance θ_i at an angle ϕ_i with respect to the spacecraft's velocity v_{sc}. To determine the contribution of surface grid cell k on the simulated ejecta measurement i, dA_{ijk} must be calculated from d_{ijk} using Equation 3.7. d_{ijk} is calculated from s_{jk}, b_{jk}, and ϕ_i using Equation 3.8. The blue shaded region indicates the change in the overlapping area as ϕ_i is integrated [14].

To achieve the area described in Section 3.3.3.1, the angular radius (r_c) of the spherical caps is given as

$$\cos r_c = 1 - \frac{2}{N_{grid}}, \tag{3.6}$$

where $N_{grid} = 12288$ is the number of grid cells on the surface. To calculate dA_{ijk} in Equation 3.5, we use the following equation for the overlap between two spherical caps of radius r_c separated by a great circle distance between their centers of d_{ijk} [119],

$$\frac{dA_{ijk}}{dA} = \frac{\pi - \arccos\left(-\cot^2 r_c + \cos d_{ijk} \csc^2 r_c\right) - 2\arccos\left(\cot r_c \tan \frac{d_{ijk}}{2}\right)\cos r_c}{\pi(1-\cos r_c)}. \tag{3.7}$$

Note that for this section, k denotes the surface bin directly below the surface-altitude bin under consideration. Additionally, the great circle distance between the projected area of a simulated impact (θ_i, ϕ_i) and surface grid cell j is given by the spherical law of cosines

$$\cos d_{ijk} = \cos\theta_i \cos s_{jk} + \sin\theta_i \sin s_{jk} \cos(\phi_i - b_{jk}), \tag{3.8}$$

where s_{jk} is the great circle distance between surface grid cells j and k, and b_{jk} is the bearing of surface grid cell j with respect to the latitude line of cell k (Figure 3.5). s_{jk} and b_{jk} are given in terms of latitude, γ, and longitude, λ, as,

$$\begin{aligned} s_{jk} &= 2\arctan\sqrt{\frac{\sin^2\frac{\gamma_j-\gamma_k}{2} + \cos\gamma_j\cos\gamma_k\sin^2\frac{\lambda_j-\lambda_k}{2}}{1-\sin^2\frac{\gamma_j-\gamma_k}{2} - \cos\gamma_j\cos\gamma_k\sin^2\frac{\lambda_j-\lambda_k}{2}}}, \\ b_{jk} &= \arctan\left(\frac{\cos\gamma_k\sin\gamma_j - \sin\gamma_k\cos\gamma_j\cos(\lambda_j-\lambda_k)}{\sin(\lambda_j-\lambda_k)\cos\gamma_j}\right). \end{aligned} \tag{3.9}$$

Using Equation 3.7-3.9, dA_{ijk} becomes a function of $(\theta_i, \phi_i, s_{jk}, b_{jk})$ where s_{jk} and b_{jk} need only be calculated once when the grid is generated. Combining this with Equation 3.1 and Equation 3.5, results in the equation for simulated impact rate S_{jk} as a function of $(v_\theta, v_r, \theta_i, \phi_i, s_{jk}, b_{jk})$ summed over simulated impacts i.

3.3.3.3 Minimization

With the S_{jk} values simulated for Equation 3.5 over all relevant surface-altitude bins, we can fit the measured LDEX data $I_{LDEX,k}$ using the parameters $Y\Phi_j$. Starting with a least-squares approach, we minimize

$$\epsilon_{tot}(Y\Phi_j) = \sum_k (I_{LDEX,k} - \sum_{j=1}^{n} Y\Phi_j S_{jk})^2 = \sum_k (I_{LDEX,k} - I_{fit,k})^2. \tag{3.10}$$

With no additional constraints, n is the number of surface grid cells. To directly connect to physical quantities, we will use the four dominant impactor sources: helion (HE), antihelion (AH), apex (AP), and anti-apex (AA). HE, AH, AP, and AA are equatorial sources at local times of 10.3 LT, 1.7 LT, 6 LT, and 18 LT respectively [112]. Each bins $Y\Phi_j$ is broken up by source α

$$Y\Phi_j = \sum_{\alpha=1}^{4} Y\Phi_\alpha \cos^3(s_{j\alpha})\Theta(s_{j\alpha} - \pi/2), \tag{3.11}$$

where $\cos^2(s_{j\alpha})$ comes from how Y scales with impact angle and $\cos(s_{j\alpha})\Theta(s_{j\alpha} - \pi/2)$ from the surface area projection of Φ_α using the Heaviside function Θ [114]. Equation 3.9 is used for $s_{j\alpha}$ with the (γ, λ) of the impactor source radiant used for one of the entries. With this substitution, $I_{fit,k}$ takes the form of a linear sum

$$I_{fit,k} = \sum_{\alpha=1}^{4} Y\Phi_\alpha \sum_{j=1}^{n} S_{jk} \cos^3(s_{j\alpha})\Theta(s_{j\alpha} - \pi/2) = \sum_{\alpha=1}^{4} Y\Phi_\alpha x_{\alpha k}. \tag{3.12}$$

In this form, the minimization is now a linear regression without a constant bias, $Y\Phi_\alpha$ are the regression coefficients, and $x_{\alpha k}$ are the independent variables. Since the dependence of Y on obliqueness of an impact is described by $x_{\alpha k}$, Y now represents the mass yield for impacts with normal incidence to the surface.

3.3.3.4 Optimization

With the addition of latitude variation in the form of Equation 3.7-3.9, the production of S_{jk} in Equation 3.5 becomes computationally expensive. To increase efficiency, the structure of the simulation follows that of Figure 3.6. We note that steps G1-3 rely only on the number and radius of the surface grid cells with G4 containing the additional information of the geometry of the instrument while S1-2 contain all of the ejecta particle dynamics of a plume. Thus G1-4 does not need to be recalculated with additional ejecta dynamical information, such as collisions or different initial ejecta distributions to be possibly evaluated in the future. As the dependence of S_{jk} on b_{jk}

closely follows that of $A\cos(b_{jk}) + B$, we chose to only evaluate at $b_{jk} \in \{0, \frac{\pi}{2}, \pi\}$ and use this fitted function to calculate all other b_{jk}. This results in increased performance with the additional benefit of allowing for changes in spacecraft bearing. Any such variation in bearing need only require repeating the last part of S3 which can be done in a matter of seconds. This performance gain is one of the benefits of the circular symmetry of the spherical caps used for the surface grid cells.

3.4 Results

Using the LDEX impact rate measurements with coverage shown in Figure 3.3, fitted values for $Y\Phi$ were calculated for the three equatorial source radiants 10.3 LT, 1.7 LT, and 6 LT corresponding to HE, AH, and AP respectively. These sources are labeled by their radients in Figure 3.7 as these values represent all possible sources originating from that direction, not just HE, AH, and AP. We excluded data within 5 days of the Geminid and Quadrantid meteor showers to isolate the contribution from sporadic background sources [116]. The segment of data coverage in Figure 3.3 from 12 LT to 22 LT was excluded from the fit as the Sun was within LDEX's field of view generating elevated noise levels in the instrument. As this excluded range covers the majority of the 18 LT (AA) source's contribution to the lunar ejecta environment, the AA source was not included in this fit. Similarly, non-equatorial sources such as the northern and southern toroidal (NT/ST) that may also contribute to ejecta production [112] were not included as the latitude coverage of Figure 3.3 is not sufficient to isolate their contribution from that of the AP source. Using the ejecta mass production weights from this latitude coverage for AP and NT/ST sources, $w_{AP} = 0.303$ and $w_{NT/ST} = 0.303$ respectively [112], we estimate the possible contribution to 6 LT from these sources. Assuming a latitude of 60° for the NT source, the relative expected contribution is derived as,

$$\frac{w_{NT}\cos^3(60^\circ - 18^\circ)}{w_{AP}\cos^3(18^\circ - 0^\circ)} = 0.22, \tag{3.13}$$

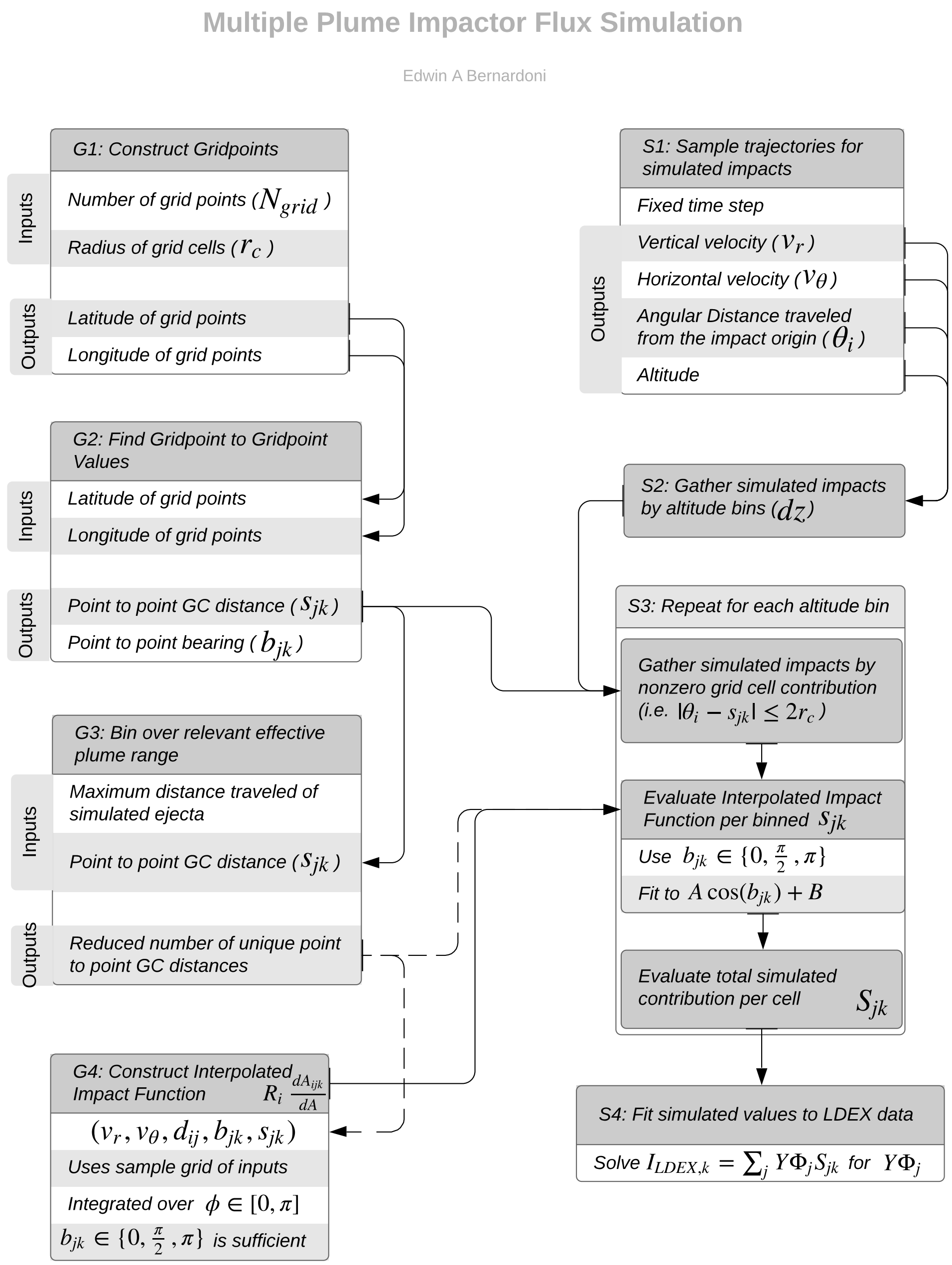

Figure 3.6: Schematic of the simulation's order of operations for the multiple plume model with latitude variation. G1-3 depends only on the number and size of the surface grid cells while G4 contains information on the geometry of the instrument. Separate from these factors, S1-2 contains all of the dynamics of the plume. Thus, G1-4 need not be recalculated with additional ejecta dynamics such as introducing collisionality or changes in the initial ejecta distributions. The fit for the second part of S3 means that changes in bearing of the instrument need only require recalculation of the last part of S3 [14].

where 18° is the average latitude of all LDEX measurements taken near 6 LT (see Figure 3.3). While we assume that the entirety of the 6 LT source is from AP meteoroids for the following discussion, note that up to 22% may be from toroidal sources.

Note that the fitted values for $Y\Phi$ are highly dependent upon m_{max}, partially from the weight in Equation 3.1, but primarily from M_s in Eqs. 3.2-3.5. For this reason, we include estimates for $m_{max} = 10^{-8}$ kg (opaque points in Figure 3.7) corresponding to 100 μm ejecta taken as the peak in the sporadic background mass distribution and for $m_{max} = 10^{-11}$ kg (transparent points in Figure 3.7) corresponding to 10 μm ejecta and the largest ejecta particle detected by LDEX. The error bars for Figure 3.7 represent the standard error of that parameter for the linear regression. As shown in Figure 3.7, 6 LT (AP) is the dominant contributing source to the lunar dust environment for both cases with a mission averaged impact ejecta mass production (mass yield times impactor mass flux) of $(1.62 \pm 0.02) \times 10^{-14}$ kg m^{-2} s^{-1} for $m_{max} = 10^{-8}$ kg and $(7.29 \pm 0.07) \times 10^{-15}$ kg m^{-2} s^{-1} for $m_{max} = 10^{-8}$ kg at normal incidence or 14.6 ± 0.1 t day^{-1} and 6.6 ± 0.1 t day^{-1}, respectively, averaged over the entire lunar surface. However, the asymmetry between HE and AH sources observed in prior studies [114, 54] remains despite considerations for the spacecraft's trajectory with mission averaged values of 10.5 ± 0.1 t day^{-1} and 4.7 ± 0.1 t day^{-1} for the HE source and 4.9 ± 0.1 t day^{-1} and 2.2 ± 0.1 t day^{-1} for the AH source. This asymmetry runs counter to expectation as models of the sporadic background do not indicate a significant asymmetry between the HE and AH impactor fluxes and impactors for the two sources should be of similar size and speed, and thus mass yield [86]. The ground based radar observations are somewhat less clear as there are observations suggesting symmetry [54] and others suggesting an asymmetry between the influx from the HE and AH sources throughout the year [21]. As the total meteoroid flux measured at Earth is 43 t day^{-1}, we expect a total impactor flux of a few tons per day for the lunar environment [112, 22]. Thus these fitted values for the three primary impactor sources suggest yields on the order of 10 consistent with [112].

As to whether the HE/AH asymmetry is an enhancement on the dayside of the moon or a deficit on the nightside is unclear. However, as we only have possible physical explanations for

Figure 3.7: Values for the mass yield times impactor mass flux averaged over the entire lunar surface (total lunar ejecta mass flux) per sporadic background source radiant fitted to LDEX measurements binned in synodic day increments. These values are produced from scaling $(Y\Phi_\alpha)$ in Equation 3.12 to the Moon's cross section using $m_{max} = 10^{-8}$ kg (opaque points) and $m_{max} = 10^{-11}$ kg (transparent points). The opaque and transparent points are staggered for clarity. Measurements only include those with quality flags of 3 or greater excluding data within 5 days of the identified Geminid and Quadrantid meteor showers and values between 12 and 22 LT. Error bars for each fit represent the standard error for each parameter in the linear regression [14].

an enhancement on the dayside, we will proceed under that assumption. For comparison, the following section introduces the empirical formula fit from [86] into our model. It should be noted that while a thermal dependence on the soil's mass yield has been suggested as a potential cause for this enhancement, no physical mechanism has been proposed to link the temperature of the lunar surface to its impact ejecta yield nor has there been any experimental evidence to suggest that this is the case. As a possible physical explanation, we discuss the potential contribution from β-meteoroids as an additional impactor source in the proceeding section [109].

3.4.1 Yield Variance

Our understanding of how the lunar regolith responds to meteoroid bombardment is limited. Effects such as surface temperature, UV radiation, or solar wind have been suggested as possible drivers that may enhance ejecta mass production on the lunar dayside [54, 86]. An emperical relation for the "excess" dayside lunar ejecta was found by comparing to expectations from dynamical models [86]. To incorporate this effect within our model, we introduce the following term into $S_{j\alpha}$ of Equation 3.12 as a function of local time per surface bin [86],

$$Y_T(LT_j) = \begin{cases} 1 & |LT_j - 12| \geq 6 \\ 1 + .81(1 - |12 - LT_j|/6) & |LT_j - 12| \leq 6 \end{cases} \tag{3.14}$$

With this additional local time dependence on the mass yield, we reproduce Figure 3.7 for $m_{max} = 10^{-8}$ kg as Figure 3.8. Note that the fitted values plotted are of the Y on the lunar nightside as the enhancement on the dayside is absorbed into $S_{j\alpha}$. Under this empirical formula, HE and AH sources have a much closer agreement with mission averaged values of 5.9 ± 0.1 t day^{-1} for the HE source and 5.0 ± 0.1 t day^{-1} for the AH source. It should be noted that this formula is derived from the observed HE/AH asymmetry in lunar ejecta and not from surface response relations.

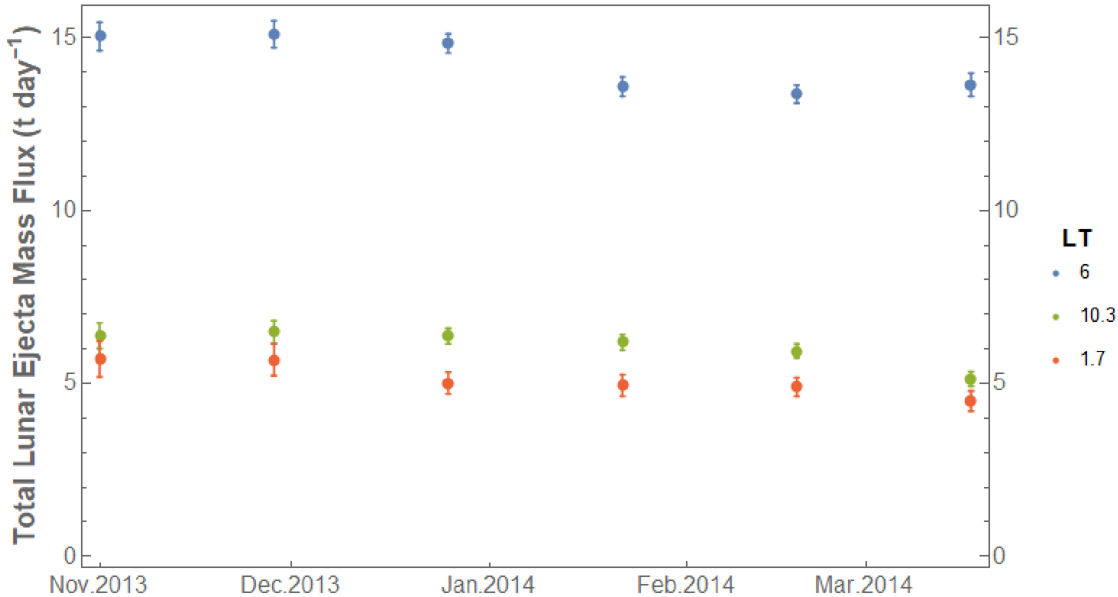

Figure 3.8: Values for the mass yield times impactor mass flux averaged over the entire lunar surface (total lunar ejecta mass flux) per sporadic background source derived from Figure 3.7 with the additional contribution of Equation 3.14. Note that the yield in these fitted values should be treated as the lunar nightside yield as the enhancement on the dayside is pulled into $S_{j\alpha}$ in Equation 3.12 [14].

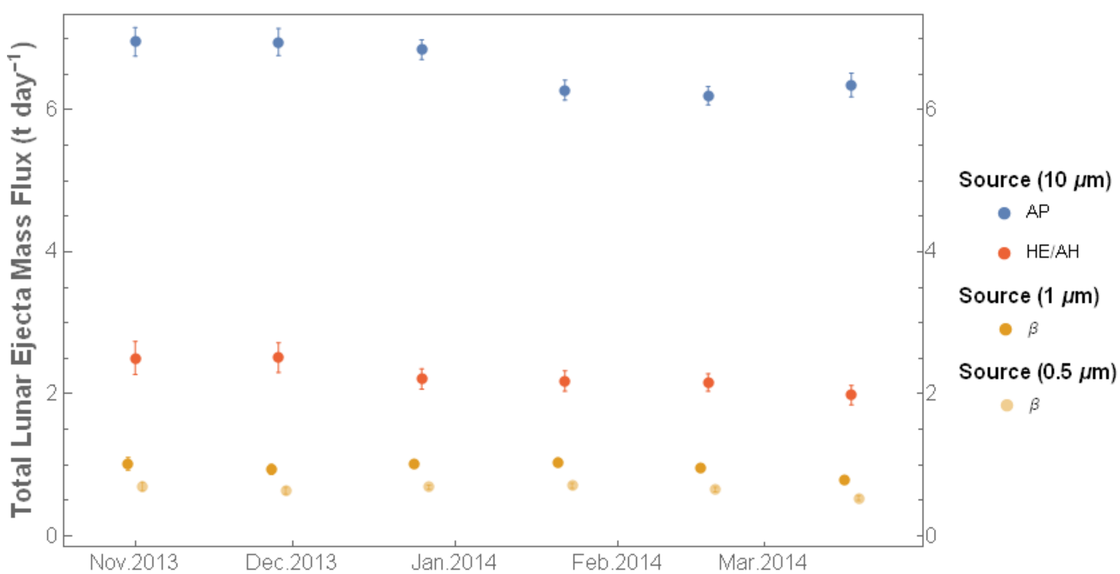

Figure 3.9: Values for the mass yield times impactor mass flux averaged over the entire lunar surface (total lunar ejecta mass flux) per sporadic background source derived from Figure 3.7 with $m_{max} = 10^{-11}$ for the sporadic background sources using $m_{max} = 10^{-14}$ kg (opaque points) and $m_{max} = 10^{-15}$ kg (transparent points) for the β-meteoroid source. The opaque and transparent points are staggered for clarity. As β-meteoroids are of a similar radiant as the HE source, $Y\Phi$ for the β-meteoroids were estimated by requiring that the total lunar ejecta mass flux for the HE source equal that of the AH source derived from Figure 3.7 [14].

3.4.2 β-meteoroids

As a possible physical explanation for the excess dayside impact ejecta, we consider the contribution of an additional impactor source, β-meteoroids [109]. Since β-meteoroids are of a similar radiant to the HE source at 11 LT [109], we would expect an enhancement of the total lunar ejecta mass flux on that side. As such, we label the HE/AH contribution as the lower of the two in Figure 3.9. We cannot take the difference between the total ejecta mass flux of 10.3 and 1.7 LT fitted values as the β-meteoroid contribution as the mass distribution of ejecta may not be the same as that of Equation 2.2. However, when considering the ejecta size distributions per local time bin, the values for α remains consistent with no significant deviations from the fit. For this reason, we use the same ejecta mass distribution for the β-meteoroid source as the sporadic background sources with the only the value for m_{max} changing as we do not expect an impactor to produce ejecta larger than itself. To provide an estimate range, we consider the cases of $m_{max} = 10^{-14}$ kg corresponding to 1 μm ejecta and $m_{max} = 10^{-15}$ kg corresponding to 0.5 μm ejecta for the β-meteoroid contribution. Figure 3.9 plots the fitted values for $Y\Phi$ under these stipulations, indicating that β-meteoroids may have a mission averaged impact ejecta mass production of 0.75 ± 0.15 t day^{-1} for $m_{max} = 10^{-14}$ kg and 0.51 ± 0.5 t day^{-1} for $m_{max} = 10^{-15}$ kg. Note that while fitted values for the sporadic background sources use $m_{max} = 10^{-11}$ kg in Figure 3.9, values for the β-meteoroid total lunar ejecta mass flux are similar for the $m_{max} = 10^{-8}$ kg case ($\sim 3 \times 10^{-6}$ difference).

Based on a variety of spacecraft measurements, the total number flux of β-meteoroids is expected to range from $10 - 600$ km^{-2} s^{-1} [13, 122, 128, 108]. For the size range of $0.5 - 0.2$ μm with a bulk density of 2 g cm^{-3}, the expected impactor mass flux for the β-meteoroids is $\Phi_\beta = 2 - 300$ g per day. Using the mission averaged values from Figure 3.9, this corresponds to mass yields at normal incident of $Y_\beta = 2.3 \times 10^3 - 3.4 \times 10^5$ for 0.5 and 0.2 μm sized β-meteoroids respectively using $m_{max} = 10^{-14}$ kg and $Y_\beta = 1.6 \times 10^3 - 2.3 \times 10^5$ using $m_{max} = 10^{-15}$ kg. Extrapolating from experimentally measured yields to impactor speeds of 100 km s^{-1}, we expect high yields for β-meteoroids of $\gtrsim 10^3 - 10^4$ consistent with our results [109, 58]. Note that while

β-meteoroids appear as a possible solution to the HE/AH ejecta production asymmetry, it is by no means certain under this cursory comparison. Further work is necessary to narrow down what effects are contributing to the observed asymmetry.

3.5 Discussion

Expanding upon the description of a single plume from Chapter 2, we constructed a global multi-plume model and constrained the product of the the mass yield and impactor flux for the three dominant equatorial sources of the sporadic meteoroids bombarding the Moon, AP, HE, and AH (Figure 3.7). Further latitude coverage or constraints relative to these equatorial sources are necessary to introduce additional sources into the model such as northern and southern toroidal. Asymmetry between HE and AH sources persist despite considerations for spacecraft trajectory. Considering the cases of surface variation in ejecta mass yield [86] and a β-meteoroid source [109], we constrained values for the mass yield and impactor mass flux required (Figure 3.8 and 3.9). Restrictions on the required mass yield extrapolated from experiment for β-meteoroid ejecta are consistent with our results for the expected impactor mass flux with ejecta mass yields on the order of $10^3 - 10^5$. This represents a significant increase in mass yield compared with values on the order of $1 - 10$ for the sporadic background sources, which have average impactor sizes much larger than β-meteoroids. The larger inferred yields for β-meteoroids may be a combination of their higher impact speeds and the fact that for smaller impactors the surface will appear more solid and less regolith in nature. A similar mission to LADEE carrying an LDEX type dust instrument on a near-polar orbit could provide the missing observations to precisely describe the ejecta production on the lunar surface. This could be critical to gauge the loss and accumulation of volatiles in the polar permanently shadowed regions, as well as to assess the effects of interplanetary dust bombardment on the evolution of the surface regolith of other airless bodies near 1 AU.

Chapter 4

Integrated Current

4.1 Introduction

LDEX was designed to characterize the lunar dust environment. For grains with radii > 0.3 μm, LDEX recorded individual dust impacts to establish an impact rate, spatial density, and size distribution. These larger grains are produced as ejecta from the continual meteoroid bombardment of the lunar surface and follow ballistic trajectories as presented in Section 2 and 3 [50]. This data set provides the first dedicated measurement of the lunar dust environment up to altitudes as high as 250 km [49]. For the purpose of characterization of smaller lunar ejecta, LDEX also recorded an integrated current that is a collective signal generated by a large number of small particle impacts. These smaller ejecta are of particular interest as mechanisms other than meteoroid bombardment, such as electrostatic lofting, may be the dominant driver for their dynamics, particularly over the lunar terminators [12, 25, 39]. While LDEX's integrated current measurements allow for the detection of smaller dust grains, this sensitivity is not limited to dust impacts. This detection mode is also sensitive to low energy pickup ions in the lunar exosphere as well as turbulent solar wind events [49, 115, 88]. While the effect of pickup ions has already been investigated in prior publications [88], here we further expand upon the yet unexplained enhancements outside the pickup ion regime by examining telling correlations with local time, Sun-Earth-*LADEE* angle, LDEX pointing, altitude, and solar wind flux. From these trends, we find solar wind ions reflected as energetic neutral atoms (ENAs) from the lunar surface to be the most likely source of the recorded day-side enhancement. While prior searches found no evidence for electrostatically lofted grains in the altitude ranges relevant to LDEX (3-250 km)[115], a recent study suggested 5 measurements from the LDEX integrated current data set as potential detections of electrostatic lofting enhanced by solar wind charging discrepancies between the windward and leeward sides of twilight craters [126]. We expand this search by modeling a first order measure of the criteria necessary for crater lofting. Before considering any of these effects, however, it is important to understand how the integrated current is measured by LDEX.

4.2 LDEX Operation

LDEX detected dust grains via plasma generated from impacts upon a hemispherical grounded target as shown in Figure 4.1. During nominal operation, a -200 V bias is applied to an ion focusing grid in front of the microchannel plate (MCP). Consequently, ions generated from the impact are focused into the MCP while electrons are collected and measured on the target. Individual dust impacts of size > 0.3 μm are identified by comparing the coincident waveforms of the MCP and target. To measure smaller dust impacts (< 0.3 μm), LDEX also recorded the integrated signal collected by the MCP. As this integrated signal would also include additional background sources such as energetic particles, pickup ions, UV induced photo-electrons, etc. the bias voltage on the ion focusing grid was switched every 10 s to +30 V for the duration of 0.1 s. This switched mode prevents low energy ions from entering the MCP while still recording the background sources measured above. A -1600 V biased flat grid is located between the MCP and the -200 V/+30 V hemispherical grid to both focus ions into the MCP as well as prevent electrons from entering during the switched mode. By subtracting the integrated signal between these two modes, only contributions from low energy ions should remain [49]. It is this reduced integrated signal that we focus on as a potential record of lofted dust particles [12, 25, 104, 39] up to the altitudes covered by LDEX (3-250 km) that are far to small to be detected as individual impacts.

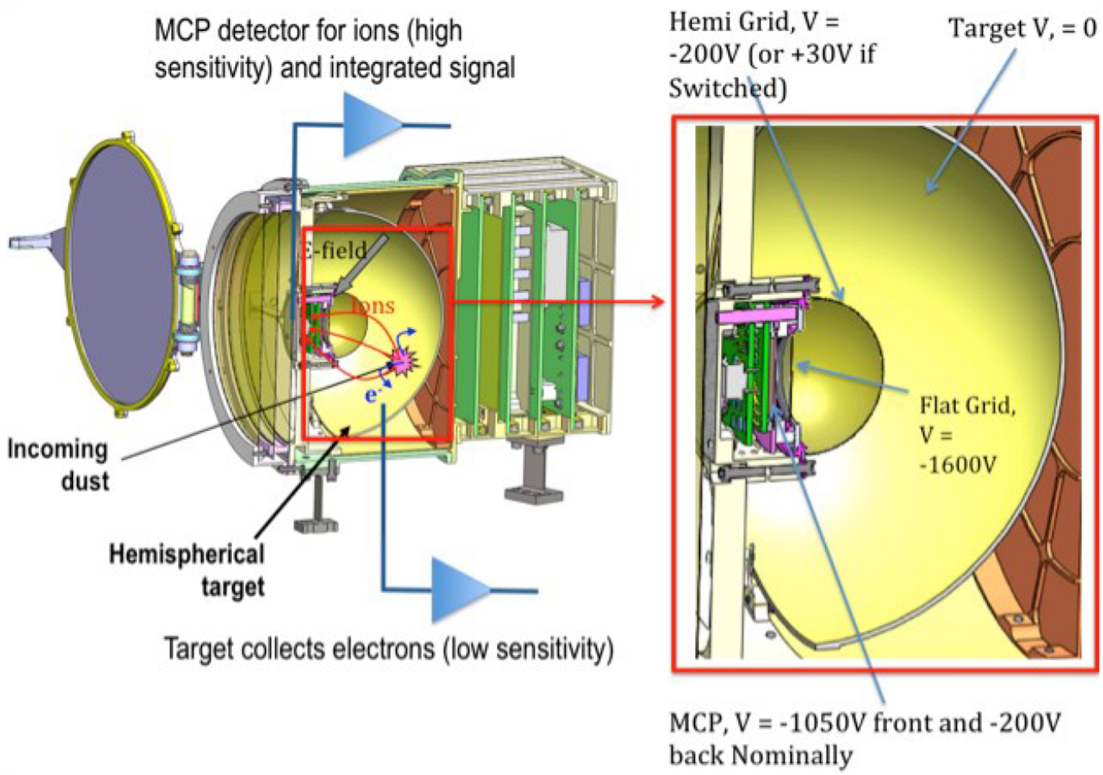

Figure 4.1: Illustration of the LDEX instrument aboard the LADEE spacecraft taken from its PDS node. Incoming dust enters the circular aperture at the front of the instrument and impacts upon the target generating plasma. The hemispherical grid is biased at -200 V during nominal operation while the target is biased at 0 V to focus low energy ions into the MCP detector and electrons on the target. Every 10 s, the biased voltage on the hemispherical grid is switch to +30 V for 0.1 s to detect background noise. An additional flat grid biased at -1600 V is located between the hemispherical grid and the MCP to enhance ion detection while also prevention electrons from entering during the +30 V mode [15].

4.3 Data

4.3.1 Overview

Before considering trends in the integrated signal, we need to filter out another source of background identified as ‘pickup ions’. These pickup ions are ambient low energy ions scooped up by LDEX in its trajectory through the extended lunar exosphere. Even for periods where LDEX is pointed anti-ram of the spacecraft (or ‘backward’ pointing), the electric field produced by the solar wind flow can force low energy ions into the detector. To remove contributions from pickup ions, we select for periods where the ambient electric field is not pointing into LDEX’s field of view (FOV). To determine the ambient electric field’s pointing with respect to LDEX’s boresight, we use data from the Acceleration, Reconnection, Turbulence and Electrodynamics of the Moon’s Interaction with the Sun (*ARTEMIS*) mission which covered the dynamic plasma environment throughout the entirety of LDEX’s operation [49, 115, 88]. All measurements considered in this work are only for periods when the electric field to boresight angle is $> 110°$.

To narrow down the dominant contribution to LDEX’s integrated signal (that aren’t pickup ions), we consider all integrated current measurements excluding periods where the ambient electric field is pointing into LDEX’s FOV. Figure 4.2 plots the average integrated current vs local time (LT) and Sun-Earth-LADEE angle (SEL angle) for forward (*left*) and backward (*right*) pointing periods. Note that 0 and negative integrated current measurements are excluded from the average and are instead shown in Figure 4.4. ‘Positive’ integrate current measurements are those where the -200 V switched mode measures more than the +30 V mode. ‘Negative’ integrated current measurements are the opposite.

Individual negative integrated current signals are excluded from the averaging of each bin as such measurements are attributed to transient high energy ion enhancements that only survive long enough to be measured by the +30 V switched mode. Note that low energy negative ions would not be measured in the +30 V switched mode due to the -1600 V focusing grid and so cannot account for these negative reduced integrated current measurements. Instead, we will consider

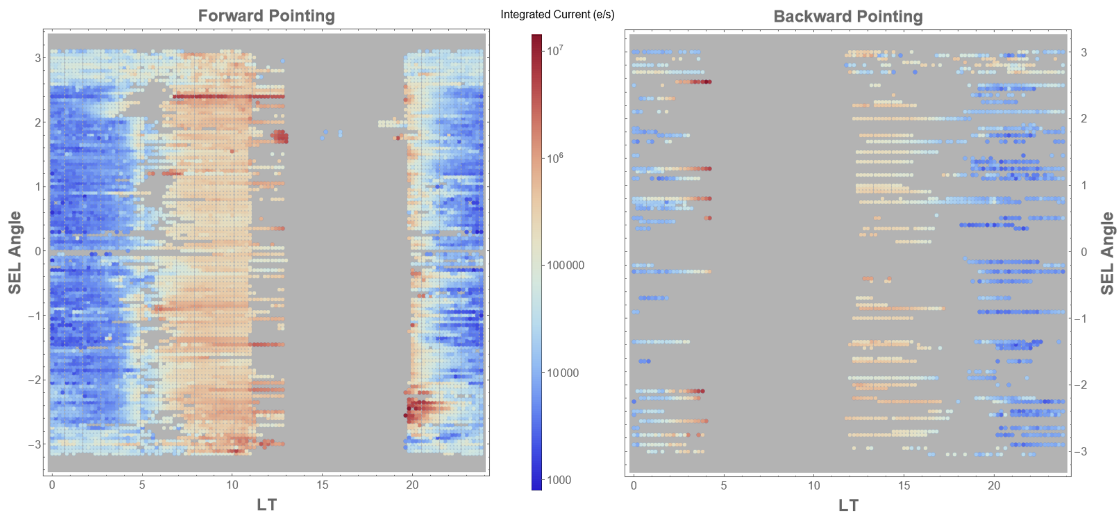

Figure 4.2: Mean values of the positive integrated current measurements binned by local time (LT) and Sun-Earth-*LADEE* angle (SEL angle) for both forward and backward pointing periods, while excluding the contribution of pickup ions. A SEL angle of 0 corresponds to *LADEE* positioned between the Sun and the Earth while a positive angle is in the direction of the Earth's orbital velocity. In forward pointing, there is a consistent enhancement on the lunar day-side (6-18 LT) for all SEL, and another significant enhancement from 19-22 LT for SEL angles when *LADEE* is between the Earth's magnetic bow shock and magnetotail opposite the Earth's orbital velocity. The missing data, 12 - 18 LT for forward and 4 - 12 LT for backward pointing periods, are periods for which the Sun would be in LDEX's FOV [15].

such negative integrated signals as a means of identifying regions of high turbulence in the plasma environment. A Sun-Earth-*LADEE* (SEL) angle of 0° corresponds to *LADEE* positioned between the Earth and Sun while a positive SEL angle corresponds to the direction of the Earth's orbital velocity. From Figure 4.2, we note three distinct regions of enhancement. The first and most prominent is the consistent enhancement on the lunar day-side (identified as the red box in Figure 4.5), clearly demonstrated by the normalized histograms of Figure 4.3. Second is the significant enhancement on the night side (19-22 LT) for SEL angles corresponding to when LADEE is in the Earth's magnetosheath opposite the Earth's orbital velocity (identified as the blue box in Figure 4.5). Finally, there appears the be a slight band of enhancement for all LT corresponding to when LADEE is within the Earth's magnetotail. We will focus on the first two patterns for this study, particularly the altitude and pointing dependencies of each region (shown in Figure 4.6 and 4.7). Note that the relatively large current measurements at the edges of the data coverage (20 LT for forward pointing and 4 LT for backward pointing) consist of fewer than 3 measurements and are for times when the Sun just enters LDEX's FOV. First, we consider the night-side enhancement within the Earth's magnetosheath.

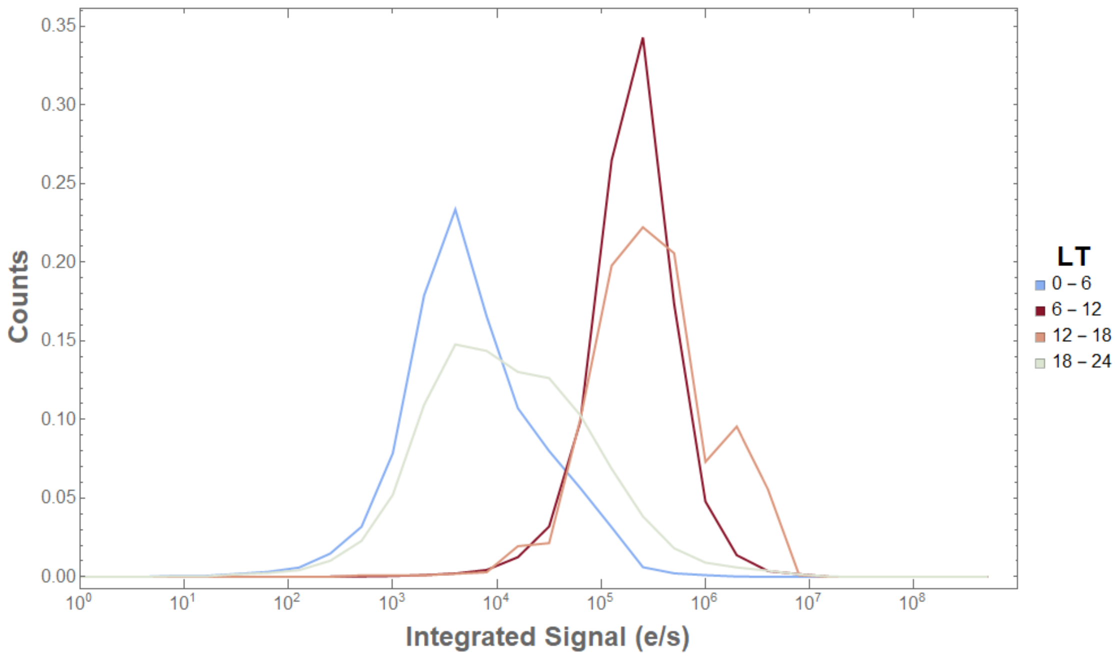

Figure 4.3: Normalized histograms for different LT bins taken from all measurements in the forward pointing regime of Figure 4.2. Note the consistent enhancement for the lunar day-side compared to the night-side.

4.3.2 Night-side Enhancement

Large negative subtracted integrated signals are indicative of transient enhancements. Shown in Figure 4.4, those observed by LDEX are concentrated around 19-22 LT and between Earth's bow shock and magnetotail correlated with one of the enhancements noted in Figure 4.2. Additionally, enhancements on the night-side, and more specifically in the 18-24 LT range, appear only in the forward pointing regime. Consider also the probability distribution function of integrated signal vs solar wind to LDEX bore sight angle generated from Artemis measurements of the solar wind shown in Figure 4.5 (*bottom right*). The region bounded by the red dotted line indicates LDEX's

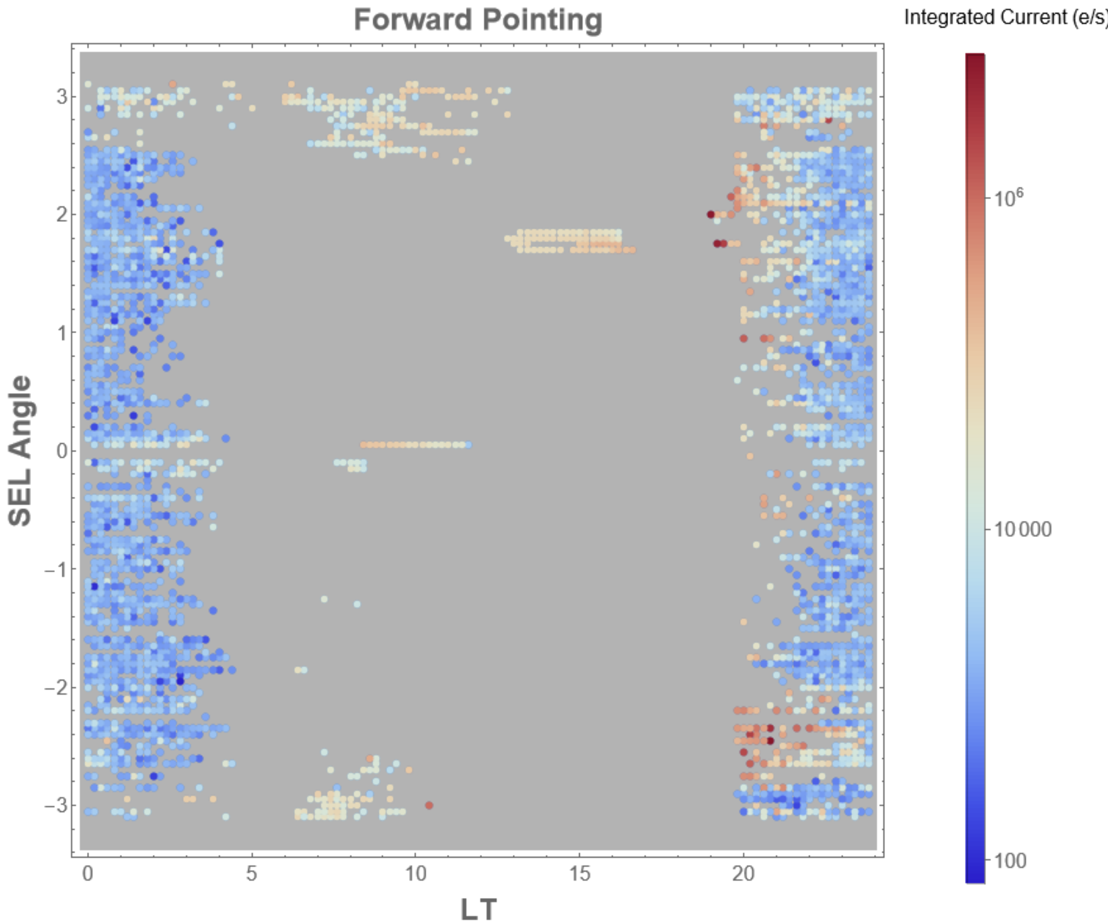

Figure 4.4: Average values for all negative integrated current measurements binned by local time (LT) and Sun-Earth-LADEE angle (SEL Angle) for the forward pointed regime excluding pickup ions. Negative integrated currents are indicative of transient enhancements in the measured current that happened to be measured during the +30 V switched mode and not the -200 V one. We would expect regions of larger and more numerous negative integrated currents to also contain transient signals enhancing the -200 V mode thus contributing to the positive measurements shown in Figure 4.2 [15].

field of view which is maximal at 0° decreasing to 0 at 68°. Almost all significant integrated current measurements ($> 10^5$ e s^{-1}) correspond to a solar wind bulk flow velocity pointing into LDEX's FOV. The correlation with solar wind visibility combined with significant negative integrated current measurements indicates that this enhancement is the result of transient high temperature plasma produced in the interaction between the solar wind and Earth's bow shock. The day-side enhancement, however, follows a very different trend.

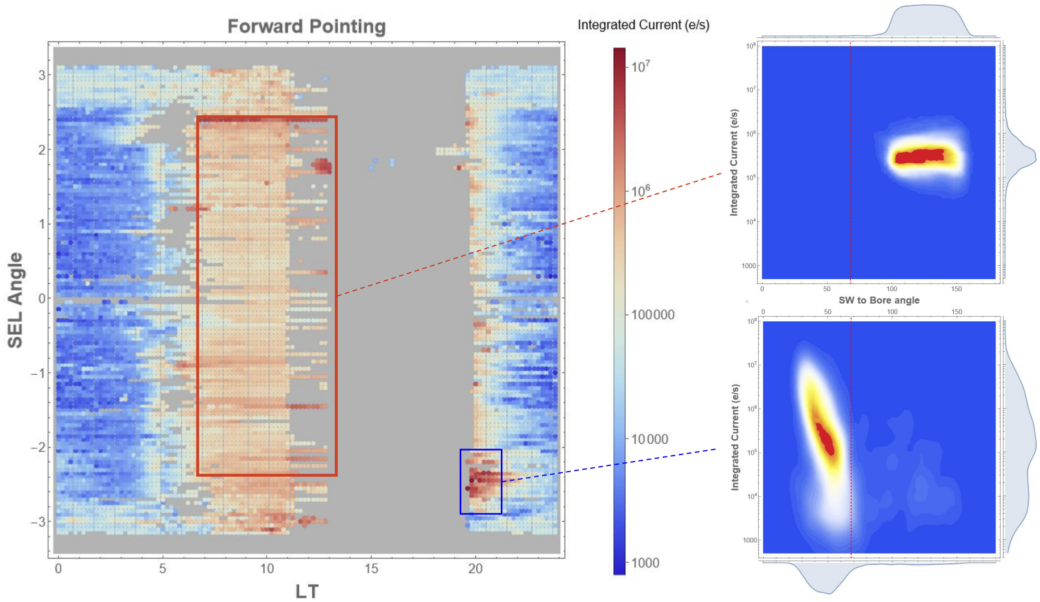

Figure 4.5: Contour plots (*right*) of the distribution of integrated current measurements as a function of integrated current value and solar wind to LDEX boresight angle for the two enhancement regions indicated by the red and blue boxes (*left*) over Figure 4.2. LDEX's FOV spans from an angle of 0° up to 68° indicated by the vertical dotted line. Note that for the night-side enhancement solar wind ions are flowing directly into the instrument while for the day-side enhancement the solar wind is not visible to LDEX [15].

4.3.3 Dayside Enhancement

As indicated by Figure 4.5 (*top right*), all measurements on the day-side enhancement (outside of the magnetosheath) occur when the solar wind is not visible to LDEX directly. Additionally, Figure 4.6 contains a consistent enhancement in the integrated signal for 6-18 LT in both forward and backward pointings as well as no apparent altitude dependence. The majority of lofted material and meteoroid ejecta should have tangential speeds to the lunar surface less than the spacecraft's speed and thus should only contribute to the forward pointing regime and so cannot alone account for this day-side enhancement. Note that as this current is an integrated measurement, signal magnitudes are a function of ejecta density as well as ejecta mass and velocity at the point of detection. Figure 4.7 further emphasises the lack of pointing dependence (though there is a slight one covered in Section 4.5) as day-side forward and backward pointing enhancements are nearly identical and

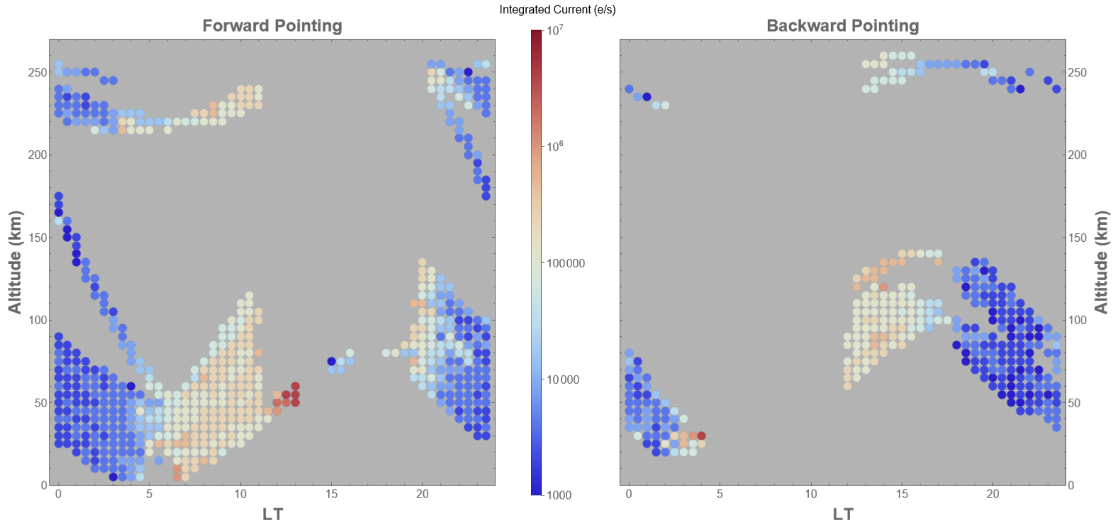

Figure 4.6: Average values for all positive integrated current measurements binned by altitude and local time (LT) for both the forward and backward pointed regimes relative to the spacecrafts velocity outside of the Earth's magnetosheath. The lunar day-side (6-18 LT) enhancement appears to show no altitude dependence. Note that the larger signals at the boundary of where the data coverage ends are suspect as the Sun just enters LDEX's FOV during those times [15].

consistent across the entire range of 6-18 LT. Thus the lack of altitude and pointing dependence in Figure 4.6 for the day-side enhancement suggest that the majority of these enhancements are not from lofted nor meteoroid ejected dust. Note again that these trends do not rule out lofted dust grains or ejecta as contributions, only that they are not the most significant factor. This enhancement, however, is not entirely independent of solar wind.

4.4 Reflected Energetic Neutral Atoms

Thus far the day-side enhancement has been demonstrated to have the following characteristics:

(1) No correlation with solar wind flowing directly into LDEX (Figure 4.5).

(2) No correlation with negative integrated current measurements (Figure 4.4)

(3) Minimal pointing dependence (Figure 4.6 and 4.7).

(4) Consistent across the entire 6-18 LT range (Figure 4.7).

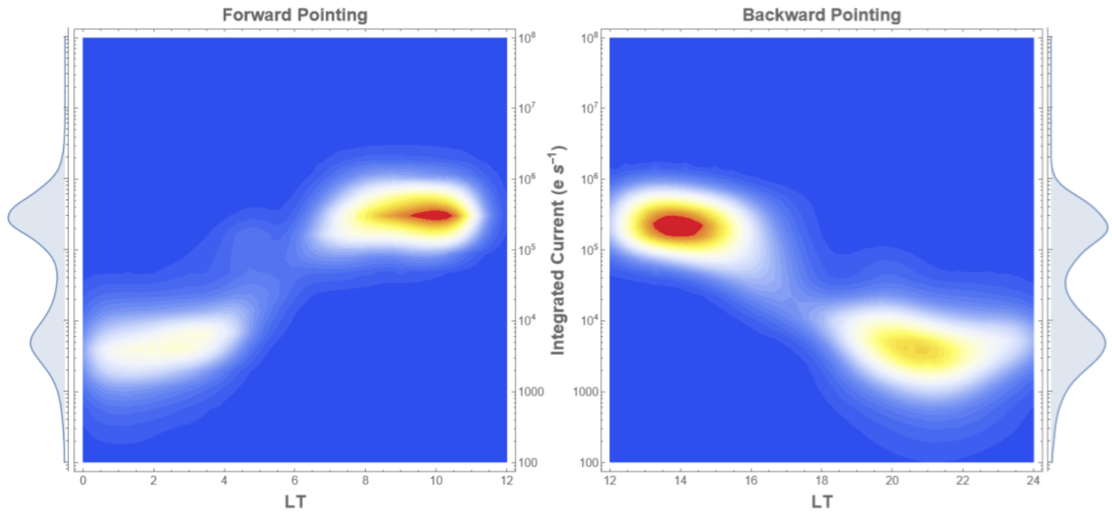

Figure 4.7: Contour plots of the distribution of integrated current measurements as a function of integrated current value and local time for forward (*left*) and backward (*right*) pointing regimes. The day-side enhancement remains consistent across all relevant local times regardless of pointing. Note that the colored contours are a measure of data coverage for each bin and are of less importance than the projected histograms on the left and right boundaries for the integrated current [15].

(5) No altitude dependence (Figure 4.6).

Note that the plotted data already accounts for pickup ions and is a reduced measurement (i.e. enhancements must appear in the -200 V switched mode but not the corresponding +30 V mode). The first two points rule out high temperature or turbulent plasma flowing directly into the instrument as was the case for the night-side enhancement. The third characteristic suggests that these are not small lofted or meteoroid ejected dust grains as ejecta have an average initial velocity of 670 m s^{-1} (less than LADEE's orbital velocity of 1.67 km s^{-1})[17, 50, 117] and lofted material has only been shown to reach heights of 10's of cm with a possible exception discussed in Section [121]. Additionally for the case of ejecta, we would expect some correlation with dominant source radiants such as helion, anti-helion, and apex sources at local times of 10.3, 1.7, and 6 LT respectively [112, 14]. Item four shows that this is not the case, however, and instead remains consistent in integrated current magnitude across the entire day-side.

The most likely source that fits the observed correlations would be from reflected energetic neutrals (ENAs) originating as solar wind protons neutralized and back-scattered from the lunar

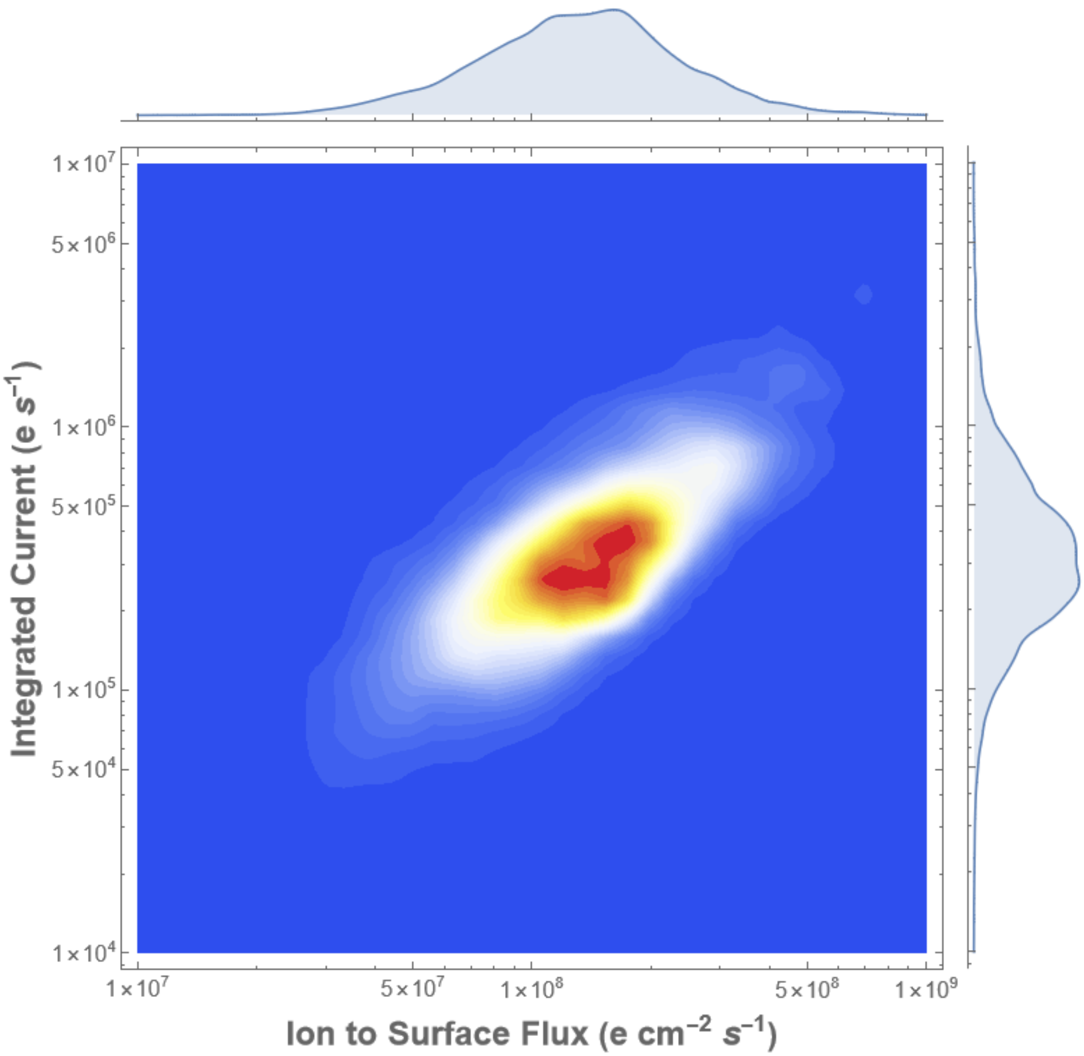

Figure 4.8: Contour plots of the distribution of integrated current measurements as a function of integrated current value and solar wind ion to lunar surface flux for for all data points within the red box of Figure 4.5. Ion to surface flux values were interpolated from *ARTEMIS* measurements with total ion flux modified by Cos of the solar wind bulk velocity angle with respect to surface normal directly below the detection point. Integrated current values show a strong linear correlation with solar wind ion to surface flux suggesting that these enhancements are due to backscattered ENAs [15].

surface [36, 124] as the observed ENA energy spectrum covers temperatures as high as 600 eV following ballistic trajectories with speeds greater than the lunar escape velocity [36, 123, 34]. For the relevant day-side enhancement measurements, the average solar wind energy is 760 eV. Using

Figure 12 of [34], the average reflected energy is expected to be $\sim$ 35 eV or 82 km s^{-1} in the case of H, far greater than the spacecraft's 1.67 km s^{-1}. The reflected component is necessary to produce a velocity component tangential to the lunar surface as without this component ENA's would only show up when the solar wind is within LDEX's FOV instead of both pointings, which is not the case as shown in Figure 4.5. ENAs are observed to reflect from the lunar surface at a broad range of reflection angles almost isotropic near 12 LT and favoring scattering back toward the Sun with increasing solar wind to surface normal angle [93]. The best indicator that the day-side enhancement is due to reflected ENAs is shown in Figure 4.8 where a strong linear correlation is depicted in the observed probability distribution between the LDEX integrated current and solar wind ion to surface flux derived from *Artemis* data. It should be noted that for ENAs to contribute to LDEX's integrated current signal, these neutrals must either re-ionize within the instrument at sufficiently low energies to be blocked by the +30 V switched mode or sputter low energy rhodium ions upon impact with the hemispherical target. For the case of sputtering from a rhodium target, there are some estimates we can look to. Using the energy dependence of sputtering yields for mono-atomic targets at normal incident given by [29] fitted for hydrogen isotopies impacting a rhodium target in [30], the threshold energy for rhodium ion sputtering is 174 eV. As the anticipated average energy per solar wind ion impacting the lunar surface carried by ENAs ranges from 30 eV to 45 eV [34], sputtering of rhodium ions from LDEX's grounded target is unlikely.

To determine if ENAs are a feasible source for this integrated current signal, we consider the *Chandrayaan-1* measurements of backscattered ENAs from the lunar surface. Figure 4.8 indicates an average ion to surface flux from the solar wind of 1.6×10^8 e cm^{-2} s^{-1} for the relevant measurements. As the median of backscatter fraction for *Chandrayaan-1* ENAs is 0.19 [35] and LDEX's maximal effective area is $\sim$100 cm^2, we anticipate an integrated current enhancement of 3×10^9 e s^{-1} at 100% collection efficiency (i.e. every ENA entering LDEX is re-ionized). Figure 4.7 shows an average integrated current signal of 4×10^5 e s^{-1} and 8.6×10^3 e s^{-1} for the forward pointing day and night-side respectively. Taking the night-side as a measure of the background noise, the enhancement potentially due to backscattered ENAs is 3.9×10^5 e s^{-1}. Therefore, LDEX, need only have a collection efficiency of 0.01% to detect solar wind backscattered ENAs from the lunar surface.

Note that such a low collection efficiency is to be expected due to a variety of factors. Geometric factors such as LDEX's pointing (which is close to tangent from surface normal for all relevant detections) as well as reflection angle dependence should play a significant role in the collection efficiency. The majority of backscattered ENAs are expected to reflected back at the Sun even with increasing incident angle so there should be at least some with the requisite horizontal speed for LDEX detection [93]. Comparisons with LDEX pointing directly at the lunar surface would provide a means of validating the scattering angle dependence of the ENA contribution. However, we do not have the requisite surface pointed data coverage to make such a comparison. Additionally, this detectability estimate does not consider re-ionization/sputtering rate of ENAs as they impact LDEX's hemispherical target. Further calibrations would be necessary to constrain this effect as well as potential secondary contributions as LDEX was not originally designed to measure ENAs. Finally, the backscatter fraction is highly dependent upon solar wind speed [34]. Comparing the derived reflection fraction from *Chandrayaan-1* to IBEX observations shows the that 0.19 values used early is in reasonably agreement for lower energy incident solar wind (at 0.45 and 0.71 keV energy passbands), but under-predicts for higher energies (1.11 keV and above) [34]. With an average solar wind energy of 760 eV for the relevant periods, a reflection fraction of 0.19 is reasonable for the majority of detections and at worst serves as a conservative estimate for the higher energy periods. An accurate estimate of backscattered ENA detections by LDEX would require a comprehensive model incorporating all of these factors. The above estimate, however, serves to demonstrate that ENAs as an explanation for the majority of the day-side integrated current enhancement is more than feasible.

Note that the neutral component of this population is not required for contributing to the observed enhancement. The source is a potential candidate as long as it is altitude independent up to ~ 150 km (likely from high surface normal speeds), pointing independent (i.e. high enough surface tangential speeds to overcome the spacecrafts speed of 1.67 km s^{-1}), and high enough energy

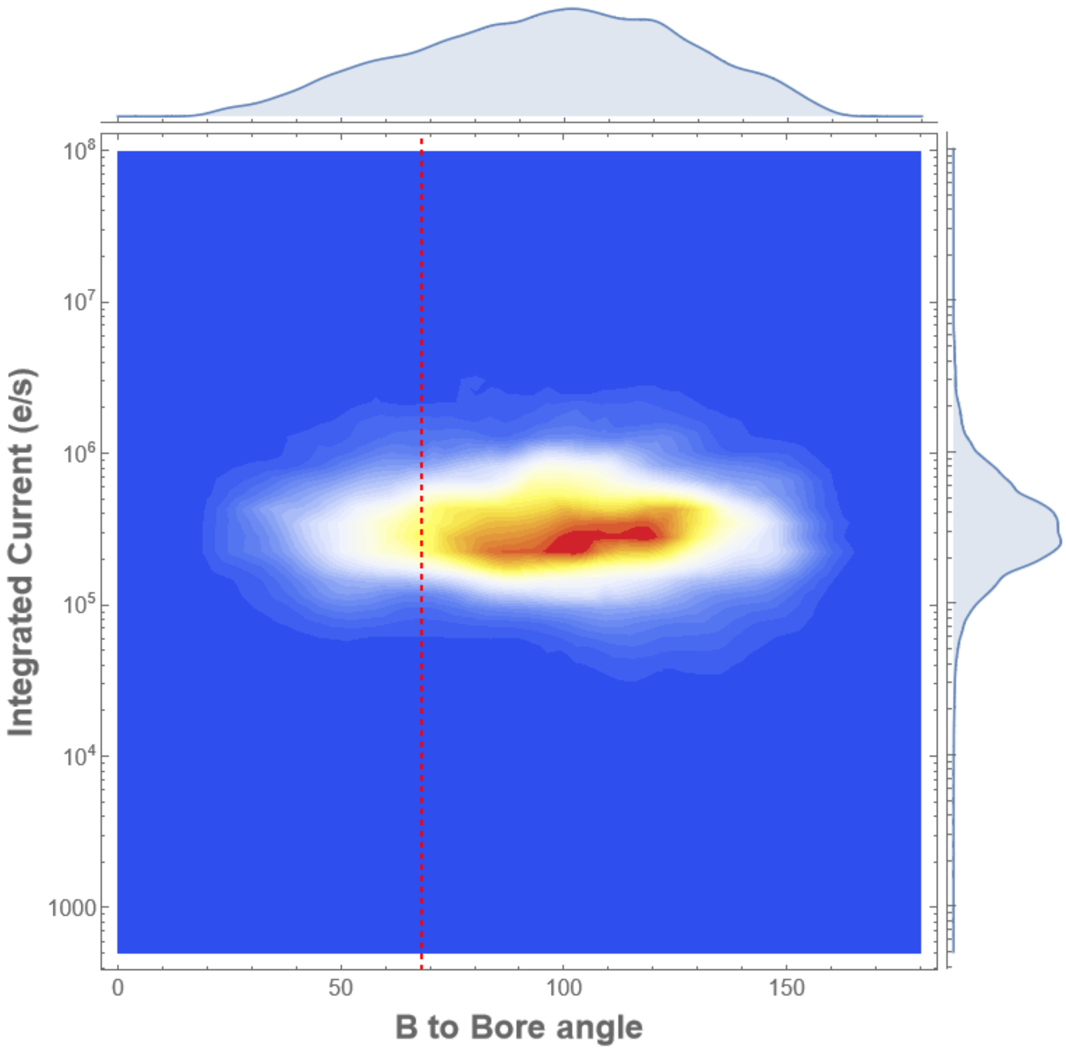

Figure 4.9: Contour plots of the distribution of integrated current measurements as a function of integrated current value and solar wind magnetic field vector to LDEX boresight angle for for all data points within the red box of Figure 4.5. LDEX's FOV spans from an angle of 0° up to 68° indicated by the vertical dotted line. In the case of backscattered solar wind ions enhancement, we expect an increase in integrated current corresponding to the solar wind magnetic field entering LDEX's FOV as these ions should be trapped to solar wind magnetic field lines. We observe no such trend nor corresponding negative integrated current (see Figure 4.4) indicating a lack of high energy ion enhancement [15].

or neutral to overcome the solar wind ambient electric field pointing out of LDEX's FOV. In the case of high energy incident positive ions, sufficient energy would need to be lost upon impact with the target (or sputtered low energy positive ions) such at the corresponding signal would only be measured by the MCP during the -200 V switched mode and not the +30 V. Else the enhancement would also show as a negative enhancement in Figure 4.4. In the case of solar wind backscattering from the lunar surface, some ions are not neutralized during the reflection and a portion that have may be re-ionized by photoionization or charge exchange. These backscattered ions become pickup ions in the solar wind and gyrate about its magnetic field lines [34]. While we have already inferred from the lack of negative enhancement on the lunar day-side that high energy ion detections are unlikely for this filtered data set, considering the solar wind's magnetic field orientation to LDEX's boresight provides another avenue for ruling out potential high energy ion enhancements. Figure 4.9 plots the distribution of integrated current measurements as a function of solar wind $\vec{B}$ angle to LDEX's boresight as measured by *ARTEMIS* for all data points within the red box of Figure 4.5. LDEX's maximum field of view angle is again indicated by the vertical dotted line. While some detections do fall within LDEX's FOV, we note no apparent trend between integrated current and solar wind $\vec{B}$ to LDEX's boresight angle like the one depicted in Figure 4.8.

4.5 Integrated Dust Measurement

With the various background contribution cases covered in the previous sections, we can take an initial look at the potential ejecta or lofted grain contribution to the integrated current. While the day-side distributions in Figure 4.7 are similar enough between forward and backward pointing regimes to argue that the majority of the signal cannot come from impact ejecta or lofted dust grains, there is a slight difference between the two. Taking the difference between the two pointing regimes provides an estimate for the pointing dependent integrated current contributions, namely ejecta and lofted dust grains. The question then becomes what would be the required detection rate by LDEX to account for the full difference between forward and backward pointing regimes?

LDEX was calibrated at the Institute of Modeling Plasma, Atmospheres, and Cosmic Dust (IMPACT) dust accelerator at the University of Colorado. Using submicron olivine particles over a mass range of 5×10^{-18} - 6×10^{-14} kg and speed range of 0.9 - 39 km/s, the ion impact charge produced from impacting the target was calibrated to the following,

$$q_i\ [e] = (0.103 \pm 0.001) \times m\ [\mathrm{kg}] \times \mathrm{v}\ [\mathrm{km/s}]^{4.76\pm0.15}, \tag{4.1}$$

where m and v are the mass and impact speed of the dust particle respectively. Dividing the forward-backward reduced mean integrated current measurement by the charge from Equation 4.1 gives an estimate of the small (< 0.3 μm) dust detection rate where we use a nominal size of 0.1 μm (or 8.4×10^{-18} kg for a density of 2 g/cc) and an impact speed equal to the spacecraft's speed.

For the day-side, we look for the potential for electrostaticly lofted dust grains. As the backward pointing only covers from 12 - 18 LT and similarly the forward pointing only covers 6-12 LT, the chosen forward pointing LT bin is reduced by the corresponding backward pointing LT bin mirrored about the average solar wind source radiant (near 12 LT) outside of the Earth's magnetosheath ($-2 \leq$ SEL angle ≤ 2). This is done with the goal of comparing between regions of similar solar wind (incident and reflected) environments available to our limited coverage. In addition, values are restricted to altitudes ≤ 100 km as the focus of this comparison is on ejecta and lofted material and measurements corresponding to $\pm10^7$ e cm^{-2} s^{-1} around the mean solar wind ion flux for similar solar wind environment. The current difference oscillates between $\pm10^4$ e s^{-1} depending upon LT bin suggesting negligible contribution from dust grains on the lunar day-side. It should be noted that the day-side comparison is marred by the velocity dependence of ENA current contributions as well as solar wind velocity dependence on ENA production. While the average ENA speed (82 km s^{-1}) is quite large compared to the spacecraft speed (1.67 km s^{-1}), the mechanism of re-ionization within LDEX and thus the velocity dependence of detection is unconstrained and could account for a non-negligible portion of the forward-backward pointing difference. Further study is required to constrain this effect.

The night-side comparison is more straightforward to make as there should be no ENA contribution and a quieter plasma environment. Figure 4.10 plots the forward pointing integrated current mean binned in LT reduced by the backward pointing integrated current mean for values between 21 and 23 LT. A singular region of backward pointing was chosen to reduce every forward

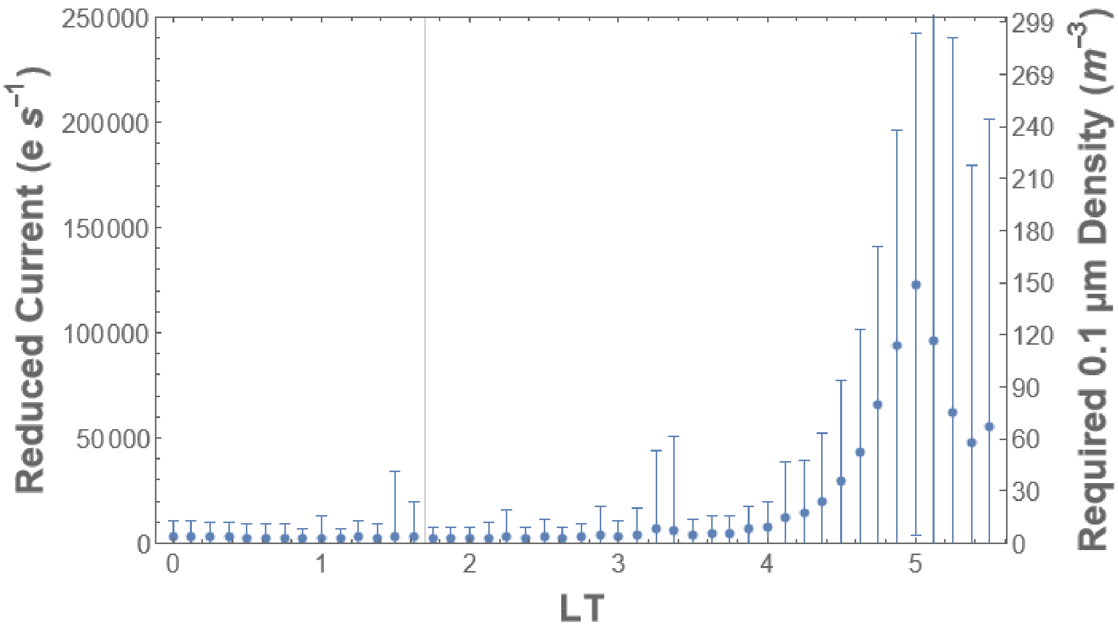

Figure 4.10: Average integrated current measurements binned in LT for the forward pointed regime reduced by the average backward pointed values between 21 and 23 LT outside of the Earth's magnetosheath. No apparent enhancement is observed near the antihelion sporadic source radiant at 1.7 LT (indicated by the vertical grey line) suggesting a vanishingly small impact ejecta population < 0.3 μm in size. The enhancement at 5 LT is likely due to changes in spacecraft charging as LADEE enters the lunar optical shadow. Corresponding values for the required 0.1 μm detection rate, derived from Equation 4.1 and converted to density, to account for the entire integrated current difference are indicated on the right axis. Note that these values are the estimated density assuming that the entire enhancement is due to 0.1 μm dust detections [15].

pointing LT bin as backward pointing LT bins approaching 6 LT include enhancements for the solar wind entering directly into LDEX's FOV as shown in Figure 4.2. While this kind of reduction would be problematic for the day-side due to varying solar wind environment and ENA reflection geometry, neither effect is relevant for the night-side. First feature of note is that there is no noticeable enhancement along the antihelion sporadic background radiant at 1.7 LT indicated by the grey line [14, 111, 116]. This suggests that the population of ejecta < 0.3 μm produced by antihelion impactors (and presumably similar for the helion side) is vanishingly small. The second feature of note is the significant increase approaching 5 LT. This is of particular interest for electrostaticly lofted dust as numerous prior in situ [91, 39, 96, 11] and remote sensing observations [72, 37, 32] have indicated the lunar terminators as potential areas of significant lofted material.

The largest spike near 5 LT is, however, likely do to LADEE entering the lunar optical shadow and thus suddenly changing the spacecraft charging. This would cause a change in the local spacecraft sheath and thus allow for pickup ions to enter LDEX [115]. The contribution from this effect, however, is difficult to estimate and so we report the 0.1 μm detection rate, converted to density, required to account for the total difference in each bin for comparison to other estimates. Note that this estimate does not account for the potential ionization enhancement resulting from the lofted grain's charge. For impact speeds on the order of a few km s^{-1}, field emission of electrons from a metal target can occur as the charged particle approaches. This electron emission results in desorption and ionization of molecules from the target surface in excess of similar neutral impactors [106, 19]. For impact speeds less than 2 km s^{-1}, however, the effect is negligible and should therefore have little effect on LDEX's integrated current measurements [19]. It should also be noted that this ionization enhancement cannot explain the increased average integrated current on the day-side observed in Figure 4.2 and 4.7 as the arguments outlined in Section 4.4 preclude small ejecta or lofted material as sources. For comparison, individual dust detections for ejecta ≥ 0.3 μm occur at an average rate of 1 min^{-1} [115]. However, the estimated density of 0.1 μm dust grains is surprisingly close to the $\sim$100 m^{-3} at a 50 km altitude derived from modeling the excess brightness observed by *Apollo 15* and *17* at the lunar terminator [72]. This enhancement is peaked at 5 LT as opposed to the anticipated 6 LT suggesting spacecraft charging as the most likely explanation for this particular feature. Additionally, follow up studies could not verify this high-density population of small grains [115]. To probe the potential lofted dust environment near the lunar terminators, we shall consider the correlation between integrated current enhancement and twilight craters.

4.6 Lofting of Lunar Dust Near Twilight Craters

One potential contribution to the LDEX integrated signal is that of small grains (< 0.3 μm) lofted from the surface via electrostatic repulsion. As lofting due to particle-particle electrostatic repulsion from patch charging models [121] are expected to reach heights on the order of 10's of cm, reaching the altitudes observed by LDEX (3-250 km) requires an additional repulsive force from

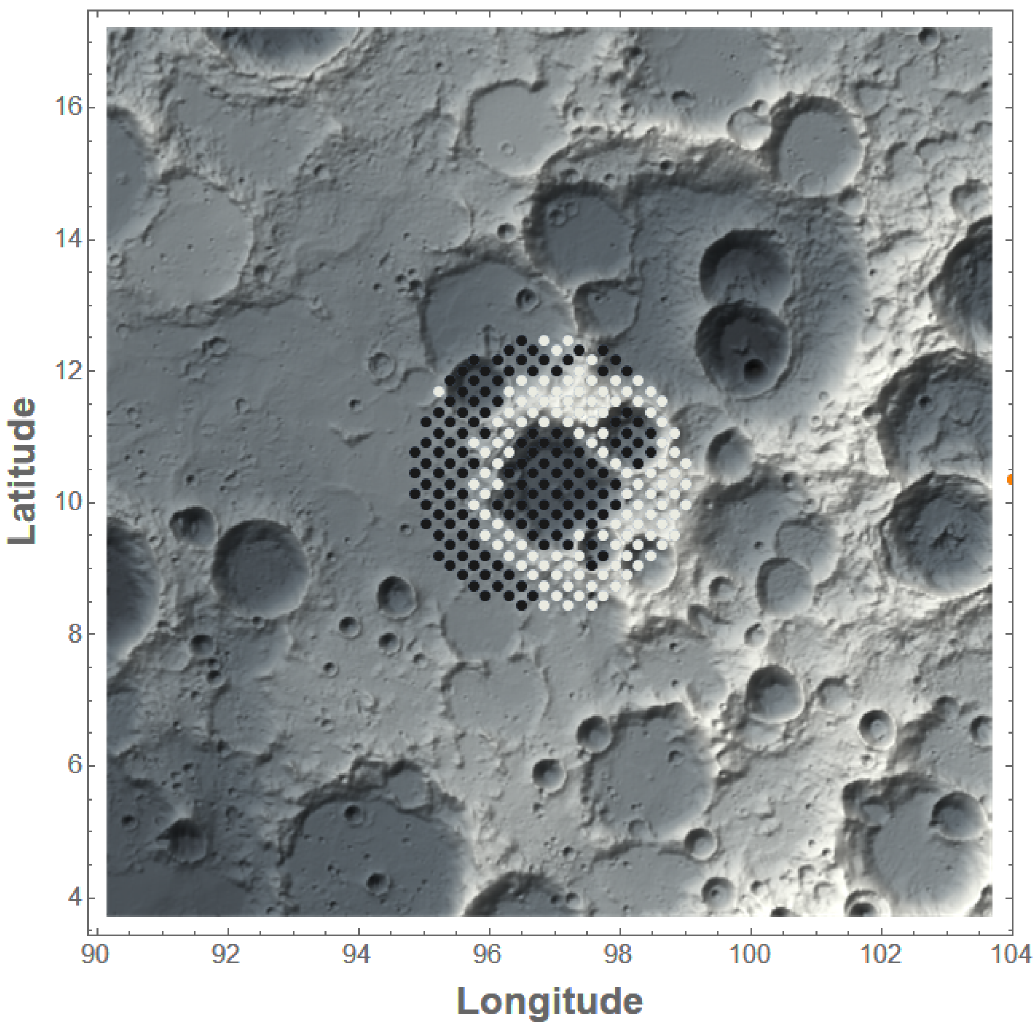

Figure 4.11: Identified lit vs unlit grid points for a detection near the sunrise terminator over an effective surface range of 400 km. Solar wind access is determined by taking the elevation data along the geodesic toward the Sun's current position at time of detection shifted by $\sim 4^{\circ}$ in the minus LT direction to account for the earth's velocity effect on the solar wind's relative trajectory. This data is then compared to a projected ray from the Sun to determine if the solar winds path is blocked by any changes in topography. White dots indicate lit or solar wind impact points while black dots indicate grid position where the solar wind is blocked by some elevation along its trajectory. The orange dot on the right border of the plot indicates the direction of the shifted sun [15].

the surface. One such enhancement may come from large topographical features, such as craters, for times when the topographic elevation angle is larger than that of the solar wind deflection angle [31]. In such cases, the solar wind wake around the feature produces a strong negative potential on

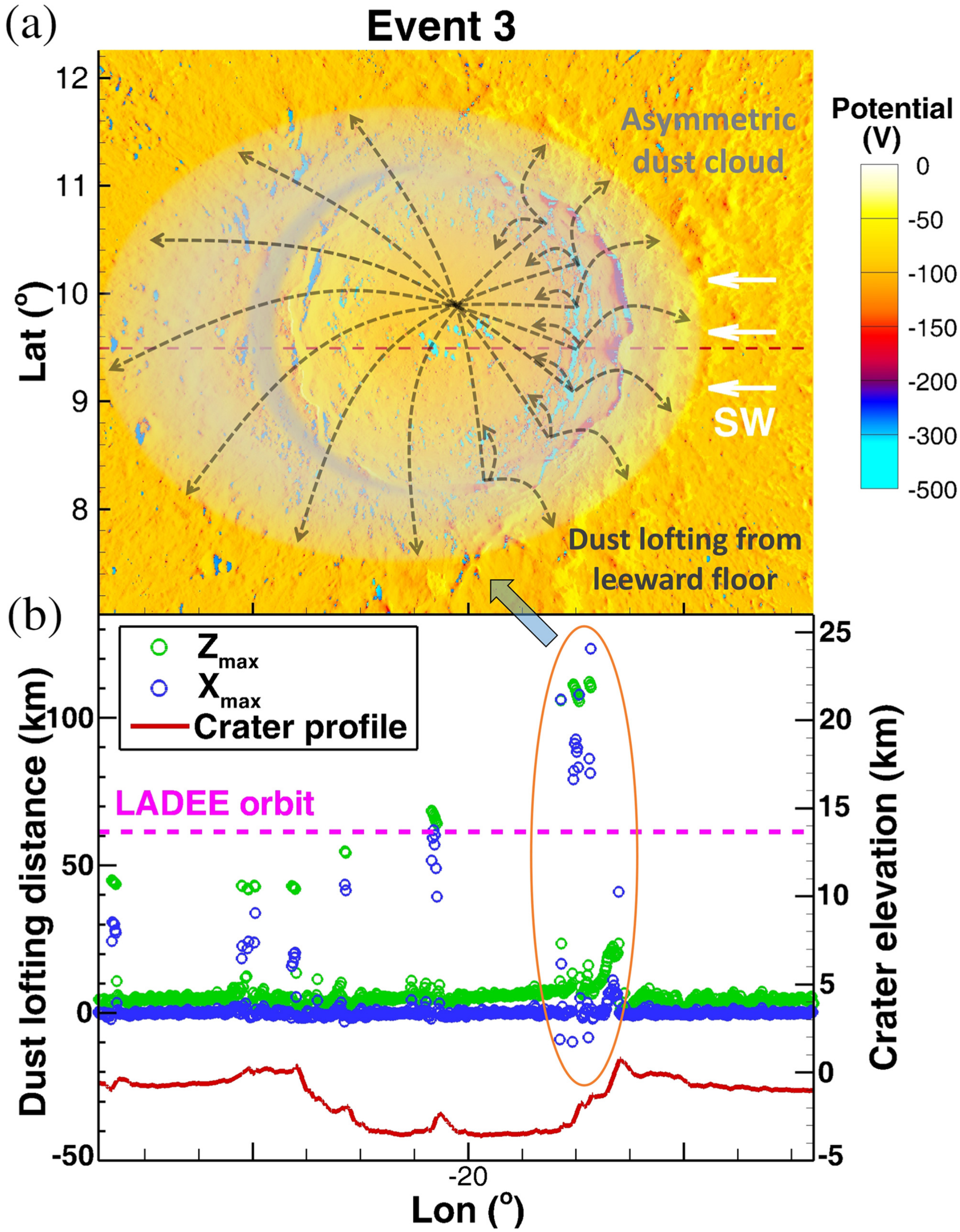

Figure 4.12: Illustration of the windward vs leeward charging of a crater near the lunar terminator taken from [126]. Panel (b) indicates the modelled dust lofting distances for 0.1 μm sized dust grains under this twilight crater enhancement compared to the trajectory of *LADEE* for one of the five events identified by [126] to be due to electrostatic lofting via twilight craters.

the leeward side which may enhance the electrostatic lofting of positively charged grains produced on the windward side as depicted in Figure 4.12. As this phenomenon requires the solar wind to charge one side of a topographical feature but not the other, craters near the solar terminators are prime candidates for enhanced electrostatic lofting. There are 5 enhancements within LDEX's integrated current data set are identified by [126] as possible detections of such an effect due to their proximity to twilight craters. While backscattered solar wind ENAs serve as better candidates for the majority of the day-side enhancement as discussed in the prior sections, we should consider the potential for lofted dust near the terminators where ENA backscattering is minimal (for LDEX's FOV) and the proposed crater lofting is maximal.

To identify whether this mechanism has a significant impact upon the integrated signal, we consider all measurements between 5 and 7 LT not associated with pickup ions. For each measurement, elevation data of the lunar surface was selected for within an effective range using the LRO LOLA DEM. As the lofted trajectories are modeled to travel as far as 100's of km [126], we chose an effective radius of 400 km for the surface patch. For each elevation grid point within the patch, additional interpolated elevation data was considered along the geodesic that included the solar winds incident vector taken as the Sun's position in lunar latitude and longitude at the time of measurement shifted by $\sim 4^\circ$ in the minus LT direction to account for the Earth's orbital velocity. Comparing this to the elevation of a ray of solar wind from the sun to the corresponding surface grid point gives a test of whether the solar winds path is interrupted by any change in topography. Doing this for each elevation data point within the effective range generates a collection of "lit" vs "unlit" points. Note that "lit" vs "unlit" refers to whether the solar wind is blocked in its trajectory to that particular surface element and not in reference to solar photons. Figure 4.11 is an example of one such grid with the direction of the Sun identified by an orange dot on the right boundary. Considering the number of lit grid points minus the number of unlit grid points points normalized by the total number of points provides a crude measure of the conditions required to generate a large negative surface potential via solar wind wake effects around topological features.

In the case of crater enhanced electrostatic lofted dust, we would expect the mean integrated

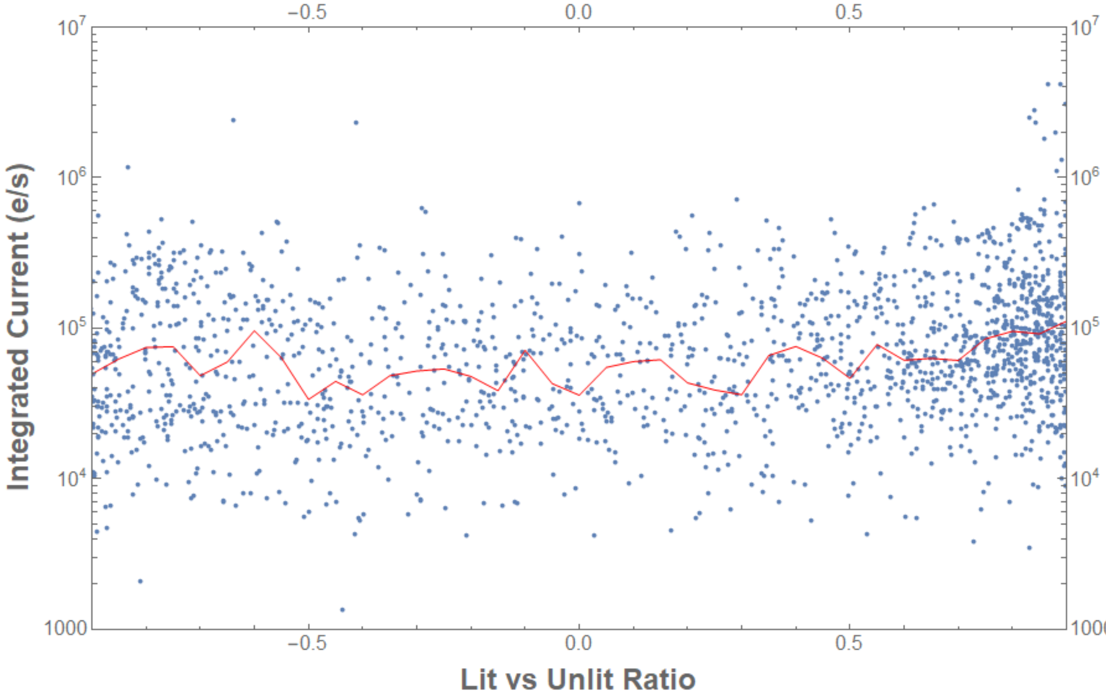

Figure 4.13: Values of the integrated current signal for all values between 5 and 7 LT excluding pickup ions plotted vs their lit vs unlit measure with the median identified in red. The lit vs unlit ratio is determined by taking the grid for each data point (see Figure 4.11 for an example) and subtracting the number of unlit points from the number of lit points divided by the total number of grid points over the effective surface range of 400 km. If the enhanced lofting provided by differences in charging for the solar wind wake around a topographical feature was a significant contribution to the integrated signal, we would expect an increase in larger signals as the lit vs unlit ratio approaches 0. Instead, there appears to be no significant increase near 0 with a slight increase approaching 1 (i.e. the surface is entirely lit) [15].

signal to increase as the lit vs unlit measure approaches 0 (i.e. 50% lit 50% unlit) and decrease as it approaches ± 1. To account for the entirety of the spike in Figure 4.10, the mean integrated signal near 0 lit vs unlit measure should show a $\sim 10^5$ e s^{-1} increase compared to ± 1 lit vs unlit measure. Instead, Figure 4.13 shows no such trend with the average integrated signal instead only slightly increasing as the surface patch becomes more and more lit. Note that the 5 measurements identified in [126] are not included in this plot as their angle between the solar wind electric field and negative LDEX's boresight range from $69 - 104°$ which lies within the potential pickup ion range. These 5 measurements are also not outliers to the trend shown in Figure 4.13. For a more robust comparison, additional complexity may be added to this lit vs unlit measure such as a weight of Cos for the solar wind's angle compared to surface normal of the local topography to account for differences in solar wind flux or a weight based on the radial distance from the center of the patch as, depending on the anticipated initial velocity and angular distributions of the lofted dust, different distances will contribute more than others to the overall signal. However, as all points considered for Figure 4.13 are near the sunrise terminator, variations in solar wind flux should be minimal. Based on this initial trend we find no correlation to support enhanced electrostatic lofting by twilight craters to the LDEX integrated signal.

4.7 Discussion

By examining the reduced integrated current signal from LDEX, we identified several correlations that assist in constraining potential contributing sources. We excluded all signals for which the ambient solar wind electric field was not pointed out of the instrument thus removing periods where pickup ions would dominate the integrated signal [88]. From this initial collection of data, we examined the average integrated current binned over LT, SEL angle, and altitude grouped by forward and backward point regimes relative to LADEE's velocity (Figure 4.2 and 4.6). For the lunar night side enhance depicted by the blue box in Figure 4.5, a localization in Sun-Earth-LADEE angle indicates that these are measurements of the high temperature plasma in the Earth's magnetosheath corresponding to solar wind flowing directly into LDEX's FOV. This interpretation is further supported by correlation with *ARTEMIS* solar wind flux measurements interpolated to LADEE's position (See Figure 4.5) and correlation between negative and positive integrated currents measurements (Figure 4.2 compared to Figure 4.4) demonstrating that these are transient high energy signals. Grouped just within the Earth's bowshock opposite the Earth's orbital velocity for the forward pointing regime, these enhancements are likely due to the high temperature plasma environment produced at the boundary of the Earth's bowshock flowing directly into LDEX's FOV.

For the lunar day-side enhancement depicted by the red box in Figure 4.5, consistent enhancement with minimal apparent pointing dependence (See Figure 4.2 and 4.7) indicates that this enhancement is unlikely to be from electrostatic lofted dust or meteoroid ejecta grains as these should predominately appear in the forward pointing regime due to their low speeds relative to spacecraft velocity. Additionally, the lack of negative integrated current signals (See Figure 4.4) and corresponding solar wind flux residing outside of LDEX's FOV (See Figure 4.5) shows that these are not simply high energy transient signals from a volatile plasma environment. Reflected solar wind ENAs seem the most likely candidate as they should reach speeds much greater than the lunar escape velocity and thus spacecraft velocity [36, 123, 34]. Figure 4.8 demonstrates a strong linear correlation with solar wind ion to surface flux as measured by *ARTEMIS* further supporting the ENA interpretation. Based upon the average backscattered fraction as measured by *Chandrayaan-1* [35], LDEX need only have an ENA collection efficiency of 0.01% to match the anticipated ENA flux. Solar wind ions that remained ions upon backscattering from the lunar surface or re-ionized in the lunar exosphere cannot account for the day-side enhancement as we note no correlation with solar wind magnetic field vector to LDEX's boresight (see Figure 4.9).

For constraining the pointing dependent contribution (presumably from small ejecta or lofted dust grains < 0.3 μm), we reduced mean forward pointing integrated current values by corresponding backward pointing means. The day-side produced no consistent pointing dependent contribution suggesting a lack of small ejecta or lofted dust grains over the altitude range observed by LDEX. This estimate, however, does not include the yet unconstrained velocity dependence of ENA detection by LDEX. For the reduced night-side current, no apparent enhancement is present at the antihelion sporadic background radiant indicating that the population of impact ejecta of size < 0.3 μm produce by antihelion (and presumably helion) meteoroids is negligibly small for the altitudes observed by LDEX. A significant enhancement near 5 LT is likely due to a change in spacecraft charging upon entering the lunar optical shadow.

While unlikely for the majority of the day-side, we considered all points near the lunar sunrise terminator to identify the potential for electrostatic lofted dust enhanced by solar wind wake charging around large topographical features. As a first order check, a grid over an effective surface range of 400 km was generated for each detection period from which each grid point was identified as ‘unlit’ vs ‘lit’ respective of whether the solar wind’s path was blocked or not by changes in elevation. From these collection of grid points, we generated a measure from the number of lit points minus the number of unlit points divided by the total. The expectation from this being that if lofting from twilight craters was a prominent contributor to LDEX integrated current measurements, that the median value would peak near 0. From Figure 4.13 we see not such trend. This combined with the lack of pointing dependence suggests that electrostatic lofting is not a prominent contributing component to the LDEX integrated current.

Chapter 5

IDPs Beyond 1 AU

The results presented in this section provide an updated look at the IDP distribution up to 50 AU as measured by the Venetia Burney Student Dust Counter (SDC) aboard the *New Horizons* spacecraft and prior numerical model predictions [90, 89] with additional measurements in the near future expected to bring further constraint on the peak IDP location produced from EKBOs. Section 5.1 briefly reviews the layout and basic operation. Section 5.2 covers the calibrated SDC measurements to date. Using these measurements, Sections 5.3 and 5.4 provide updated IDP flux and density estimates respectively for different size cutoffs with updated methodology to how they are derived from prior publications.

5.1 SDC Instrument Description

SDC consists of an array of 14 impact sensors, permanently polarized polyvinylidene fluoride (PVDF) films each with an area of 14.2 cm $\times$ 6.5 cm and 28 μm thick as shown in Figure 5.1 [48]. Dust impacts are measured from changes in the surface charge density due to cratering, a function of both the mass m, and the impact speed v of the particle [97, 87, 53]. The instrument is also sensitive to mechanical vibrations. For this reason, 12 panels reside on the exposed front while the remaining 2 are unexposed to dust impacts on the underside and act as a means of noise characterization and mitigation during ground data processing. Additionally, panels are grouped into 2 separate rows with 1 reference channel each and record impacts through separate analog to digital converters (ADCs) labeled as sides A and B. These panels are mounted on a frame to the

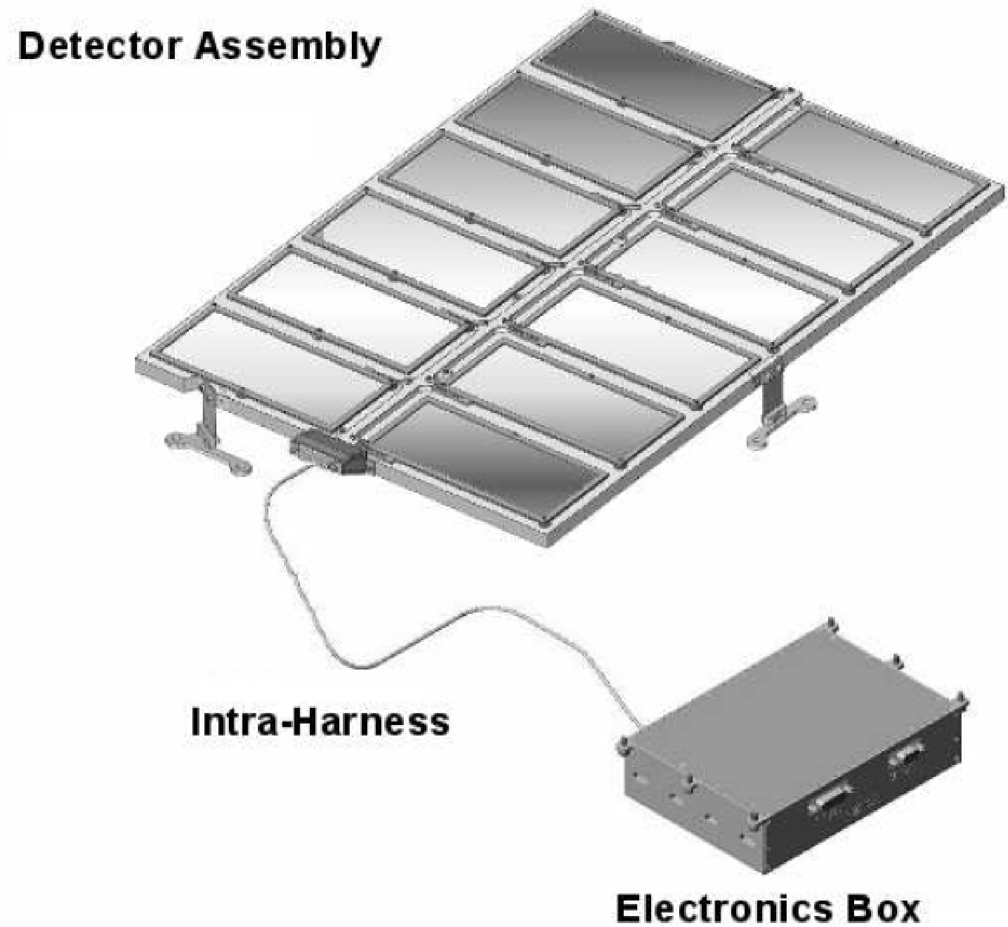

Figure 5.1: Illustration of the SDC instrument aboard the *New Horizons* spacecraft taken from its PDS node. The front panel consists of 12 permanently polarized polyvinylidene fluoride (PVDF) films with 2 reference films on the back grouped into 2 separate analog to digital converters by row. Dust grains are measured via changes in the surface charge density as a result of impact cratering on the films.

exterior of New Horizons facing the spacecraft's ram during nominal operation. Signals from the panels are recorded by the instruments electronic box within the spacecrafts interior opposite the detector panels.

Electronic noise and possible instrument sensitivity degradation are monitored via periodic noise and charge stimulus tests. Noise tests consist of measuring all hits for each channel at thresholds initially far below operation values followed by increasing steps in threshold value producing rates per threshold [48]. These noise tests are also used to determine threshold values for periods of high activity such as encounter flybys [8]. Charge stimulus tests are used to detect possible electronics degradation by injecting a known charge via a capacitor into each electronic chain. All channels are monitored and show minimal or no changes changes since launch. An in depth analysis of relative channel sensitivities and differences between the A and B sides of the instrument is described comprehensively in the literature [83].

For the purpose of ground data processing, calibrations from the 2 MV Van de Graaff dust accelerator at the Max Planck Institute for Nuclear Physics performed before launch are used with an assumed Keplerian IDP velocity modified by radiation pressure and added in quadrature with *New Horizons* velocity to convert the charge measurements to mass [48, 53]. For this conversion, all dust grains are assumed to follow circular Keplerian, prograde orbits modified by radiation pressure. Valid hits (i.e. those excluding coincidences between channels or with spacecraft thruster firings) are used to produce flux and density estimates.

5.2 SDC Measurements out to 50 AU

Figure 5.2 shows the trajectory of *New Horizons* to date, enabling a near continuous measurement of the interplanetary dust environment by SDC to 50 AU. As each dust impact is detected as a single charge amplitude, this measure alone is not enough to distinguish real dust hits from piezoelectric or pyroelectric noise. To filter out such noise contributions, some measurements are flagged as 'coincidence' during ground data processing. Hits that occur within a second of a thruster firing are most likely acoustic noise events. Similarly, hits on multiple channels at the same time are likely noise events as the expected dust impact rate is $\sim$ one hit per week, hence such hits are likely due to mechanical vibrations from the spacecraft propagating through multiple panels.

Figure 5.3 shows all non-coincidence data as a function of heliocentric distance. As SDC measures impact charge, which is a function of both the mass and speed of the dust with respect to the instrument [48, 53, 87, 84, 83], a velocity and bulk mass density for the dust grain must be assumed to convert to mass. We use the standard silicate mass density for IDP of 2.5 g/cm^3 with speeds derived from assuming circular Kepler orbits modified by radiation pressure for the dust grains. Missing segments in the coverage of Figure 5.3 are either from the instrument being off during those time periods for operational requirements or raised thresholds for all channels to allow SDC to remain turned on during active spacecraft operation, such as the Pluto and Arrokoth flybys. The rising minimum value in the mass with increasing distance is due to the spacecraft slowing down as it travels further out of our solar system raising the minimum detectable mass as shown in Figure 5.2.

To compare flux and density estimates as a function of distance and across all channels, a common mass cutoff threshold must be used. Due to the decrease in spacecraft speed, the cutoff thresholds used in this paper are larger than those in prior publications. We use a size cutoff for the IDP grain radius $r_g > 0.63$ μm to allow for all channels to contribute to the estimate given the decreasing spacecraft speed.

5.3 Flux Estimates

For estimates of interplanetary dust flux onto SDC, we consider all non-coincidence data above a set size cutoff. Here we use a size cutoff for the IDP grain radius $r_g > 0.63$ μm to allow for all channels to contribute to the estimate given the decreasing spacecraft speed discussed earlier. Counts are then binned in time or heliocentric distance and rates are calculated per science panel with the following expression,

$$\tilde{r}_{si} = \frac{N_{si}}{dt_{si}} - \frac{N_{ri}}{dt_{ri}}, \tag{5.1}$$

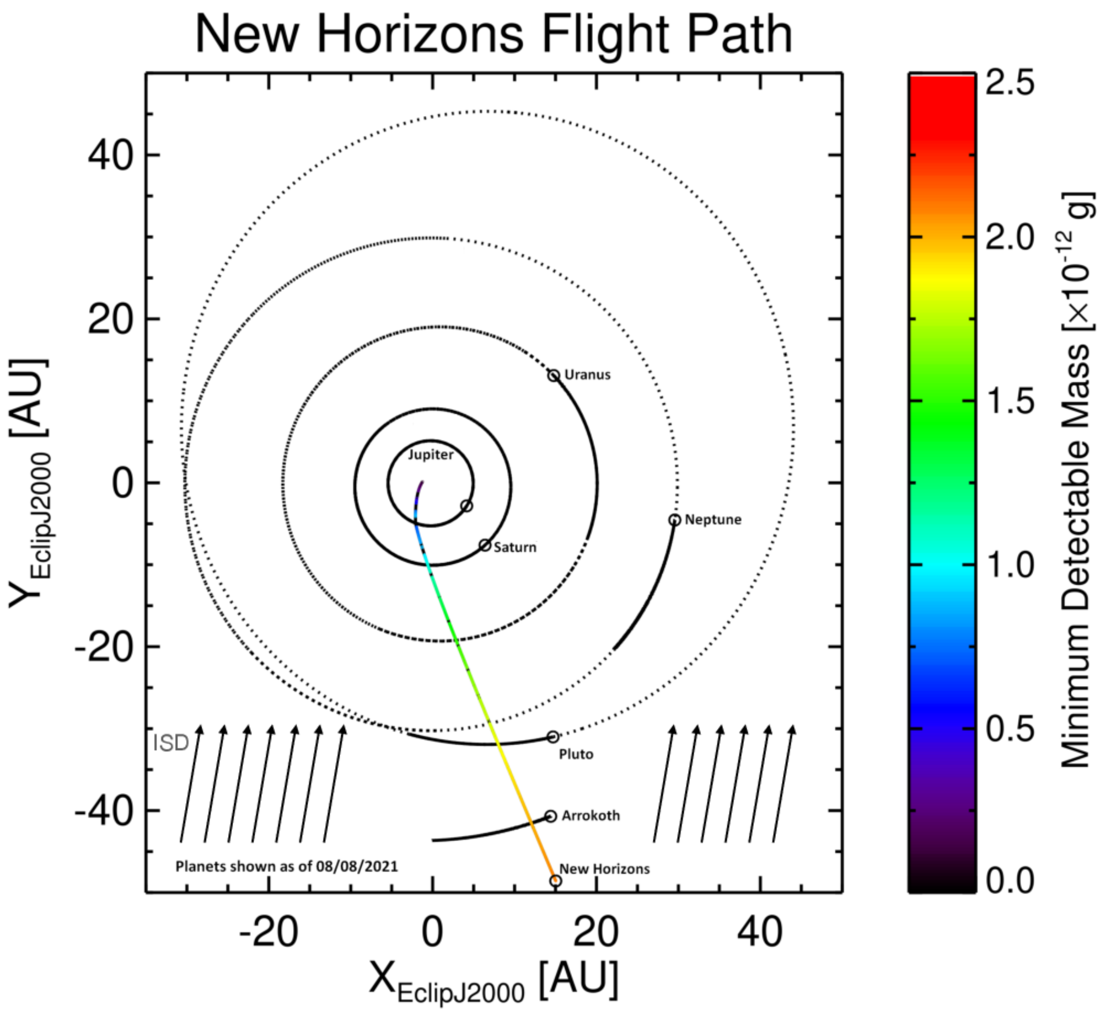

Figure 5.2: The trajectory of *New Horizons* past 50 AU. The decrease in spacecraft speed with increasing distance results in a higher minimum detectable mass, clearly identified in the bottom panel of Figure 5.3. *New Horizons* is now heading along an ecliptic longitude $\lambda_{NH} = 293°$ compared to the interstellar dust inflow of $\lambda_{ISD} \simeq 259°$, indicated by the parallel upward pointing arrows at the bottom. Considering the magnitude of their speeds results in an impact angle of ISD onto SDC of $\alpha \simeq 23°$ [16].

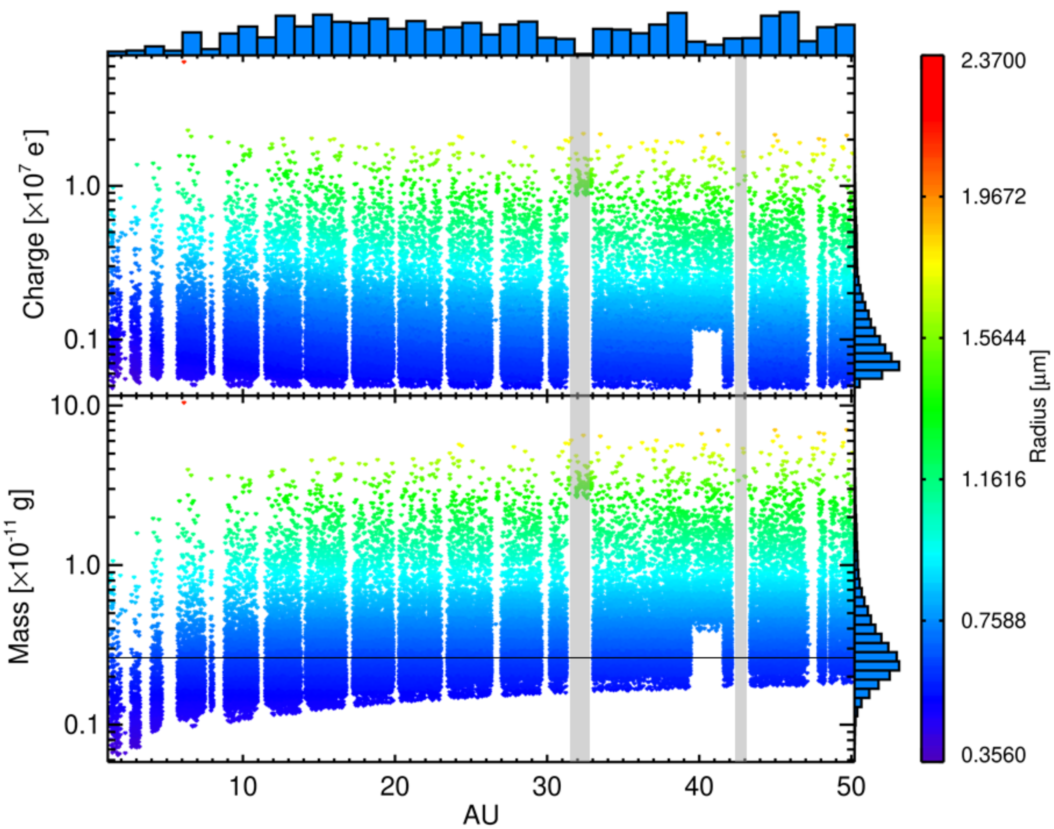

Figure 5.3: Plot of impact charges (*Top*) and mass estimates (*Bottom*) of all dust events recorded by SDC up to 50 AU excluding those flagged as coincidence events. Gray bars indicate Pluto and Arrokoth flybys and a black horizontal line in the bottom plot indicates the 0.63 μm cutoff used for flux and density estimates, allowing for both A and B sides to contribute [84]. Mass estimates assume silicate-dominated IDP grains with a density of 2.5 g/cm^3 following circular Kepler orbits modified by radiation pressure. Histogram bars are included for both distance and Charge/Mass bins on their corresponding axes [16].

where N_{si} is the total valid counts on science channel i over the given bin and dt_{si} is the total valid on time for science channel i with thresholds below the given size cutoff. N_{ri} and dt_{ri} are the same respective quantities for the corresponding reference channel on the same electrical chain (A or B). Errors and averages are calculated as the standard deviation and mean of this reduced rate per bin shown in Figure 5.4 for the size cutoff of IDP grain radius $r_g > 0.63\ \mu$m. Additionally, any channels for which their respective reference channel measured a higher rate were treated as having a reduced rate of zero for the purposes of averaging. Each channel was also required to cover a valid on time dt_{si} of at least 10% of the total time bin to be included in the average. Each electrical chain side (A or B) must additionally have more than one science channel to contribute.

It is important to note that these flux estimates differ slightly from the approach used in prior publications when it comes to determining the valid operation times as part of the initial rate calculation per channel. Previously, time bins were selected such that all channels were on with an appropriate cutoff threshold over the entire bin. Recent changes in SDC flight operation have resulted in frequent instrument threshold changes to allow for continued operation during frequent data downlinks and other activities. To account for this, we now use the new tracked threshold settings (labeled as 'sdc_chn_lvl_dn.tab' in recent PDS data releases), combined with SDC on/off times to determine the total time that a channel is on and below the given mass cutoff threshold per time bin.

Plotted alongside flux estimates from SDC in Figure 5.4 are predictions from [90, 89] assuming only IDP detections (solid curve). The outer solar system's IDP distribution is dominated by production from mutual collisions [101] and bombardment from interstellar and interplanetary dust [127] of EKBO. Beyond 42 AU, the gradually decreasing trend in the fluxes as function of distance could indicate that *New Horizons* has passed the peak density of the parent EKBO distribution, thereby approaching the outer edge of our dust disk populated mainly by small particles forced onto eccentric orbits by radiation pressure effects [59]. The conversion from impact charge to mass, however, is appropriate for IDP only, and must be revisited for the possible detection of interstellar dust (ISD) particles that flow through the solar system coincident with the flow of interstellar H

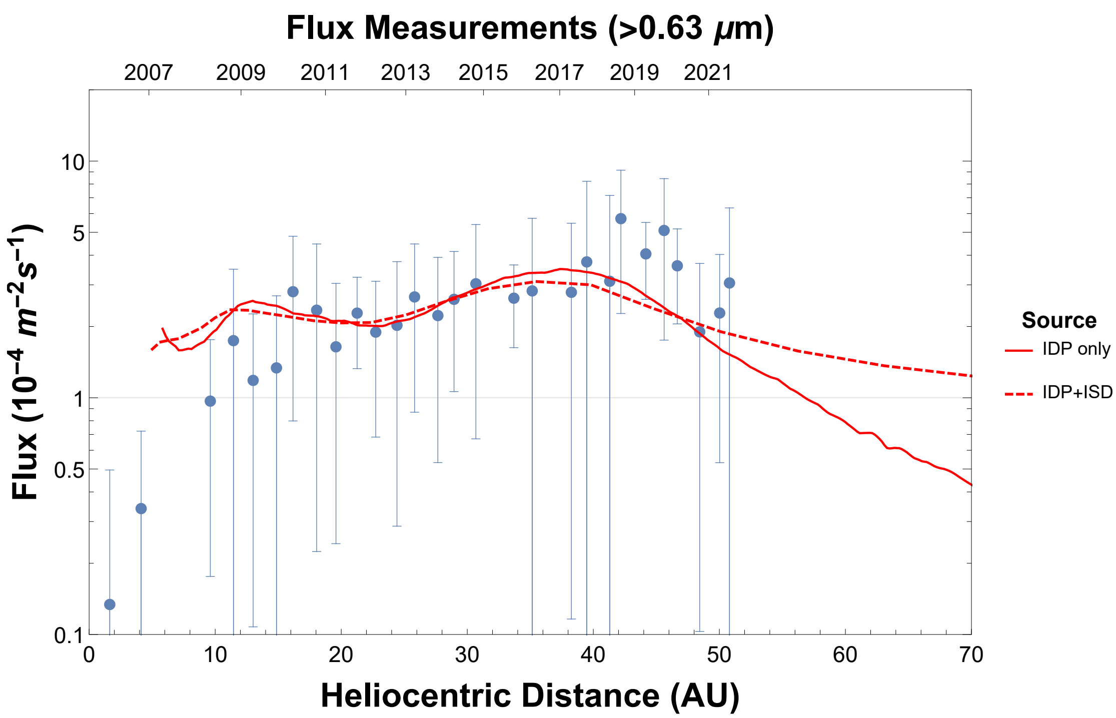

Figure 5.4: Plot of the estimated dust flux onto SDC for grains with IDP radii > 0.63 μm. The two red curves demonstrate the model given by [90, 89] fitted to SDC measurements assuming only IDP detections (solid curve) or an updated version assuming an additional constant ISD contribution of 10^{-4} m^{-2}s^{-1} (dashed curve) indicated by the horizontal grey line [16].

and He with speeds $\simeq 26$ km/s [41, 33, 71].

5.3.1 ISD Contribution

Due to the relative motion of the heliosphere with respect to the local interstellar medium, interstellar neutral atoms and dust particles (ISD) flow through our solar system with speeds $\simeq 26$ km/s [33, 71]. The first in situ detection of interstellar dust was made by *Ulysses* in 1992, during its encounter with Jupiter, sending the spacecraft on a solar polar orbit [41]. Subsequently, *Ulysses* monitored the variability of the ISD flux for $\simeq 16$ years noticing strong temporal variability with solar cycle, reaching a maximum of $\simeq 1.8\times10^{-4}$ m^{-2}s^{-1} in 1992 and 2006, and a minimum of $\simeq 10^{-5}$ flux in 2000 [103]. The mass of the vast majority of ISD detected by *Ulysses* was estimated to be 2.8×10^{-16} kg (or $\simeq 0.3$ μm with our assumed density of 2.5 g/cm^3), with diminishing contribution from larger or smaller particles [67, 64]. Following the *Ulysses* discovery, the reanalysis of data from *Helios* and *Galileo* also identified ISD [65, 2, 9, 3, 4]. *Cassini*, in orbit around Saturn for $\simeq 13$ years (of which $\simeq 10$ years was used for the following estimate), recorded an average flux $\simeq 1.5\times10^{-4}$ m^{-2}s^{-1}, based on 36 ISD hits, also identifying their composition as magnesium-rich grains of silicate and oxide composition [5]. The characteristic ISD size of $\simeq 0.3$ μm indicates that the ratio of radiation pressure over solar gravity $\beta \simeq 1$, hence these grains would cross our solar system on approximately straight line trajectories as shown in Figure 5.2. However, in addition to gravity and radiation pressure, dust particles in this size range also respond to electromagnetic forces as they carry a positive charge and react on interplanetary magnetic fields, resulting in temporal variability of the ISD flux with solar cycle, alternating between periods of focusing towards and away from the ecliptic plane [66, 98, 102, 99]. While the basic interactions of ISD within the heliosphere appear to be well understood, our current models (calibrated using *Ulysses* data) can only reproduce the measurements of all spacecraft data of the variability of their flux measured to date within a factor of 2 to 3 [63]. Hence, the question arises whether or not SDC detected ISD during its 15-year cruise across the solar system?

SDC records dust particles through the charge amplitude they generate as function of their

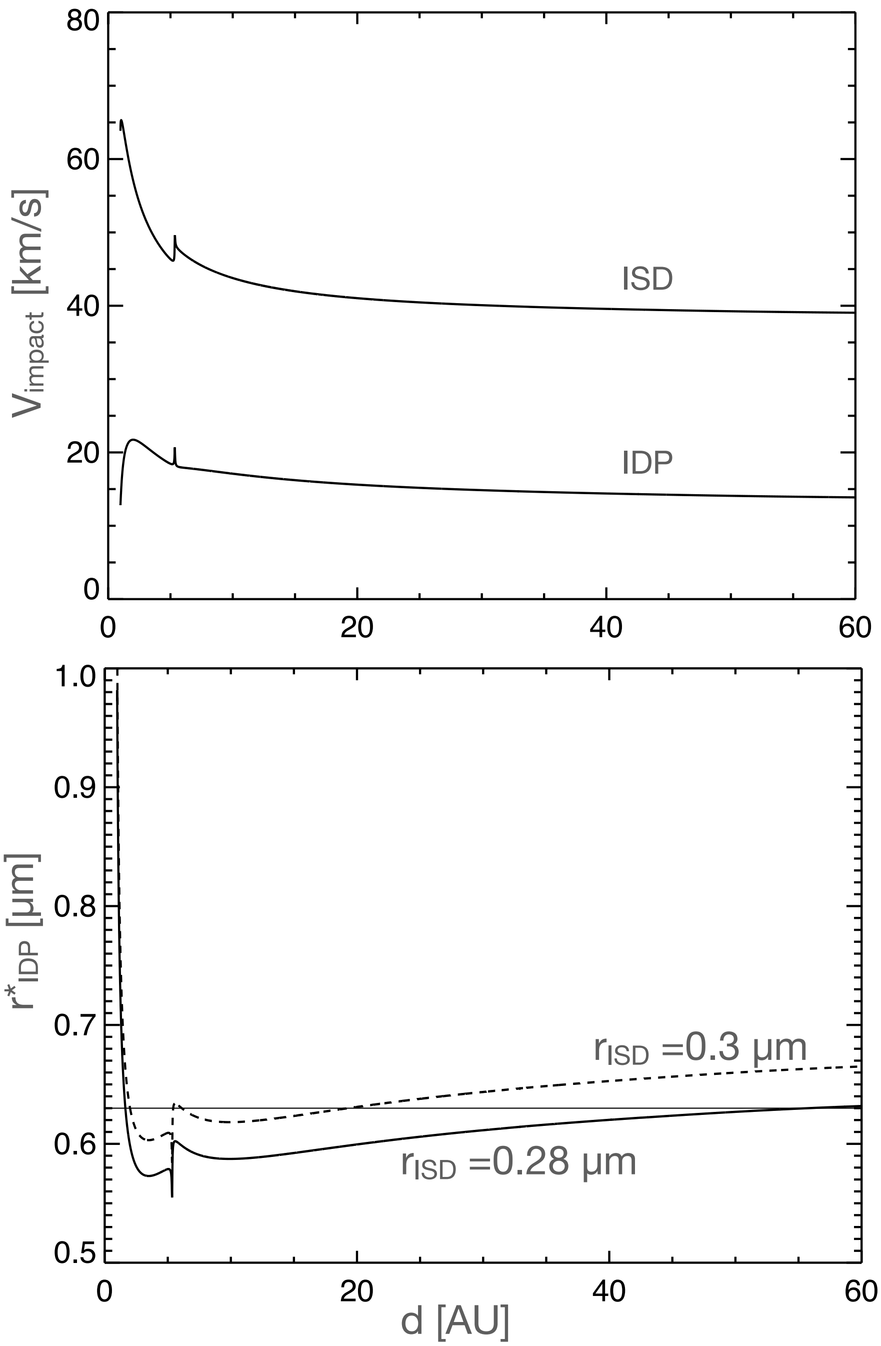

Figure 5.5: The impact speed of ISD and IDP (*Top*), and the equivalent IDP size of 0.28 and 0.3 μm radius ISD (*Bottom*) as function of heliocentric distance [16].

impact speed v and mass m [48, 53, 82]

$$N_e\ [e] = 5.63 \times 10^{17} m\ [\mathrm{g}]^{1.3} \mathrm{v}\ [\mathrm{km/s}]^{3.0}. \tag{5.2}$$

The traditional SDC analysis assumes that IDP follow circular Kepler orbits modified by radiation pressure to calculate their impact speed. Hence, according to Eq. 5.2, the much smaller and faster ISD will be assigned a larger IDP mass. With an expected size of 0.3 μm, speed of $\simeq$ 26 km/s, and ecliptic longitude of $\lambda_{ISD} \simeq 259°$ show in Figure 5.2, we can predict what size SDC would mistake these ISD impacts as [33, 71, 67, 64, 63]. Figure 5.5 (*Top*) shows the anticipated impact speed of a 0.3 μm ISD compared to the assumed speed used in the IDP conversion from charge to mass in Figure 5.3. From the charge produced for a 0.3 μm ISD with its expected impact speed converted to size using the assumed IDP speed, we produce the SDC pipelines size interpretation of ISD impacts as a function of heliocentric distance shown in Figure 5.5 (*Bottom*). The typical 0.3 μm ISD grain is interpreted as larger than a 0.63 μm for most of SDC's current coverage and thus should contribute at our current mass cutoff threshold.

This detectability, however, is quite close to the cutoff threshold with only a size difference of 0.02 μm pushing nominal ISD detectability below the cutoff threshold. As mentioned previously, the 0.3 μm estimate was done using data primarily from the defocusing phase of the solar cycle, and thus the nominal ISD size is likely a smaller. Velocity values are also subject to uncertainty from the aforementioned factor of 2 to 3 in their flux measurements [63]. For this reason, we present two model fits in Figure 5.4 for the purpose of comparing with SDC flux measurements. For one case (solid curve), we assume only IDP detections following the model given by [90, 89] (i.e. the ISD contribution is just below the IDP size cut off of 0.63 μm). For the second (dashed curve), we assume a potential average ISD flux contribution of 10^{-4} m^{-2}s^{-1} as observed by *Ulysses* in addition to the IDP model presented in [90, 89]. From these two cases, we provide a prediction of what SDC is expected to measure beyond 50 AU given ISDs are currently contributing to our flux values vs only IDPs are currently measured by SDC. The potential contribution of ISDs should become increasingly apparent with additional detections beyond 50 AU as indicated by the divergence in the two model fits in Figure 5.4.

5.4 Density Estimates

For SDC estimates of interplanetary dust densities, we continue with the same valid time selection scheme used for the flux estimates. We now require additional velocity information for determining the volume carved out per detector panel for each valid time range

$$V = A_{det} \int_{T_1}^{T_2} \hat{\mathbf{n}}_{SDC} \left(\mathbf{v}_{sc} - \mathbf{v}_{dust} \right) dt, \tag{5.3}$$

where T_1 and T_2 are the start and stop times of one valid time segment within the temporal bin, respectively. The total volume over the entire temporal bin is then a sum of all such segments. A_{det} is the area of a single detector panel, $\hat{\mathbf{n}}_{SDC}$ is the surface normal of the detector panel, $\mathbf{v}_{sc}$ is New Horizon's velocity vector, and $\mathbf{v}_{dust}$ is the dust velocity vector assuming circular Kepler velocities modified by radiation pressure. In the same manner as the flux estimates, each science panel's density estimate is reduced by its respective reference channel and averaged with errors calculated as the standard deviation across all contributing channels. Any channels for which their respective reference channel measured a higher density were again treated as having a reduced density of zero for the purposes of averaging. Figure 5.6 shows IDP density estimates at four size cutoffs: 0.63 μm, 0.68 μm 0.82 μm, and 1.5 μm. The 0.63 μm cutoff corresponds to the minimum cutoff allowed for all panels to contribute to the estimate in the last time bin while the 0.68 μm cutoff corresponds to the minimum cutoff to remove the expected ISD contribution derived from Figure 5.5. The 0.82 μm comes from the same consideration but for 'medium' threshold settings while 1.5 μm is derived from the threshold settings used during the Pluto and Arrokoth flybys and three-axis periods. For dust grains with radii > 0.63 μm, the density demonstrates an increase up to and through the Kuiper Belt. Comparing this to the 20-40 km^{-3} estimated by the Voyager spacecraft shows a reasonable agreement with SDC observations [43, 44]. Note, however, that while the quoted size threshold for this estimate is ~ 1 μm, the mass-to-charge conversion factor can vary by up to a factor of ten leading to a possible size threshold of $\sim 0.5 - 2.3$ μm [43]. For this reason, we include the estimate in the 0.63 μm size cutoff of Figure 5.6 though the thresholds between the two may sightly differ.

Figure 5.7 shows the total modeled interplanetary dust densities in the ecliptic plane, in a Neptune-rotated frame, summed over all three dust sources (EKB, OCC, and JFC) and all sizes (0.5 to 500 micron radius) with total production rates for EKB, OCC, and JFC dust grains from [89]. The dot and dashed line at 30 AU denote the position and orbit of Neptune, respectively. Local maxima in the density are found (i) within 1 AU from combined EKB and JFC contributions undergoing Poynting-Robertson drag into the inner heliosphere, (ii) near 10 AU from EKB grains trapped in mean-motion resonance with both Saturn and Jupiter, and (iii) centered on 40 AU from direct production from EKBO and trapping in mean-motion resonance with Neptune. The peak density in the EKB reaches approximately 75 km^{-3} for all grains >0.5 μm, while the peak density for those grains >0.63 μm (i.e. the SDC minimum detectable size used here) is approximately 35 km^{-3}, commensurate with the SDC data shown in Figure 5. Under the assumption that there is not an additional distant component to the EKB beyond what is currently anticipated [80], the total IDP densities at 50 and 100 AU gradually decline to 45 km^{-3} and 5 km^{-3}, respectively.

5.5 Summary

With *New Horizons* passing 50 AU, we now have direct measurements of the IDP environment from SDC through most of the Kuiper Belt. Under the assumption of circular Kepler orbits for the dust grains, we present mass distribution measurements, estimates for the IDP flux to SDC, and density as function of distance from the Sun. For dust grains with $r_g > 0.63$ μm, SDC flux estimates approaching the outer Kuiper Belt seem to follow our latest models [90, 89], that are based upon dust production from the currently anticipated parent EKB distribution [80].

While we anticipate ISDs should contribute to SDC flux values as shown by Figure 5.5, this contribution should become increasingly apparent beyond 50 AU as *New Horizons* leaves the EKBO-generated IDP distribution (see Figure 5.4). The *New Horions* spacecraft is healthy and could continue operating through the 2030s, reaching a heliocentric distance of 90 to 100 AU. SDC

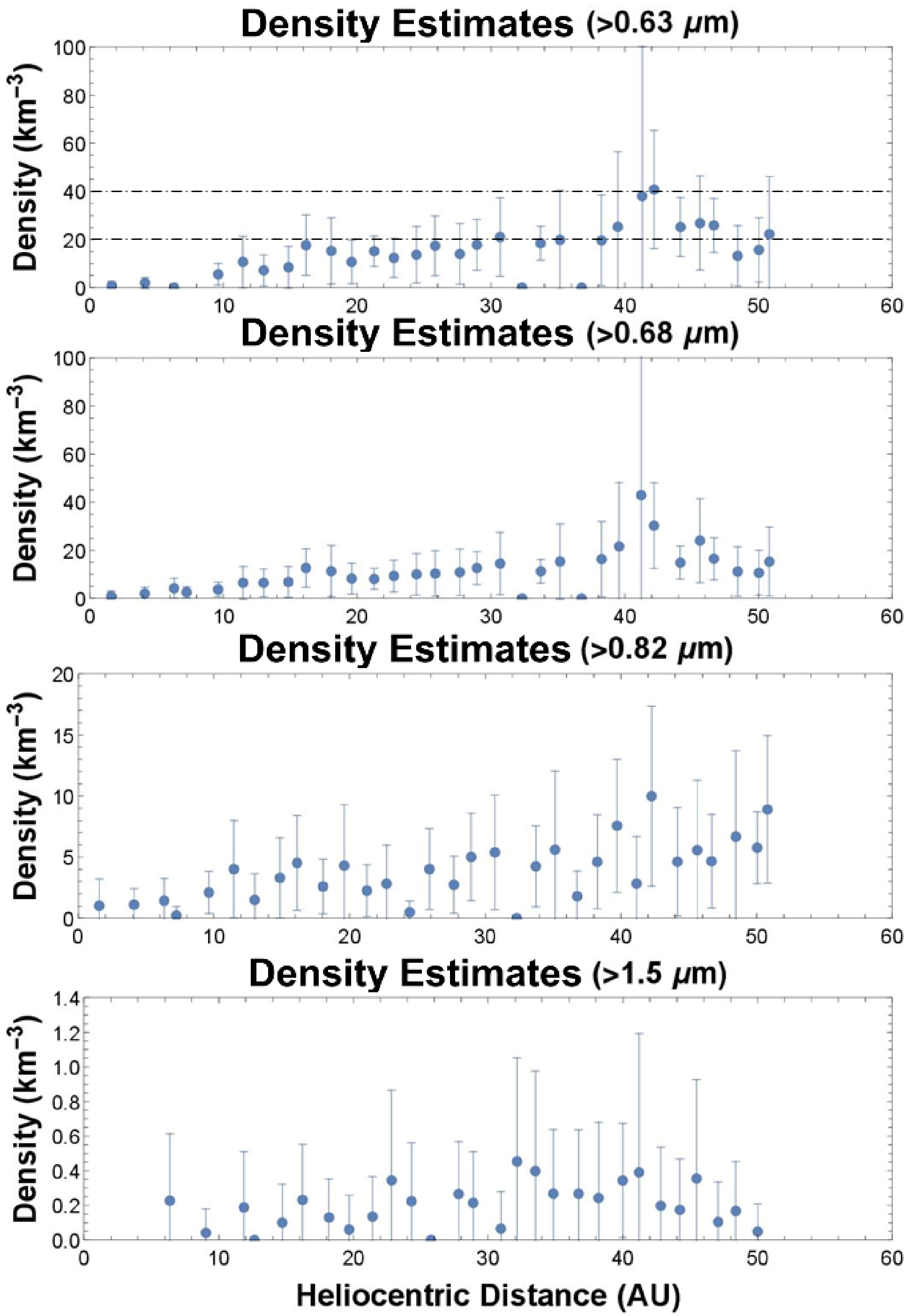

Figure 5.6: Plot of estimated IDP density for grains with radii > 0.63 μm (*First*), > 0.68 μm (*Second*), > 0.82 μm (*Third*), and > 1.5 μm (*Fourth*) as measured by SDC. Note that these estimates are upper limits on the IDP density as the contribution from ISD impacts is not removed. However, ISD impacts are not expected to contribute for thresholds above 0.68 μm. Voyager estimates from plasma wave data are indicated by dashed lines in the top plot. Points plotted at 0 with no error bars are empty bins either from containing no valid detections for any panel or no valid time coverage for any panel within that time period [16].

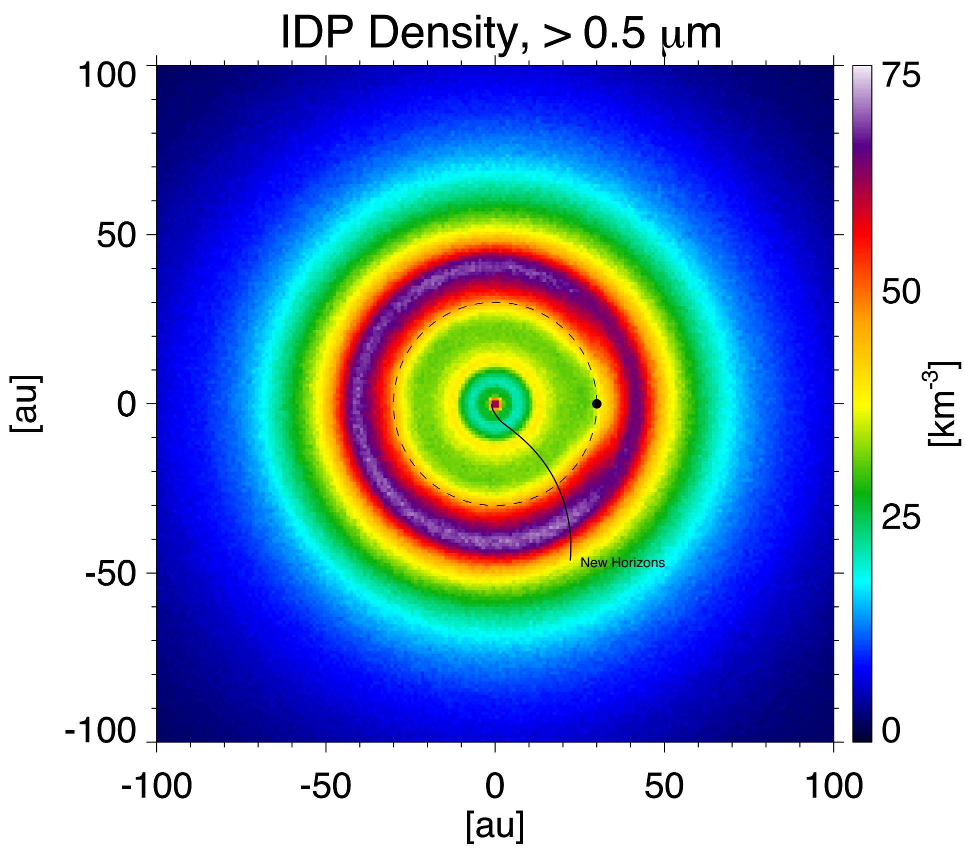

Figure 5.7: The total modeled IDP density in the Neptune-rotated frame. The dot and dashed line denote the position and orbit of Neptune, while the solid line denotes the trajectory of the New Horizons spacecraft [16].

will continue its measurements of the interplanetary dust fluxes in the outer solar system, detecting the collisional debris of the parent Edgeworth-Kuiper Belt objects.

SDC observations into the *terra incognita* $\gg 50$ AU will provide an unparalleled opportunity to learn about the large-scale structure of the EKB, constrain the upwind ISD fluxes, and offer unique insights into the interpretation of telescopic observations of dust disks around other stars.

Chapter 6

Future Work

The preceding sections have explored the IDP and airless body environment primarily through a modeling approach. While estimates are provided such as the mass flux and mass yield product for the sporadic background sources at 1 AU and the implications of an addition β-meteoroid source, each thrust could be improved in future works, whether that be to introduce additional complexity to better mirror observable phenomena or constrain additional parameters to connect with more physical quantities. The following section serves to summarized some of the more apparent improvements for future research projects.

One that concerns both Section 3 and 2 is the assumed azimuthal symmetry of the impact ejecta plumes. As mentioned in Section 2.3.1, azimuthal symmetry is chosen primarily for simplicity to avoid degeneracy in the ejecta cone angle fit as well as increased complexity in the model of Section 3. The effect of obliqueness of impact on the mass yield is accounted for with the relation in Equation 3.12 while the potential plume asymmetry is not. There exists compelling laboratory evidence for significant asymmetry in ejecta flow resulting from oblique impacts, as shown in Figure 6.1, though over different impactor parameters than the ones relevant to the plumes observed by LDEX [6]. This may also serve as a potential explanation for the surprisingly narrow outer ejecta cone angle of $8 \pm 3^\circ$ as an asymmetric plume structure could result in measurement of only half the plume. While we can argue that at least some of the identified plumes should be the result of normal incident impactors, a sample size of 19 is rather small. Implementing asymmetry in the fit described in Section 2 would require additional assumptions on the mass and speed of the

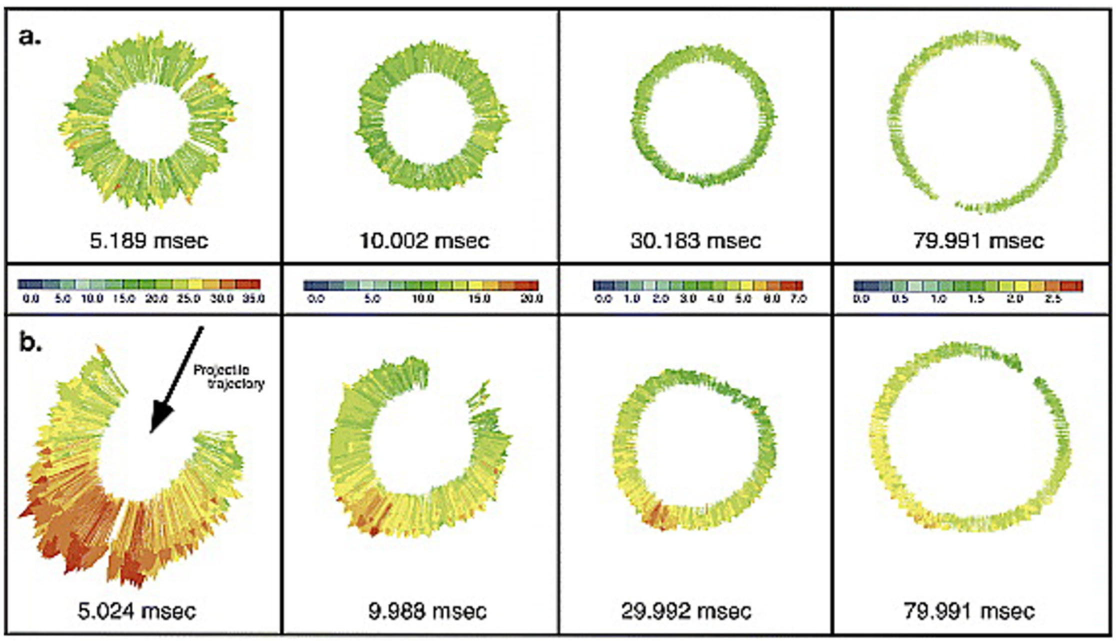

Figure 6.1: Vector plots of the ejecta velocities as measured by NASA Ames Vertical Gun Range experiment taken from [6]. This image demonstrates the asymmetry present for impacts at 30° in row (b) compared to impacts an impact at 90°.

impactors both of which have a significant degree of uncertainty. Restricting the set of identified to plumes to those correlated with meteoroid showers would alleviate this problem however. In contrast, introducing azimuthal plume asymmetry into the global three dimensional model of lunar ejecta environment would be fairly straightforward as the sporadic background source radiants in local time provide the necessary obliqueness of impact.

The global ejecta model and estimates discussed in Section 3 could benefit from a number of additions. For one, additional information on the ejecta mass yield as a function of impactor size and speed for lunar regolith would allow for the impactor mass flux to be decoupled from the model estimates. Alternatively, constraints on the sporadic background flux per source would allow for decoupling ejecta yield estimates from the model. Perhaps the most significant unknown in the global model is that of the maximum ejecta mass (m_{max}). The effect of m_{max} on the estimated product is discussed in Section 3.4 primarily as a result of M_s in Eqs. 3.2-3.5. While we do provide estimates using the maximum ejecta mass observed by LDEX of $m_{max} = 10^{-11}$ kg (10 μm), it is unclear whether this is the true maximum ejecta mass or simply the upper mass limit on LDEX, nor is it clear how this value changes with impactor parameters and surface properties. Constraints on this quantity are key to future implementation of the global ejecta model.

While the feasibility of ENA detection by LDEX's integrated current measurements is discussed in Section 4.4, full characterization of their contribution to the integrated signal and potential resulting estimates for the lunar day-side small ejecta or lofted dust grains < 0.3 μm requires its own global model. Prior studies on ENA reflection and production as a function of solar wind energy [36, 123, 34] and angle of incident [93] combined with interpolated solar wind measurements from *ARTEMIS* provide the necessary information for the initial setup of such a model. The most significant unknown in this case would be the re-ionization mechanism (if not the rate) by which LDEX detects these ENAs. Perhaps comparing the effect of each potential ionization mechanism and its variation with local time could distinguish the relevant physical phenomenon.

As for a hypothetical future mission with a similar instrument, there are several data sets that could significantly improve the estimates presented here. Flybys that include polar orbits would allow for incorporation of the toroidial meteoroid sources into the global ejecta model expanding upon the upper limit presented in Section 3.4. Pointing coverage that includes an LDEX equivalent instrument pointed toward the lunar surface could serve to constrain the ENA re-ionization mechanism and rate based upon expected velocity dependence. Finally, additional functionality to record the negative current component (i.e. electron and negative ion rate) could serve to characterize periods of ENA detection as ionization of neutral hydrogen via impact with a surface has the potential to produce as many negative ions as positive. These negative ions can be produced as a result of electron tunneling from a shift in the ENA's affinity level below the work function of the target metal as it approaches the grounded target [42]. These measurements would also act as a direct means of verifying the spacecraft charging hypothesis presented as an explanation for the peak observed in Figure 4.10.

Finally for SDC, while the flux estimates depicted in Figure 5.4 follow the model prediction of [90, 89], the peak flux rate appears in the 42 - 45 AU range as opposed to the modelled 38 AU. This indicates that the location of the EKBO distribution may need to be revisited for future comparisons. Additionally, we do not know if the ISDs potentially detectable to SDC fully penetrate the PVDF film instead of the typical cratering as the calibrations done for the instruments do not cover up to the speeds relevant to ISDs. This effect should be constrained for future comparisons to SDC data.

Chapter 7

Conclusion

The dust environment of our solar system provides unique insight into the dynamics and evolution of all bodies within it. Expanding upon prior LDEX results, we tackled unanswered questions concerning the lunar dust environment. First, generalized meteoroid impact ejecta dust distributions fitted to LDEX plume data produced cone angles far smaller than the expected $30°$. We expanded this search to a full three dimensional model to address as to whether the assumption of central plume trajectory sampling was the cause of the $< 10°$ outer cone angle fits. Similarly small outer cone angles, with an average of $8 \pm 3°$ were derived regardless of this consideration along with other extensions to the model. We posit that the deviation from laboratory observations may be do to the observed plume structures originating from reverse plumes. It may be the case that the anticipated $30°$ primary cone are only relevant for lower altitudes than those observed by LDEX as we find no evidence for a double cone structure under the same initial ejecta speed distribution.

Taking these ejecta plume distribution fits, We constructed a global three dimensional model of the entire lunar ejecta environment. Fully accounting for spacecraft trajectory considerations, new fits were produced for the dominant sporadic meteoroid background sources HE, AH, and AP as a product of meteoroid mass flux and mass ejecta yield. Determining one requires additional constraint on the other. LDEX lacks the latitudinal coverage to constrain NT and ST sources. We, however, estimate that there contribution could account for up to 22% of the AP contribution. Asymmetry between HE and AH persist counter to ground based observations despite these considerations. As a physical expansion for the phenomenon, we consider the implications of an additional source in the form of β-meteoroids and their feasibility based on prior flux observations and extrapolated laboratory yields. This comparison demonstrates that β-meteoroids could more than feasibly account for the HE excess. However, this is not definitely the case and could be due to a yet unconstrained contribution. Additionally, we address the effect that the assumed maximum ejecta mass has upon the estimate and provide secondary estimates using instead the largest ejecta observed by LDEX.

To determine potential smaller ejecta (< 0.3 μm) and electrostaticly lofted dust measurements, contributions to LDEX's integrated current were determined through trends and correlations with *LADEE*'s position with respect to the Earth's magnetosheath and local time, altitude, LDEX's pointing, and solar wind values interpolated from *ARTEMIS* observations. Most notable of these was the solar wind backscattered ENAs consistent across the entire lunar day-side. Comparisons between forward and backward pointing averages on the lunar night-side reveal a lack of small ejecta produced from meteoroid bombardment. To reexamine the case of electrostaticly lofted dust at the lunar terminates, we address the proposed mechanism of enhancement by differential charging between windward and leeward sides of twilight craters. As a check, we considered an effective surface range grid per integrated current measurement near 6 LT and determined whether the solar wind's trajectory to that element was interrupted by changes in elevation. Lack of correlation between the "lit" vs "unlit" measure and integrated current indicate that electrostatic lofting enhanced by twilight craters is not present in the LDEX data set.

Finally, we report IDP flux and density estimates out to 50 AU from SDC data using updated methodology. Current flux values continue the follow the model prediction of [90, 89] though the location of the EKBO distribution may need to be revisited. We demonstrate that detection if ISDs by SDC is likely given its operating mass thresholds and show that their contribution should become more apparent with additional measurements beyond 50 AU.

Bibliography

[1] N. Altobelli, V. Dikarev, S. Kempf, R. Srama, S. Helfert, G. Moragas-Klostermeyer, M. Roy, and E. Grün. Cassini/Cosmic Dust Analyzer in situ dust measurements between Jupiter and Saturn. J. Geophys. Res., 112(A11):7105, July 2007.

[2] N. Altobelli, E. Grün, and M. Landgraf. A new look into the Helios dust experiment data: presence of interstellar dust inside the Earth's orbit. A&A, 448:243–252, March 2006.

[3] N. Altobelli, S. Kempf, H. Krüger, M. Landgraf, M. Roy, and E. Grün. Interstellar dust flux measurements by the Galileo dust instrument between the orbits of Venus and Mars. Journal of Geophysical Research (Space Physics), 110(9):A07102, July 2005.

[4] N. Altobelli, S. Kempf, M. Landgraf, R. Srama, V. Dikarev, H. Krüger, G. Moragas-Klostermeyer, and E. Grün. Cassini between Venus and Earth: Detection of interstellar dust. Journal of Geophysical Research (Space Physics), 108:8032, October 2003.

[5] N. Altobelli, F. Postberg, K. Fiege, M. Trieloff, H. Kimura, V. J. Sterken, H. W. Hsu, J. Hillier, N. Khawaja, G. Moragas-Klostermeyer, J. Blum, M. Burton, R. Srama, S. Kempf, and E. Gruñ. Flux and composition of interstellar dust at Saturn from Cassini's Cosmic Dust Analyzer. Science, 352(6283):312–318, April 2016.

[6] J. L. B. Anderson, P. H. Schultz, and J. T. Heineck. Asymmetry of ejecta flow during oblique impacts using three-dimensional particle image velocimetry. Journal of Geophysical Research (Planets), 108:5094, aug 2003.

[7] J. R. Arnold. A Monte Carlo model for the gardening of the lunar regolith. Moon, 13:159–172, July 1975.

[8] F. Bagenal, M. Horányi, D. J. McComas, R. L. McNutt, H. A. Elliott, M. E. Hill, L. E. Brown, P. A. Delamere, P. Kollmann, S. M. Krimigis, M. Kusterer, C. M. Lisse, D. G. Mitchell, M. Piquette, A. R. Poppe, D. F. Strobel, J. R. Szalay, P. Valek, J. Vandegriff, S. Weidner, E. J. Zirnstein, S. A. Stern, K. Ennico, C. B. Olkin, H. A. Weaver, L. A. Young, G. R. Gladstone, W. M. Grundy, W. B. McKinnon, J. M. Moore, J. R. Spencer, T. Andert, J. Andrews, M. Banks, B. Bauer, J. Bauman, O. S. Barnouin, P. Bedini, K. Beisser, R. A. Beyer, S. Bhaskaran, R. P. Binzel, E. Birath, M. Bird, D. J. Bogan, A. Bowman, V. J. Bray, M. Brozovic, C. Bryan, M. R. Buckley, M. W. Buie, B. J. Buratti, S. S. Bushman, A. Calloway, B. Carcich, A. F. Cheng, S. Conard, C. A. Conrad, J. C. Cook, D. P. Cruikshank, O. S. Custodio, C. M. Dalle Ore, C. Deboy, Z. J. B. Dischner, P. Dumont, A. M. Earle, J. Ercol, C. M. Ernst, T. Finley, S. H. Flanigan, G. Fountain, M. J. Freeze, T. Greathouse,

J. L. Green, Y. Guo, M. Hahn, D. P. Hamilton, S. A. Hamilton, J. Hanley, A. Harch, H. M. Hart, C. B. Hersman, A. Hill, D. P. Hinson, M. E. Holdridge, A. D. Howard, C. J. A. Howett, C. Jackman, R. A. Jacobson, D. E. Jennings, J. A. Kammer, H. K. Kang, D. E. Kaufmann, D. Kusnierkiewicz, T. R. Lauer, J. E. Lee, K. L. Lindstrom, I. R. Linscott, A. W. Lunsford, V. A. Mallder, N. Martin, D. Mehoke, T. Mehoke, E. D. Melin, M. Mutchler, D. Nelson, F. Nimmo, J. I. Nunez, A. Ocampo, W. M. Owen, M. Paetzold, B. Page, A. H. Parker, J. W. Parker, F. Pelletier, J. Peterson, N. Pinkine, S. B. Porter, S. Protopapa, J. Redfern, H. J. Reitsema, D. C. Reuter, J. H. Roberts, S. J. Robbins, G. Rogers, D. Rose, K. Runyon, K. D. Retherford, M. G. Ryschkewitsch, P. Schenk, R. Schindhelm, B. Sepan, M. R. Showalter, K. N. Singer, M. Soluri, D. Stanbridge, A. J. Steffl, T. Stryk, M. E. Summers, M. Tapley, A. Taylor, H. Taylor, H. B. Throop, C. C. C. Tsang, G. L. Tyler, O. M. Umurhan, A. J. Verbiscer, M. H. Versteeg, M. Vincent, R. Webbert, G. E. Weigle, O. L. White, K. Whittenburg, B. G. Williams, K. Williams, S. Williams, W. W. Woods, and A. M. Zangari. Pluto' interaction with its space environment: Solar wind, energetic particles, and dust. Science, 351(6279):aad9045, March 2016.

[9] M. Baguhl, E. Grün, and M. Landgraf. In Situ Measurements of Interstellar Dust with the ULYSSES and Galileo Spaceprobes. Space Science Reviews, v.78, Issue 1/2, p.165-172., 78:165–172, 1996.

[10] O. S. Barnouin-Jha, S. Yamamoto, T. Toriumi, S. Sugita, and T. Matsui. Non-intrusive measurements of crater growth. Icarus, 188:506–521, jun 2007.

[11] O. E. Berg. A lunar terminator configuration. Earth and Planetary Science Letters, 39(3):377–381, May 1978.

[12] O. E. Berg, H. Wolf, and J. Rhee. Lunar soil movement registered by the Apollo 17 cosmic dust experiment. In H. Elsaesser and H. Fechtig, editors, Interplanetary Dust and Zodiacal Light, volume 48 of Lecture Notes in Physics, Berlin Springer Verlag, pages 233–237, 1976.

[13] Otto E Berg and Eberhard Grün. Evidence of hyperbolic cosmic dust particles. Space Research XIII, pages 1047–1055, 1973.

[14] Edwin Bernardoni, Mihály Horányi, and Jamey Szalay. Formation of the lunar dust ejecta cloud. The Planetary Science Journal, 2(2):67, apr 2021.

[15] Edwin Bernardoni, Mihály Horányi, and Jamey R. Szalay. Ldex integrated signal. The Planetary Science Journal, 2022 in preparation.

[16] Edwin Bernardoni, Mihály Horányi, Jamey R. Szalay, Alex Doner, Marcus Piquette, Andrew R. Poppe, David James, Silvan Hunziker, Veerle Sterken, Peter Strub, Cathy Olkin, Kelsi N. Singer, John Spencer, Alan Stern, and Harold Weaver. Student dust counter status report: the first 50 au. The Planetary Science Journal, 2022 in review.

[17] Edwin A. Bernardoni, Jamey R. Szalay, and Mihály Horányi. Impact ejecta plumes at the moon. Geophysical Research Letters, 46(2):534–543, 2019.

[18] R. Brunetto, M. J. Loeffler, D. Nesvorný, S. Sasaki, and G. Strazzulla. Asteroid Surface Alteration by Space Weathering Processes, pages 597–616. 2015.

[19] M.J. Burchell, M.J. Cole, and J.A.M. McDonnell. Role of particle charge in impact ionization by charged microparticles. Nuclear Instruments and Methods in Physics Research Section B: Beam Interactions with Materials and Atoms, 143(3):311–318, 1998.

[20] M. D. Campbell-Brown. High resolution radiant distribution and orbits of sporadic radar meteoroids. Icarus, 196:144–163, July 2008.

[21] Margaret Campbell-Brown and J Jones. Annual variation of sporadic radar meteor rates. Monthly Notices of the Royal Astronomical Society, 367(2):709–716, April 2006.

[22] J D Carrillo-Sanchez, David Nesvorny, Petr Pokorný, Diego Janches, and John M C Plane. Sources of cosmic dust in the Earth's atmosphere. Geophysical Research Letters, 43(23):11,979–11,986, December 2016.

[23] M. J. Cintala, L. Berthoud, and F. Hörz. Ejection-velocity distributions from impacts into coarse-grained sand. Meteoritics and Planetary Science, 34:605–623, jul 1999.

[24] Emily S. Costello, Rebecca R. Ghent, and Paul G. Lucey. The mixing of lunar regolith: Vital updates to a canonical model. Icarus, 314:327 – 344, 2018.

[25] B. R. De and D. R. Criswell. Intense localized photoelectric charging in the lunar sunset terminator region, 1. Development of potentials and fields. J. Geophys. Res., 82:999, March 1977.

[26] Francesca E. DeMeo, Richard P. Binzel, Stephen M. Slivan, and Schelte J. Bus. An extension of the bus asteroid taxonomy into the near-infrared. Icarus, 202(1):160 – 180, 2009.

[27] H. Dietzel, G. Eichhorn, H. Fechtig, E. Grun, H.-J. Hoffmann, and J. Kissel. The HEOS 2 and HELIOS micrometeoroid experiments. Journal of Physics E Scientific Instruments, 6:209–217, March 1973.

[28] Martin J. Duncan and Harold F. Levison. A disk of scattered icy objects and the origin of jupiter-family comets. Science, 276(5319):1670–1672, 1997.

[29] W. Eckstein and R. Preuss. New fit formulae for the sputtering yield. Journal of Nuclear Materials, 320(3):209–213, 2003.

[30] Wolfgang Eckstein. Sputtering Yields, pages 33–187. Springer Berlin Heidelberg, Berlin, Heidelberg, 2007.

[31] W. M. Farrell, T. J. Stubbs, J. S. Halekas, R. M. Killen, G. T. Delory, M. R. Collier, and R. R. Vondrak. Anticipated electrical environment within permanently shadowed lunar craters. Journal of Geophysical Research (Planets), 115:3004, March 2010.

[32] P. D. Feldman, D. A. Glenar, T. J. Stubbs, K. D. Retherford, G. Randall Gladstone, P. F. Miles, T. K. Greathouse, D. E. Kaufmann, J. W. Parker, and S. Alan Stern. Upper limits for a lunar dust exosphere from far-ultraviolet spectroscopy by lro/lamp. Icarus, 233:106–113, May 2014.

[33] P. C. Frisch, M. Bzowski, E. Grün, V. Izmodenov, H. Krüger, J. L. Linsky, D. J. McComas, E. Möbius, S. Redfield, N. Schwadron, R. Shelton, J. D. Slavin, and B. E. Wood. The Galactic Environment of the Sun: Interstellar Material Inside and Outside of the Heliosphere. Space Science Reviews, 146:235–273, August 2009.

[34] H. Funsten, F. Allegrini, P. Bochsler, S. Fuselier, Mike Gruntman, Kevin Henderson, P. Janzen, R. Johnson, B. Larsen, D. Lawrence, David Mccomas, E. MöBius, D. Reisenfeld, Diego Rodriguez Moreno, N. Schwadron, and Peter Wurz. Reflection of solar wind hydrogen from the lunar surface. Journal of Geophysical Research (Planets), 118:292–305, 02 2013.

[35] Y. Futaana, S. Barabash, M. Wieser, M. Holmstrom, C. Lue, P. Wurz, A. Schaufelberger, A. Bhardwaj, M. B. Dhanya, and K. Asamura. Empirical energy spectra of neutralized solar wind protons from the lunar regolith. Journal of Geophysical Research: Planets, 117(E5), 2012.

[36] Y. Futaana, S. Barabash, M. Wieser, C. Lue, P. Wurz, A. Vorburger, A. Bhardwaj, and K. Asamura. Remote energetic neutral atom imaging of electric potential over a lunar magnetic anomaly. Geophysical Research Letters, 40(2):262–266, Jan 2013.

[37] D. A. Glenar, T. J. Stubbs, J. E. McCoy, and R. R. Vondrak. A reanalysis of the Apollo light scattering observations, and implications for lunar exospheric dust. Planetary and Space Science, 59:1695–1707, November 2011.

[38] K. M. Gorski, E. Hivon, A. J. Banday, B. D. Wandelt, F. K. Hansen, M. Reinecke, and M. Bartelmann. HEALPix: A framework for high-resolution discretization and fast analysis of data distributed on the sphere. The Astrophysical Journal, 622(2):759–771, apr 2005.

[39] E. Grün and M. Horányi. A new look at Apollo 17 LEAM data: Nighttime dust activity in 1976. Planetary and Space Science, 89:2–14, December 2013.

[40] E. Grün, H. A. Zook, H. Fechtig, and R. H. Giese. Collisional balance of the meteoritic complex. Icarus, 62:244–272, May 1985.

[41] E. Grün, H.A. Zook, M. Baguhl, A. Balogh, S.J. Bame, H. Fechtig, R. Forsyth, M.S. Hanner, M. Horányi, J. Kissel, B.-A. Lindblad, D. Linkert, G. Linkert, I. Mann, J.A.M. McDonnel, G.E. Morfill, J.L. Phillips, C. Polanskey, G. Schwehm, N. Siddique, P. Staubach, J. Svestka, and A. Taylor. Discovery of Jovian dust streams and interstellar grains by the Ulysses spacecraft. Nature, 362:428–430, 1993.

[42] Mike Gruntman. Energetic neutral atom imaging of space plasmas. Review of Scientific Instruments, 68(10):3617–3656, 1997.

[43] D. A. Gurnett, J. A. Ansher, W. S. Kurth, and L. J. Granroth. Micron-sized dust particles detected in the outer solar system by the Voyager 1 and 2 plasma wave instruments. Geophys. Res. Lett., 24(24):3125–3128, January 1997.

[44] D. A. Gurnett, A. M. Persoon, L. Granroth, and W. S. Kurth. Interstellar Dust Detected by Voyager 1 Over Heliocentric Radial Distances From 5 to 132 AU. In AGU Fall Meeting Abstracts, volume 2015, pages SH53C–06, December 2015.

[45] B. A. S. Gustafson. Physics of Zodiacal Dust. Annual Review of Earth and Planetary Sciences, 22:553–595, 1994.

[46] D. Han, A. R. Poppe, M. Piquette, E. Grün, and M. Horányi. Constraints on dust production in the Edgeworth-Kuiper Belt from Pioneer 10 and New Horizons measurements. Geophys. Res. Lett., 38:24102, December 2011.

[47] Brendan Hermalyn, Peter H. Schultz, Mark Shirley, Kimberly Ennico, and Anthony Colaprete. Scouring the surface: Ejecta dynamics and the lcross impact event. Icarus, 218(1):654 – 665, 2012.

[48] M. Horányi, V. Hoxie, D. James, A. Poppe, C. Bryant, B. Grogan, B. Lamprecht, J. Mack, F. Bagenal, S. Batiste, N. Bunch, T. Chanthawanich, F. Christensen, M. Colgan, T. Dunn, G. Drake, A. Fernandez, T. Finley, G. Holland, A. Jenkins, C. Krauss, E. Krauss, O. Krauss, M. Lankton, C. Mitchell, M. Neeland, T. Reese, K. Rash, G. Tate, C. Vaudrin, and J. Westfall. The Student Dust Counter on the New Horizons Mission. Space Sci. Rev., 140:387–402, October 2008.

[49] M. Horányi, Z. Sternovsky, M. Lankton, C. Dumont, S. Gagnard, D. Gathright, E. Grün, D. Hansen, D. James, S. Kempf, B. Lamprecht, J. Szalay, R. Srama, and G. Wright. The Lunar Dust Experiment (LDEX) onboard the Lunar Atmosphere and Dust Environment Explorer (LADEE) mission. Space Science Reviews, 185:93 – 113, 2014.

[50] M. Horányi, J. R. Szalay, S. Kempf, J. Schmidt, E. Grün, R. Srama, and Z. Sternovsky. A permanent, asymmetric dust cloud around the Moon. Nature, 522(7556), 2015.

[51] Kevin R Housen, William J Sweet, and Keith A Holsapple. Impacts into porous asteroids. Icarus, 300:72–96, January 2018.

[52] D. H. Humes. Results of Pioneer 10 and 11 meteoroid experiments - Interplanetary and near-Saturn. J. Geophys. Res., 85:5841–5852, November 1980.

[53] D James, V Hoxie, and M Horányi. Polyvinylidene fluoride dust detector response to particle impacts. Review of Scientific Instruments, 81(3):034501, 2010.

[54] Diego Janches, Petr Pokorný, Menelaos Sarantos, Jamey Szalay, Mihaly Horanyi, and David Nesvorny. Constraining the Ratio of Micrometeoroids From Short- and Long-Period Comets at 1 AU From LADEE Observations of the Lunar Dust Cloud. Geophysical Research Letters, 45(4):1713–1722, February 2018.

[55] J. Jones and P. Brown. The radiant distribution of sporadic meteors. Planetary and Space Science, 42(2):123–126, 1994. Special Issue: Asteroids, Comets and Meteors 1993-I.

[56] J Jones and Peter Brown. Sporadic meteor radiant distributions - Orbital survey results. Monthly Notices of the Royal Astronomical Society, 265:524, December 1993.

[57] D. Koschny and E. Grün. Impacts into Ice-Silicate Mixtures: Crater Morphologies, Volumes, Depth-to-Diameter Ratios, and Yield. Icarus, 154:391–401, December 2001.

[58] D. Koschny and E. Grün. Impacts into Ice-Silicate Mixtures: Ejecta Mass and Size Distributions. Icarus, 154:402–411, December 2001.

[59] A. V. Krivov, T. Löhne, and M. Sremčević. Dust distributions in debris disks: effects of gravity, radiation pressure and collisions. A&A, 455(2):509–519, August 2006.

[60] A. V. Krivov, M. Sremčević, F. Spahn, V. V. Dikarev, and K. V. Kholshevnikov. Impact-generated dust clouds around planetary satellites: spherically symmetric case. Planetary and Space Science, 51:251–269, March 2003.

[61] H Krüger, Alexander V Krivov, Miodrag Sremčević, and Eberhard Grün. Impact-generated dust clouds surrounding the Galilean moons. Icarus, 164(1):170–187, July 2003.

[62] Harald Krüger, Peter Strub, Nicolas Altobelli, Veerle J. Sterken, Ralf Srama, and Eberhard Grün. Interstellar dust in the solar system: model versus in situ spacecraft data. A&A, 626:A37, June 2019.

[63] Harald Krüger, Peter Strub, Nicolas Altobelli, Veerle J. Sterken, Ralf Srama, and Eberhard Grün. Interstellar dust in the solar system: model versus in situ spacecraft data. A&A, 626:A37, June 2019.

[64] Harald Krüger, Peter Strub, Eberhard Grün, and Veerle J. Sterken. Sixteen Years of Ulysses Interstellar Dust Measurements in the Solar System. I. Mass Distribution and Gas-to-dust Mass Ratio. ApJ, 812(2):139, October 2015.

[65] Harald Kruger, Peter Strub, Ralf Srama, Masanori Kobayashi, Tomoko Arai, Hiroshi Kimura, Takayuki Hirai, Georg Moragas-Klostermeyer, Nicolas Altobelli, Veerle J Sterken, Jessica Agarwal, Maximilian Sommer, and Eberhard Grün. Modelling DESTINY+ interplanetary and interstellar dust measurements en route to the active asteroid (3200) Phaethon. Planetary and Space Science, 172:22–42, August 2019.

[66] M. Landgraf. Modeling the motion and distribution of interstellar dust inside the heliosphere. J. Geophys. Res., 105:10303–10316, May 2000.

[67] M. Landgraf, H. Krüger, N. Altobelli, and E. Grün. Penetration of the heliosphere by the interstellar dust stream during solar maximum. Journal of Geophysical Research (Space Physics), 108:8030, August 2003.

[68] Harold F. Levison and Luke Dones. Chapter 31 - comet populations and cometary dynamics. In Tilman Spohn, Doris Breuer, and Torrence V. Johnson, editors, Encyclopedia of the Solar System (Third Edition), pages 705–719. Elsevier, Boston, third edition edition, 2014.

[69] J.-C. Liou, H. A. Zook, and S. F. Dermott. Kuiper Belt Dust Grains as a Source of Interplanetary Dust Particles. Icarus, 124:429–440, December 1996.

[70] Robert Lunsford, editor. Sporadic Meteors, pages 3–10. Springer New York, New York, NY, 2009.

[71] D. J. McComas, M. A. Dayeh, F. Allegrini, M. Bzowski, R. DeMajistre, K. Fujiki, H. O. Funsten, S. A. Fuselier, M. Gruntman, P. H. Janzen, M. A. Kubiak, H. Kucharek, G. Livadiotis, E. Möbius, D. B. Reisenfeld, M. Reno, N. A. Schwadron, J. M. Sokół, and M. Tokumaru. The First Three Years of IBEX Observations and Our Evolving Heliosphere. ApJS, 203(1):1, November 2012.

[72] J. E. McCoy. Photometric studies of light scattering above the lunar terminator from apollo solar corona photography. In Lunar and Planetary Science Conference Proceedings, pages 1087–1112, April 1976.

[73] A. Moro-Martín and R. Malhotra. A Study of the Dynamics of Dust from the Kuiper Belt: Spatial Distribution and Spectral Energy Distribution. AJ, 124:2305–2321, October 2002.

[74] A. Moro-Martín and R. Malhotra. Dynamical Models of Kuiper Belt Dust in the Inner and Outer Solar System. AJ, 125:2255–2265, April 2003.

[75] T W Murphy Jr, E G Adelberger, J B R Battat, C D Hoyle, R J McMillan, E L Michelsen, R L Samad, C W Stubbs, and H E Swanson. Long-term degradation of optical devices on the Moon. Icarus, 208(1):31–35, July 2010.

[76] T W Murphy Jr, R J McMillan, N H Johnson, and S D Goodrow. Lunar eclipse observations reveal anomalous thermal performance of Apollo reflectors. Icarus, 231(C):183–192, March 2014.

[77] D. Nesvorný, P. Jenniskens, H. F. Levison, W. F. Bottke, D. Vokrouhlický, and M. Gounelle. Cometary Origin of the Zodiacal Cloud and Carbonaceous Micrometeorites. Implications for Hot Debris Disks. ApJ, 713:816–836, April 2010.

[78] J. Oberst and Y. Nakamura. A search for clustering among the meteoroid impacts detected by the Apollo lunar seismic network. Icarus, 91:315–325, June 1991.

[79] J. H. Oort. The structure of the cloud of comets surrounding the Solar System and a hypothesis concerning its origin. Bull. Astron. Inst. Netherlands, 11:91–110, January 1950.

[80] J.-M. Petit, J. J. Kavelaars, B. J. Gladman, R. L. Jones, J. Wm. Parker, C. Van Laerhoven, P. Nicholson, G. Mars, P. Rousselot, O. Mousis, B. Marsden, A. Bieryla, M. Taylor, M. L. N. Ashby, P. Benavidez, A. Campo Bagatin, and G. Bernabeu. THE CANADA-FRANCE ECLIPTIC PLANE SURVEY—FULL DATA RELEASE: THE ORBITAL STRUCTURE OF THE KUIPER BELT. The Astronomical Journal, 142(4):131, sep 2011.

[81] Carle M Pieters and Sarah K Noble. Space weathering on airless bodies. Journal of Geophysical Research: Planets, 121(1):1865–1884, October 2016.

[82] M. Piquette, D. James, and M. Horányi. Calibration of polyvinylidene fluoride based dust detectors in response to varying grain density and incidence angle. Review of Scientific Instruments, 91(2):023307, 2020.

[83] M. Piquette, A. R. Poppe, E. Bernardoni, J. R. Szalay, D. James, M. Horányi, S. A. Stern, H. Weaver, J. Spencer, C. Olkin, and New Horizons P&P Team. Student Dust Counter: Status report at 38 AU. Icarus, 321:116–125, March 2019.

[84] M. R. Piquette, D. James, and M. Horanyi. The Response of Varying Particle Density and Incidence Angle on Polyvinylidene Fluoride Dust Detectors. In AGU Fall Meeting Abstracts, volume 2019, pages P33I–3534, December 2019.

[85] J. M. C. Plane. Cosmic dust in the earth's atmosphere. Chemical Society Reviews, Vol. 41, p. 6507-6518, 2012, 41:6507–6518, April 2012.

[86] Petr Pokorný, Diego Janches, Menelaos Sarantos, Jamey Szalay, Mihaly Horanyi, David Nesvorny, and Marc J Kuchner. Meteoroids at the Moon: Orbital Properties, Surface Vaporization, and Impact Ejecta Production. Journal of Geophysical Research: Planets, 124(3):752–778, March 2019.

[87] A. Poppe, B. Jacobsmeyer, D. James, and M. Horányi. Simulation of polyvinylidene fluoride detector response to hypervelocity particle impact. Nuclear Instruments and Methods in Physics Research A, 622:583–587, October 2010.

[88] A. R. Poppe, J. S. Halekas, J. R. Szalay, M. Horányi, Z. Levin, and S. Kempf. Ladee/ldex observations of lunar pickup ion distribution and variability. Geophysical Research Letters, 43(7):3069–3077, 2016.

[89] A. R. Poppe, C. M. Lisse, M. Piquette, M. Zemcov, M. Horányi, D. James, J. R. Szalay, E. Bernardoni, and S. A. Stern. Constraining the solar system's debris disk with in situ new horizons measurements from the edgeworth–kuiper belt. 881(1):L12, aug 2019.

[90] Andrew R. Poppe. An improved model for interplanetary dust fluxes in the outer Solar System. Icarus, 264:369–386, January 2016.

[91] J. J. Rennilson and D. R. Criswell. Surveyor Observations of Lunar Horizon-Glow. Moon, 10:121–142, June 1974.

[92] M. Sachse, J. Schmidt, S. Kempf, and F. Spahn. Correlation between speed and size for ejecta from hypervelocity impacts. Journal of Geophysical Research: Planets, 120(11):1847–1858, 2015.

[93] A. Schaufelberger, P. Wurz, S. Barabash, M. Wieser, Y. Futaana, M. HolmstrÃ¶m, A. Bhardwaj, M. B. Dhanya, R. Sridharan, and K. Asamura. Scattering function for energetic neutral hydrogen atoms off the lunar surface. Geophysical Research Letters, 38(22), 2011.

[94] P. H. Schultz, B. Hermalyn, A. Colaprete, K. Ennico, M. Shirley, and W. S. Marshall. The LCROSS Cratering Experiment. Science, 330:468, October 2010.

[95] Peter H. Schultz, Clara A. Eberhardy, Carolyn M. Ernst, Michael F. A'Hearn, Jessica M. Sunshine, and Carey M. Lisse. The deep impact oblique impact cratering experiment. Icarus, 191(2, Supplement):84 – 122, 2007. Deep Impact at Comet Tempel 1.

[96] A. B. Severnyi, E. I. Terez, and A. M. Zvereva. The Measurements of Sky Brightness on Lunokhod-2. Moon, 14(1):123–128, September 1975.

[97] J. A. Simpson and A. J Tuzzolino. Polarized polymer films as electronic pulse detectors of cosmic dust particles. Nucl. Instrum. Methods A, 236:187–202, 1985.

[98] V. J. Sterken, N. Altobelli, S. Kempf, G. Schwehm, R. Srama, and E. Grün. The flow of interstellar dust into the solar system. A&A, 538:A102, February 2012.

[99] Veerle J. Sterken, Peter Strub, Harald Krüger, Rudolf von Steiger, and Priscilla Frisch. Sixteen Years of Ulysses Interstellar Dust Measurements in the Solar System. III. Simulations and Data Unveil New Insights into Local Interstellar Dust. ApJ, 812(2):141, October 2015.

[100] Alan Stern. The evolution of comets in the oort cloud and kuiper belt. Nature, 424:639–642, 2003.

[101] S. A. Stern. Signatures of collisions in the Kuiper Disk. A&A, 310:999–1010, June 1996.

[102] P. Strub, V. J. Sterken, R. Soja, H. Krüger, E. Grün, and R. Srama. Heliospheric modulation of the interstellar dust flow on to Earth. A&A, 621:A54, January 2019.

[103] Peter Strub, Harald Krüger, and Veerle J. Sterken. Sixteen Years of Ulysses Interstellar Dust Measurements in the Solar System. II. Fluctuations in the Dust Flow from the Data. ApJ, 812(2):140, October 2015.

[104] T. J. Stubbs, R. R. Vondrak, and W. M. Farrell. A dynamic fountain model for lunar dust. Advances in Space Research, 37:59–66, 2006.

[105] Mark V. Sykes and Richard Greenberg. The formation and origin of the iras zodiacal dust bands as a consequence of single collisions between asteroids. Icarus, 65(1):51–69, 1986.

[106] A.A. Sysoev, V.P. Ivanov, T.V. Barinova (Komova), Yu.A. Surkov, and V.V. Vysochkin. Mass spectra formation from charged microparticles. Nuclear Instruments and Methods in Physics Research Section B: Beam Interactions with Materials and Atoms, 122(1):79–83, 1997.

[107] J. R. Szalay. The Lunar Dust Environment. PhD thesis, University of Colorado at Boulder, 1 2015.

[108] J. R. Szalay, P. Pokorný, S. D. Bale, E. R. Christian, K. Goetz, K. Goodrich, M. E. Hill, M. Kuchner, R. Larsen, D. Malaspina, D. J. McComas, D. Mitchell, B. Page, and N. Schwadron. The near-sun dust environment: Initial observations from parker solar probe. The Astrophysical Journal Supplement Series, 246(2):27, feb 2020.

[109] J. R. Szalay, P. Pokorný, and M. Horányi. Hyperbolic meteoroids impacting the moon. The Astrophysical Journal, 890(1):L11, feb 2020.

[110] J. R. Szalay, P. Pokorný, Z. Sternovsky, Z. Kupihar, A. R. Poppe, and M. Horányi. Impact ejecta and gardening in the lunar polar regions. Journal of Geophysical Research: Planets, 124(1):143–154, 2019.

[111] J. R. Szalay, Petr Pokorný, Mihaly Horanyi, Diego Janches, Menelaos Sarantos, and Ralf Srama. Impact ejecta environment of an eccentric asteroid: 3200 Phaethon. Planetary and Space Science, 165:194–204, January 2019.

[112] J. R. Szalay, Petr Pokorný, Z Sternovsky, Z Kupihar, Andrew R Poppe, and Mihaly Horanyi. Impact Ejecta and Gardening in the Lunar Polar Regions. Journal of Geophysical Research: Planets, 124(1):143–154, January 2019.

[113] Jamey Szalay, Petr Pokorný, Peter Jenniskens, and Mihaly Horanyi. Activity of the 2013 Geminid meteoroid stream at the Moon. Monthly Notices of the Royal Astronomical Society, 474(3):4225–4231, March 2018.

[114] Jamey R Szalay and Mihály Horányi. Annual variation and synodic modulation of the sporadic meteoroid flux to the Moon. Geophysical Research Letters, 42(24):10,580–10,584, 2015. 2015GL066908.

[115] Jamey R Szalay and Mihály Horányi. The search for electrostatically lofted grains above the Moon with the Lunar Dust Experiment. Geophysical Research Letters, 42(13):5141–5146, 2015. 2015GL064324.

[116] Jamey R Szalay and Mihály Horányi. Detecting meteoroid streams with an in-situ dust detector above an airless body. Icarus, 275:221 – 231, 2016.

[117] Jamey R. Szalay and Mihály Horányi. Lunar meteoritic gardening rate derived from in situ LADEE/LDEX measurements. Geophysical Research Letters, 43(10):4893–4898, 2016. 2016GL069148.

[118] Jamey R. Szalay, Mihály Horányi, Anthony Colaprete, and Menelaos Sarantos. Meteoritic influence on sodium and potassium abundance in the lunar exosphere measured by LADEE. Geophysical Research Letters, 43(12):6096–6102, 2016. 2016GL069541.

[119] Andrei Tovchigrechko and Ilya A. Vakser. How common is the funnel-like energy landscape in protein-protein interactions? Protein Science, 10(8):1572–1583, 2001.

[120] C. Vitense, A. V. Krivov, H. Kobayashi, and T. Löhne. An improved model of the Edgeworth-Kuiper debris disk. A&A, 540:A30, April 2012.

[121] X. Wang, J. Schwan, H.-W. Hsu, E. Grün, and M. Horányi. Dust charging and transport on airless planetary bodies. Geophysical Research Letters, 43(12):6103–6110, 2016.

[122] A. Wehry and I. Mann. Identification of β-meteoroids from measurements of the dust detector onboard the ULYSSES spacecraft. A&A, 341:296–303, 1999.

[123] Martin Wieser, Stas Barabash, Yoshifumi Futaana, Mats Holmstrom, Anil Bhardwaj, R. Sridharan, M.B. Dhanya, Peter Wurz, Audrey Schaufelberger, and Kazushi Asamura. Extremely high reflection of solar wind protons as neutral hydrogen atoms from regolith in space. Planetary and Space Science, 57(14-15):2132–2134, Dec 2009.

[124] Martin Wieser, Stas Barabash, Yoshifumi Futaana, Mats Holmström, Anil Bhardwaj, R. Sridharan, M. B. Dhanya, Audrey Schaufelberger, Peter Wurz, and Kazushi Asamura. First observation of a mini-magnetosphere above a lunar magnetic anomaly using energetic neutral atoms. Geophysical Research Letters, 37(5), 2010.

[125] M. C. Wyatt. Evolution of debris disks. ARA&A, 46:339–383, September 2008.

[126] Lianghai Xie, Xiaoping Zhang, Lei Li, Bin Zhou, Yiteng Zhang, Qi Yan, Yongyong Feng, Dawei Guo, and Shuoran Yu. Lunar dust fountain observed near twilight craters. Geophysical Research Letters, 47(23):e2020GL089593, 2020.

[127] S. Yamamoto and T. Mukai. Dust production by impacts of interstellar dust on Edgeworth-Kuiper Belt objects. A&A, 329:785–791, January 1998.

[128] A. Zaslavsky, N. Meyer-Vernet, I. Mann, A. Czechowski, K. Issautier, G. Le Chat, F. Pantellini, K. Goetz, M. Maksimovic, S. D. Bale, and J. C. Kasper. Interplanetary dust detection by radio antennas: Mass calibration and fluxes measured by STEREO/WAVES. Journal of Geophysical Research (Space Physics), 117(16):5102, May 2012.

Appendix A

Publications

A.1 Papers Published

- Bernardoni, E. A., Szalay, J. R., Horányi, M. (2019). Impact ejecta plumes at the Moon. Geophysical Research Letters, 46, 534– 543.

- Bernardoni, E. A., Szalay, J. R., Horányi, M. (2021). Formation of the Lunar Dust Ejecta Cloud. The Planetary Science journal, 2, 67.

- Piquette, M., Poppe, A., Bernardoni, E., Szalay, J., James, D., Horányi, M., Stern, S., Weaver, H., Spencer, J., Olkin, C., Team, N.H. (2018). Student Dust Counter: Status report at 38 AU. Icarus, 321, 116-125.

- Poppe, A., Lisse, C., Piquette, M., Zemcov, M., Horányi, M., James, D., Szalay, J., Bernardoni, E., Stern, S. (2019). Constraining the Solar System's Debris Disk with In Situ New Horizons Measurements from the Edgeworth-Kuiper Belt. The Astrophysical Journal, 881.

- Stern, S. et al. (2019). Initial results from the New Horizons exploration of 2014 MU69, a small Kuiper Belt object. Science, 364.

- Horányi, M., Bernardoni, E., Carroll, A., Hood, N., Hsu, H., Kempf, S., Pokorny, P., Sternovsky, Z., Szalay, J., Wang, X., (2021). he Dust Environment of the Moon, *in*: The Impact of Lunar Dust on Human Exploration. Cambridge Scholars Publishing.

- Spencer, J. et al. (2020). The geology and geophysics of Kuiper Belt object (486958) Arrokoth. Science, 367.

- Hill, M. et al. (2020). Influence of Solar Disturbances on Galactic Cosmic Rays in the Solar Wind, Heliosheath, and Local Interstellar Medium: Advanced Composition Explorer, New Horizons, and Voyager Observations. The Astrophysical Journal, 905, 69.

A.2 Papers in Review

- Bernardoni, E., Horányi, M., Doner, A., Piquette, M., Szalay, J., Poppe, A., James, D., Olkin, Spencer, J., Stern, A., Weaver, H. (2021). Student Dust Counter status report: The first 50 AU. In review

A.3 Papers in Preparation

- Bernardoni, E. A., Szalay, J. R., Horányi, M. (2022). LDEX Integrated Signal. In preparation

- Bernardoni, E. A., Horányi, M. (2022). Secondary Emission Contributions to the Discrete Dust Grain Charging Model in a Plasma. In preparation